2010

Terahertz and Microwave Detection Using Metallic Single Wall Carbon Nanotubes

Enrique A. Carrion
University of Massachusetts Amherst

TERAHERTZ AND MICROWAVE DETECTION USING METALLIC SINGLE WALL CARBON NANOTUBES

A Thesis Presented

by

ENRIQUE CARRION

Submitted to the Graduate School of the
University of Massachusetts Amherst in partial fulfillment
of the requirements for the degree of

MASTER OF SCIENCE IN ELECTRICAL AND COMPUTER ENGINEERING

September 2010

Electrical and Computer Engineering

TERAHERTZ AND MICROWAVE DETECTION USING METALLIC SINGLE WALL CARBON NANOTUBES

A Thesis Presented

by

ENRIQUE CARRION

Approved as to style and content by:

_____
Sigfrid Yngvesson, Chair

_____
Eric Polizzi, Member

_____
Paul Siqueira, Member

_____
C. V. Hollot, Department Head
Electrical and Computer Engineering

ACKNOWLEDGEMENTS

First and foremost, I would like to thank my principal investigator, adviser, and friend, Dr. Sigfrid Yngvesson, for granting me the opportunity, guidance, and support necessary to finish this thesis. Without him, this work would not have been possible. His contributions to my academic, scientific, and professional life extend beyond the ones placed in this document. His passion for science, research, and particularly nanotechnology will serve me as an example and inspiration anywhere I go.

Also, I would like to mention and thank my two other committee members, Dr. Eric Polizzi and Dr. Paul Siqueira. From them, I learned the experimental and theoretical tools necessary to develop my project and ultimately complete this work. Their vast experience in their respective fields, computational nanoelectronics and microwave engineering, directly influenced my project and career.

In this section I would also like to acknowledge and thank the several other graduate students and staff that in one way or other accompanied and supported me throughout the past two years. Being able to work with and learn from friends has been one of the best experiences I have had while at UMass. From the THz lab, Martin Muthee, Jason Donovan, John Nicholson, Ric Zanonni, and former members Kan Fu and Bo Fu, have always demonstrated an interest and willingness to help, collaborate, and do experiments together. Their input was very important at several stages of this work. Even more, without them -in particular Martin Muthee and Jason Donovan- the times in which measurements run for long hours until late at night would not have been as enjoyable. Also Mauricio Sanchez from LAMMDA was a huge resource to help me find the equipment for the MW responsivity and the S-parameters measurements.

I would also like to thank Dr. Robert Jackson, and Dr. Marinos Vouvakis for letting me use equipment from their labs in order to do MW measurements. Those measurements became an important part of this work and would not have been possible without their collaboration. Lastly, I would like to thank my family and friends who always believed in me and encouraged me to pursue the career that interested me the most. Thanks Mom, Dad, Gian, and Sara, your support means the world to me.

ABSTRACT

TERAHERTZ AND MICROWAVE DETECTION USING METALLIC SINGLE WALL CARBON NANOTUBES

SEPTEMBER 2010

ENRIQUE CARRION

M.S.E.C.E, UNIVERSITY OF MASSACHUSETTS AMHERST

Directed by: Sigfrid Yngvesson

Carbon nanotubes (CNTs) are promising nanomaterials for high frequency applications due to their unique physical characteristics. CNTs have a low heat capacity, low intrinsic capacitance, and incredibly fast thermal time constants. They can also exhibit ballistic transport at low bias, for both phonons and electrons, as evident by their fairly long mean free paths. However, despite the great potential they present, the RF behavior of these nanostructures is not completely understood. In order to explore this high frequency regime we studied the microwave (MW) and terahertz (THz) response of individual and bundled single wall nanotube based devices. This thesis is an experimental study which attempts to understand the high frequency characteristics of metallic single walled carbon nanotubes, and to develop an ultra-fast and sensitive direct THz detector.

First, the appropriate high frequency detector background is introduced. CNTs previously measured behavior draws similarities to two types of detectors: diode and bolometer. Therefore, our CNT devices are geared towards those designs. Second the fabrication process of devices is reviewed. UV lithography is used to pattern THz coupling log periodic antennas, on top of which CNTs are deposited by using a dielectrophoretic process. Third, the fabricated devices are tested at DC, MW, and THz frequencies. All of these measurements are done as a function of temperature, power, and frequency. Finally, the physical processes that give rise to the diode and bolometric detections at MW and THz detection at different temperatures and under different bias regimes (i.e. low and high) are explained.

TABLE OF CONTENTS

Page

LIST OF TABLES

Table Page

LIST OF FIGURES

Figure Page

CHAPTER 1
INTRODUCTION

1.1 Project Motivation

The Terahertz (THz) gap is the region of the electromagnetic spectrum in between Infrared (IR) and Microwave (MW) frequencies; it spans from about 1 to 10 THz. These frequencies approximately correspond to wavelengths from 30 to 300 μm (Fig. 1.1).

Several applications which take advantage of the high frequency, long wavelength, and low-power characteristics of THz have been developed over the last decade. THz are currently being used and researched in medical imaging [1], security and sensing [2][3], spectroscopy [4], astronomy [5], and other fields. Depending on the desired application some of the difficulties of working at such high frequencies range from power limitations and frequency tunability, to beam pattern resolution and atmospheric attenuation. However, regardless of the wide variety of difficulties pertinent to each application, a common obstacle to all has been the lack of reliable sources and detectors.

Over the past several years, the source-detector issue has been addressed, and to a certain extent, resolved. Currently there are a variety of both commercial sources and detectors available [6][7][8]. Quantum cascade lasers, frequency multipliers, time domain systems, and gas lasers, are just a few of the sources commonly used (Fig. 1.2). In the case of direct detectors, diodes, pyroelectric detectors, and semiconductor bolometers are the most common and easily available devices, while in the case of mixing applications, superconducting silicon-insulator-silicon (SIS) structures and hot electron bolometers (HEBs) are used as the standard mixers [9][10]. However, one of the main disadvantages of all of these devices is that cryogenic temperatures of 4K, or in some cases even lower (~mK), are required for their operation.

On the other hand, carbon nanotube based devices are promising for THz detection based on some unique characteristics that arise from their small diameters (1-2 nm). CNTs have very low heat capacity [11], low intrinsic capacitance [12], and ultra fast thermal time constants [13]. They can also exhibit ballistic transport at low bias, for both phonons and

electrons [14], since they have a fairly long mean free path [15]. Furthermore, our group has had vast experience designing and testing niobium nitride (NbN) superconducting HEBs [16], as well as CNT based direct and heterodyne MW detectors [17]. Taking advantage of our group's expertise in both of these areas, this work will attempt to understand the high frequency (MW and THz) characteristics of metallic single walled carbon nanotubes and develop an ultra-fast and sensitive direct THz detector.

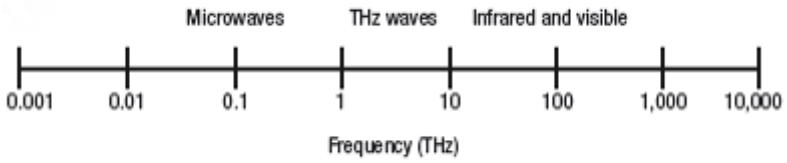

Figure 1.1 Electromagnetic spectrum denoting the terahertz region between microwave and infra-red frequencies. From ref. [6].

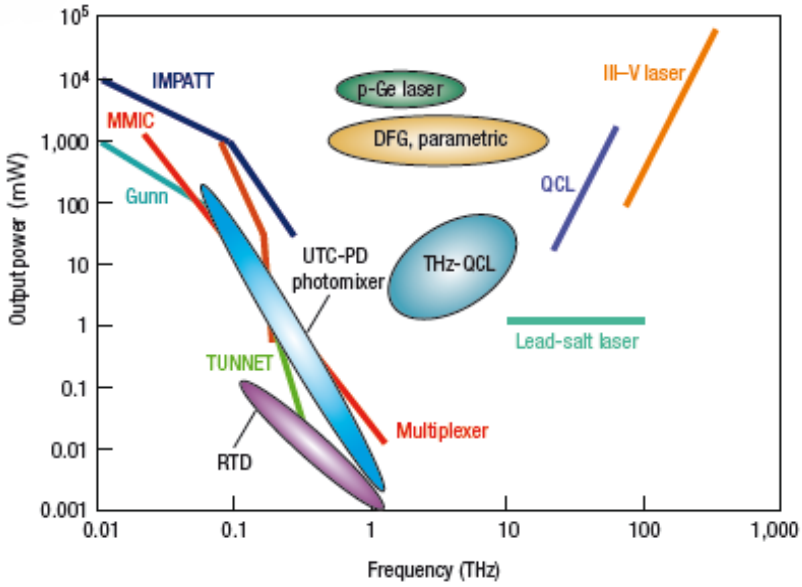

Figure 1.2 Common terahertz sources as a function of frequency. [6]

1.2 Carbon Nanotube Basics

1.2.1 Physical Structure

The physical structure of carbon nanotubes, as well as many of their electric and thermal properties, are consequences of the unusual physical and electronic structure of graphene (Fig. 1.3). Graphene is a single atom layer thick sheet of sp^2 bonded carbon atoms. Carbon nanotubes, discovered by Iijima [18] in 1991, can be thought of as rolled up sheets of graphene. The chiral vector *C* (Eq. 1), which describes the circumference of the CNT, also defines the direction upon which a certain nanotube may be rolled up. In Eq. 1, a_1 and a_2 serve as the unit vectors that define the basis in the honeycomb graphene lattice, and the indexes *n* and *m* define the different combinations along the many directions upon which the CNT can be wrapped. This results in a unique one dimensional structure, which due to its boundary conditions around its circumference, has a quantized component of momentum ($k_{\perp}$) along the circumference, and a continuous one ($k_{||}$) along the length of the tube. The latter determines the free electron motion of electrons in this axial direction.

$$\overline{C} = n\overline{a}_1 + m\overline{a}_2 \qquad (1)$$

From the quantization of momentum in the circumferential direction ($k_{\perp}$), discrete energy sub-bands are formed for each possible CNT. The relation between these sub-bands and the band structure of graphene determines the electronic structure of CNTs. If the sub-bands pass through the K or K' Dirac points (shown in Fig. 1.3) the nanotube has a metallic band structure, otherwise it behaves as a semiconductor. More specifically, when the indices *n* and *m* are equal (n=m) the nanotube is metallic and it forms in the Armchair structure; when *n* minus *m* is a multiple of three (n-m=3j) the nanotube is quasi-metallic (i.e. a very small band gap, on the order of meV) and can form in the Zigzag structure (when n=0); finally when *n* minus *m* is not a multiple of three (n-m≠3j) the resulting nanotube will be semiconducting and form in the Chiral structure. We can see all of these cases and structures, as well as single, multi-walled, and a bundle of CNTs in Fig. 1.4. This work will deal exclusively with metallic CNTs.

Additionally, multi-walled nanotubes (MWNTs) may also be formed upon the rolling of several sheets of graphene. (Fig. 1.4). MWNT diameters range from a few nm up to about 100nm, while SWNT diameters range from about 1 - 3 nm.

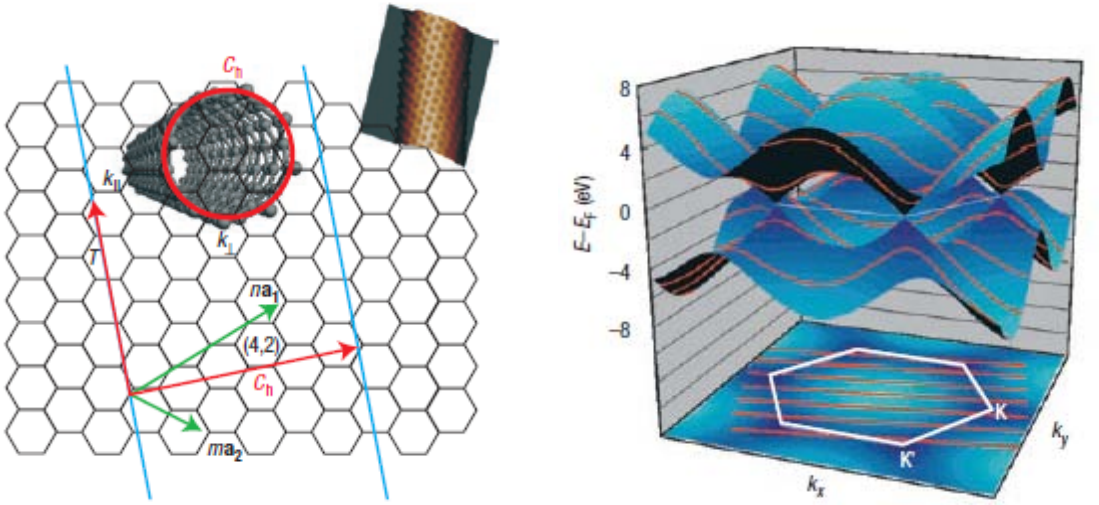

Figure 1.3 (Left) Graphene sheet denoting chiral vectors, and chiral indices. (Right) Electronic structure of graphene showing K and K' Dirac points. From ref. [19].

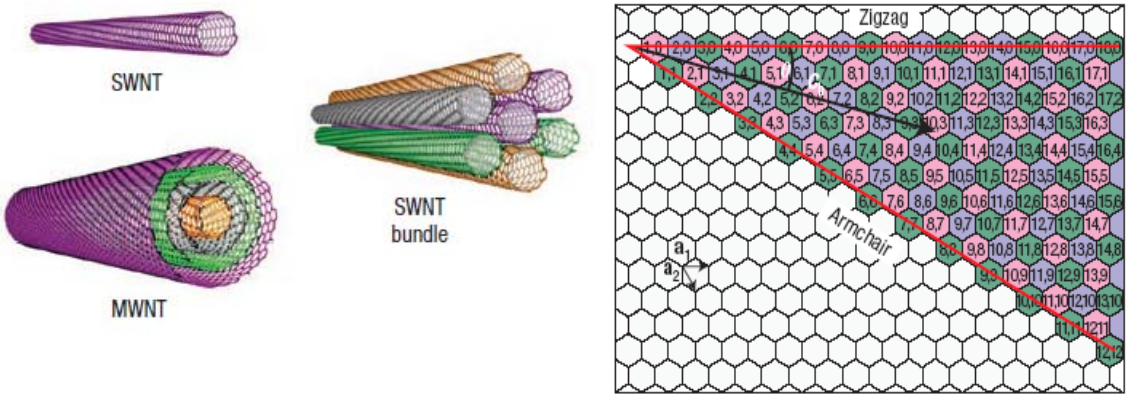

Figure 1.4 (Left) Single-walled, multi-walled, and bundle of CNTs. (Right) Armchair, Zigzag, and Chiral structures of CNTs. From ref. [20].

1.2.2 DC and AC Behavior

Metallic CNTs have been studied for a number of years since they were first measured in 1997 [21][22]. The DC characteristic of individual carbon nanotubes are well known. Like in macroscopic structures, the electrical properties used to describe nanotubes, such as resistance, capacitance, and inductance, arise from their unique structure and their interactions with the environment (i.e. contacts). However, due to their one-dimensionality, their transport properties are different than the ones of other three dimensional materials. For example, the mean free paths (mfp) of a nanotube are much longer than those of bulk semiconductors. For acoustical phonons (AC), the mfp can be greater than 1μm at room temperature, while for optical phonons (OP) the mfp is about 15nm [23].

Moreover, even with such a small mfp for OP, electron-OP scattering processes do not occur at low energies (supplied through the bias voltage); it is not until a bias of about 160mV [24] is applied across the CNT that scattering effects begin to show. The main effect of this scattering can be observed in the measured DC characteristics of the CNT device, since a clear current saturation occurs as the bias voltage is increased. Ideally, for a perfect contact situation the maximum amount of current that can go through a single SWCNT can be calculated to be about 25μA.

Similarly, using the Landauer formulism [12] and considering the number of modes (M=2) and spin one can calculate the minimum DC resistance of a single CNT to be approximately $R_{CNT} = h/2e^2M = 6.45K\Omega$. Nonetheless, the actual measured resistance for CNT based devices depends greatly on the quality of the contacts. Contacts add to the total measured DC resistance of the CNT from a few KΩ to hundreds of MΩ. Annealing has been shown [25] to clearly improve the quality of the contacts and lower the total resistance of the device. All around contact techniques, and choices of metals with work functions closer to the Fermi level of carbon, such as palladium (Pd), have also been shown [26] to improve contacts.

Additionally, nanotubes can also be described in terms of an intrinsic kinetic inductance (L_k), and a quantum capacitance (C_Q). The physical origin of the first one is due to an excess of kinetic energy resultant from current flow from a 3D electron reservoir (i.e. metal contacts) to a 1D system. The low density of states (DOS) of nanotubes forces us to

consider extra kinetic energy required to place electrons in a conducting state. Similarly, considering the change in charge density due to a change in the potential results in the already mentioned C_Q. For a metallic SWNT, the value of L_k is 4 nH/μm [28]. This value is almost three orders of magnitude bigger than the classical electromagnetic inductance (L_M), and therefore the latter can be ignored. On the other hand, the value of C_Q which can be calculated to be approximately about 100aF/μm, is around the same order of magnitude as the classical electrostatic capacitance (C_E~50aF/μm).

In contrast to the well-known DC electrical properties of nanotubes, attempting to describe the AC characteristics proves to be more challenging. A well-known and generally accepted model for the high frequency transport inside a CNT is not available, mainly due to the complexity added from the CNT low dimensionalities. It has been documented that the Landauer picture breaks down in 1D [27]. Burke [28] has proposed a model, in which he considers interacting electrons, rather than non-interacting electrons inside the well-known Fermi gas. Burke and others [29][30] have suggested the presence of a different medium: The Luttinger-Tomonaga liquid [31][32]. In this case, electron-electron interactions become relevant and affect transport; the main predicted consequence is a power-law dependence of the thermal and electrical conductivity. Using this theory, Burke arrives to a model that describes a CNT as four parallel and connected transmission lines (TL), composed of the previously mentioned L_K, and C_Q (Fig. 1.5). These channels represent 3 spin current carrying modes, and 1 electron current carrying mode. This model and its channels can be reduced to deal exclusively with the current carrying mode of the CNT (Fig. 1.6). As we can see in Fig. 1.6, a series resistance has been added to the TL in order to account for the CNT DC resistance (R_{CNT}). Also, note that in this figure, the kinetic inductance is divided by a factor of 4, and the quantum capacitance is multiplied by 4. This is done to compensate for the fact that we have added the electrical effect of the four channels into one. Finally, to complete the TL model, we will account for the effect of the contacts that will be necessary in order to characterize our device (Fig. 1.7). Here we have added both a contact resistance (R_C) and a contact capacitance (C_C). This model will be referred throughout this work as *The Modified Burke TL Model*. In this work, we will mainly focus on the effects and consequences that treating the CNT as a transmission line in series with the CNT resistance

can have in our own CNT devices (detectors) rather than discussing the validity of the Luttinger liquid theory.

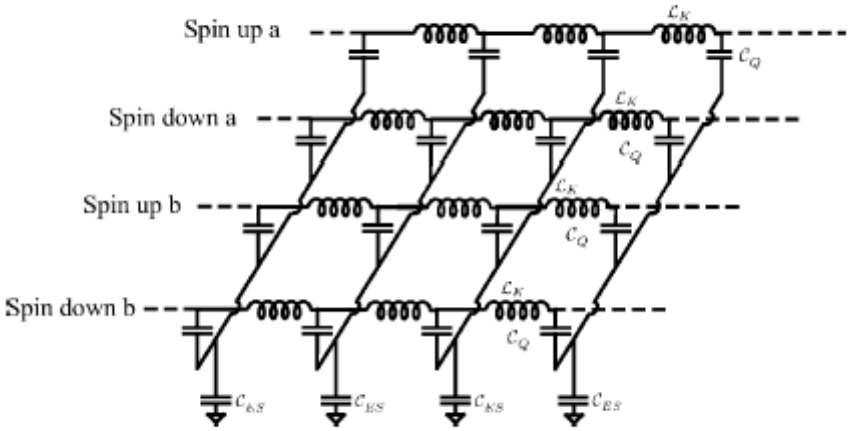

Figure 1.5 AC circuit model for interacting electrons. Four modes, 3 spin carrying, and 1 current carrying are coupled due to electron-electron interactions in a 1D conductor. From ref. [28].

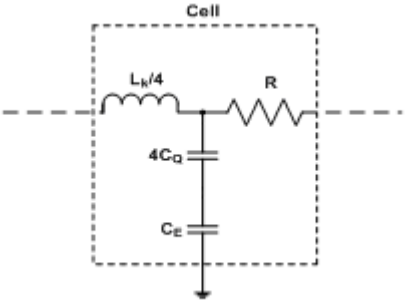

Figure 1.6 Unit cell of the transmission line model, composed of a kinetic inductance, a quantum capacitance, a negligibly small electrostatic capacitance, and a series CNT resistance. Note: In this work we will denote R as R_{CNT}.

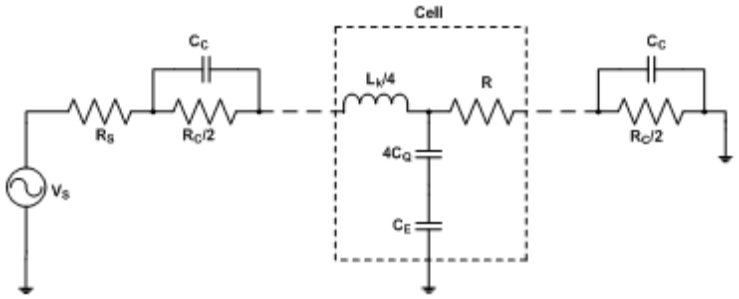

Figure 1.7 *Modified Burke TL Model.* Complete transmission line (TL) model used in this work to treat the CNT. Note that the complete model treats the CNT as a TL in series with the DC CNT resistance. Also, contact resistance (C_R) and capacitance (C_C) are added to model device accurately.

Some of the main consequences of treating nanotubes as a TL, are the presence of expected TL properties, such as phase velocity (v_p) and characteristic impedance (Z_C). In [28], Burke carefully derives these values for a single CNT, as well as the ones for L_K and $C_{Q.}$ Others [29] [33], have also experimentally measured L_K and C_Q values for semiconducting or metallic single or bundles of CNTs. In this work, we will attempt to reproduce measurements from [29] in order to obtain a more clear idea of how certain parameters, such as R_{CNT}, R_C, C_C, and L_K, of the *Modified Burke Model* (Fig. 1.7) affect our own CNT based devices.

1.3 Overview of MW/THz detectors

In this section, we will first present a short review of a few of the most common MW and THz direct detectors, their principles of operation, and the performance and limitations expected from them. Then, we will introduce two new kinds of detectors that we expect to fabricate using metallic single walled carbon nanotubes (m-SWCNTs): The CNT Diode Mode Detector and CNT Bolometer Mode Detector. Once again, the basic principles of operation will be described, as well as their expected performance and limitations.

1.3.1 Pyroelectric Detectors, Schottky Diodes, and Semiconductor Bolometers

Pyroelectric detectors consist of ferroelectric materials, such as triglycine sulphate (TGS) or lithium tantalate, which exhibit large spontaneous electrical polarization changes when their temperature varies. The change in polarization can be observed if these materials are placed in between two electrodes, forming a capacitor. Then, when IR or far IR radiation hits the detector a voltage is created across this capacitor, and an external impedance (Fig. 1.8). These detectors have several advantages, such as high responsivity (3-10 KV/W), room temperature operation, fast thermal response (~1μs), low cost, and stability against ambient temperature, atmospheric changes, and electromagnetic interference. However, they only respond to time varying signals. Furthermore, they are not sensitive to wavelength, just to temperature changes. IR Filters placed in front of the detectors are used for "wavelength selectivity."

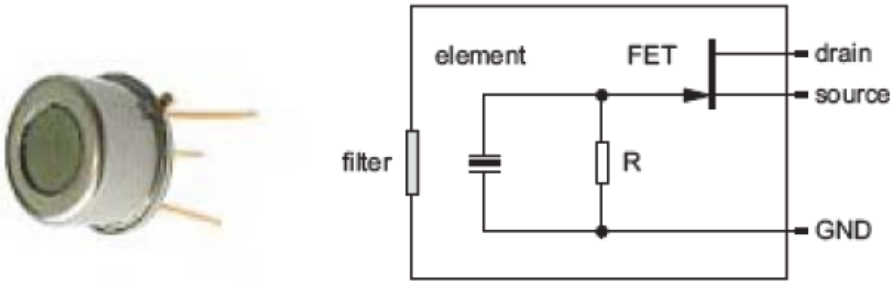

Figure 1.8 Pyroelectric detector (left) and its main schematic (right).

Schottky diode detectors, are also well-known common devices in MW and THz electronics. They can be used as direct detectors and mixers for a wide variety of frequencies. They operate by sensing a change in the IV characteristics of the device due to the RF voltage applied. In other words, the RF voltage can be detected ‘directly’ by measuring the changes in the non-linear IV curve of the diode device [34]. This 'detected' change in current can be calculated by simply taking into account the DC characteristics of the device.

Considering the expression for current as a function of voltage of a Schottky diode and applying a simple approximation, the current can be found to be exponentially

proportional to α , see (2). Now, we consider $V = V_o + \delta V$, where V_o is an average DC voltage and δV is an oscillating component of RF voltage ($\delta V = V_{RF}\, sin(\omega t)$); then, we substitute V in (2) and apply a Taylor series expansion. The result (3) contains several terms which will be analyzed individually. The first term, $I(V_o)$, is simply the bias current applied to the device; the second term, $dI/dV \cdot V_{RF} \cdot \sin(\omega t)$, is composed of a sinusoidal component varying at frequency ω and the linear dynamic conductance (first voltage derivative of the current). The third and most important term for detection, $d^2I/dV^2 \cdot V_{RF}^2$, consists of the squared RF voltage and the second voltage derivative of the current. Here, a small change in DC current (ΔI) is produced due to the squared RF voltage (4). This last term will be the one used to 'detect' the RF signal. An example of a Schottky diode, also known as square law detector, is shown in Fig. 1.9.

(2) $$I(V) = I_S \cdot \left(e^{eV/\eta K_B T} - 1\right) = I_S \cdot \left(e^{\alpha} - 1\right) \cong I_S \cdot e^{\alpha}$$

(3) $$I(V_O + \delta V) = I(V_O) + \frac{dI}{dV}\delta V + \frac{1}{2}\frac{d^2I}{dV^2}(\delta V)^2 + \ldots$$

(4) $$\Delta I = \frac{1}{4} \times \frac{d^2I}{dV^2} \times V_{RF}^2$$

A *bolometer device* basically exhibits changes in its resistance as it dissipates power. This device is quite different than the previously described Schottky diode; in this case, the detection is due to the RF power absorption by the bolometric material, not due to an instantaneous RF voltage. A bolometer is said to be a 'hot electron' bolometer (HEB), if the RF energy heats up the electrons inside the device higher than the lattice temperature. This change in electron temperature is what in turn produces a change in resistance. Overall, a bolometer device (Fig. 1.10) is described by a temperature dependent resistance $R(T)$ (5), a heat capacity C_o (6), and a thermal conductance G_{th} (7) [35].

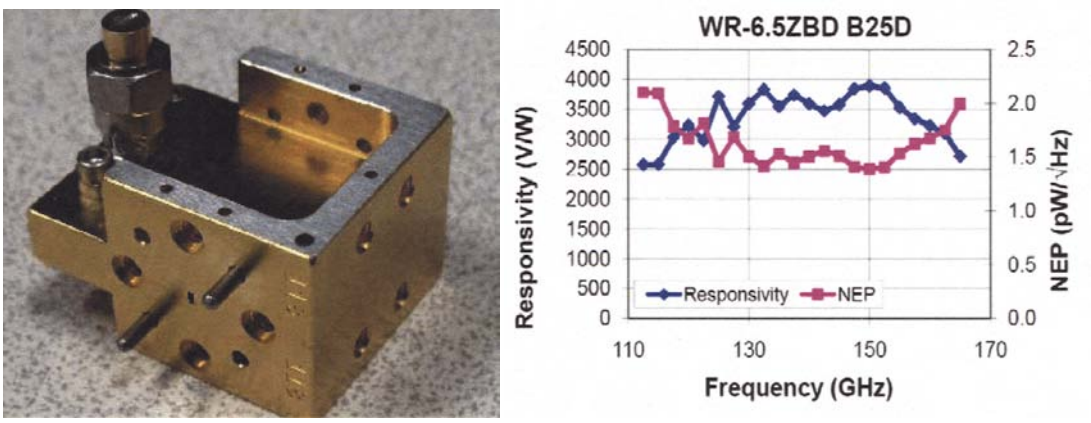

Figure 1.9 Virginia Diode Inc. Zero bias Schottky diode THz detector (left) and responsivity and NEP as a function of frequency (right). Additionally, the detector responsivity ranges from 4 KV/W at 100GHz, to 400V/W at 900GHz; this detector is designed for low power operation with an NEP of about $1.5\times10^{-12}\ W/\sqrt{Hz}$. From ref. [36]

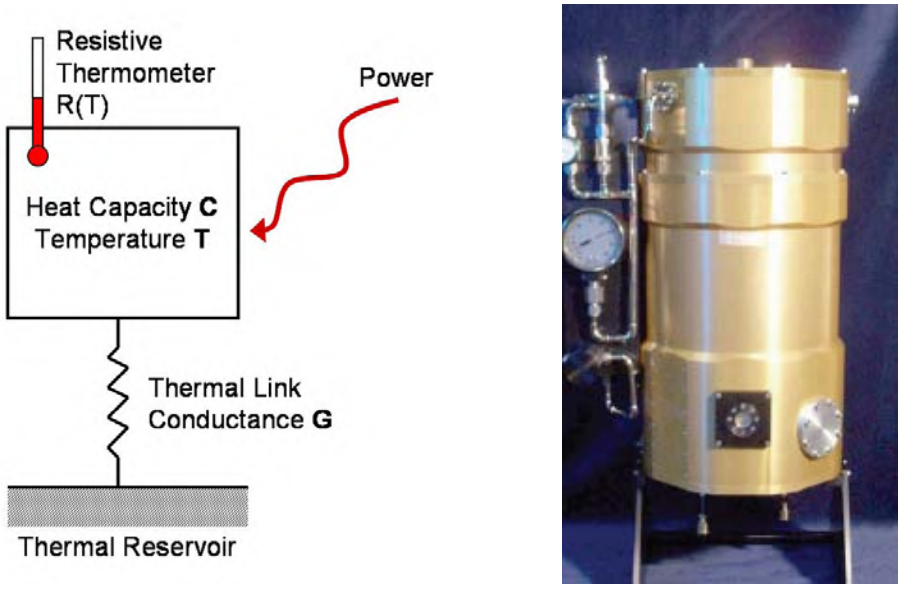

Figure 1.10 Conceptual model of a common bolometer device. Note that the thermal conductance G (G_{th}) is the main link for the device to dissipate the energy acquired from the incident power (left, from ref. [35]). Typical Si superconducting bolometer (right), spectral response from 2 - 3000μm, operating temperature from 4.2 - 0.3K. The bolometer responds only to an AC signal within detector bandwidth.

(5) $$R(T) = R_0 + (dR/dT)\cdot \delta T$$

(6) $$C_o = \frac{dR}{dP} = \frac{dT}{dP}\cdot\frac{dR}{dT} = G_{th}^{-1}\cdot\frac{dR}{dT}$$

(7) $$G_{th} = dP/dT$$

As in the Schottky diode case, the response of a bolometer can be predicted based on its IV characteristics. We start by considering the circuit shown on Fig. 1.11. We see that the bolometer device absorbs RF power (P_{RF}). As power is absorbed, the voltage, current, and resistance of the bolometer go from $V_o \to V_o + \Delta V$, $I_o \to I_o - \Delta I$, and $R_o \to R_o + \Delta R$. Thus, the voltage across the bolometer, ignoring the second order term "$\Delta I \cdot \Delta R$" will equal,

(8) $$V_o + \Delta V = (I_o - \Delta I)\times(R_o + \Delta R) = \underbrace{I_o R_o}_{Vo} + \underbrace{I_o \Delta R - R_o \Delta I}_{\Delta V}.$$

Similarly, the absorbed DC power (P_{DC}), goes from $P_{DC} \to P_{DC}^0 + \Delta P_{DC}$. Thus, once again ignoring the second order term "$\Delta I \cdot \Delta V$" results in,

(9) $$P_{DC}^0 + \Delta P_{DC} = (V_o + \Delta V)\times(I_o - \Delta I) = \underbrace{I_o V_o}_{P_{DC}^0} + \underbrace{I_o \Delta V - V_o \Delta I}_{\Delta P_{DC}}.$$

Also, by analyzing the circuit, the load resistance (R_L) should equal,

(10) $$R_L = \frac{\Delta V}{\Delta I}.$$

Finally, recalling the definition of the factor C_0 for the bolometer (see (6)) and since we have the input from two sources of incident power (P_{RF} and P_{DC}), we have

(11) $$C_o = \frac{dR}{dP} \approx \frac{\Delta R}{\Delta P} \longrightarrow \Delta R = C_o \cdot \Delta P = C_o \cdot (\Delta P_{RF} + \Delta P_{DC}).$$

Now, with expressions (8) - (11), we have all the necessary equations to derive the responsivity. Details of the algebraic procedure can be seen in Appendix 1. Here, we will merely present the main result obtained there. We define the bolometer responsivity (12) as

the change in output voltage for a change in the incident power. The final simplified responsivity is shown in (13).

$$Sv^{B} = \frac{\Delta V}{\Delta P_{RF}} = \frac{\Delta I \cdot R_L}{P_{RF}} \tag{12}$$

$$Sv = \frac{I_o}{G_{th}} \frac{dR}{dT} \tag{13}$$

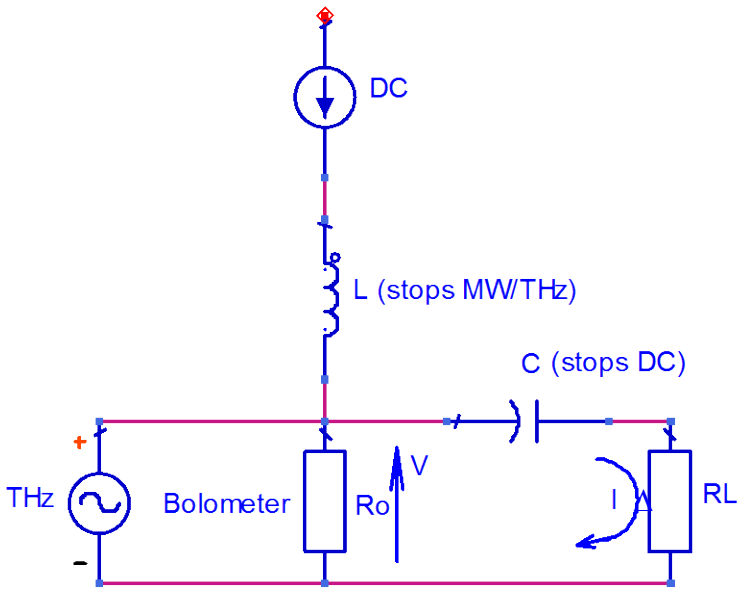

Figure 1.11 Circuit model for a typical bolometer. Note that in this case, the 'incident' RF power is represented by a THz source

1.3.2 CNT Diode Mode Detector

In the case of the diode mode, we propose the use of a CNT based detector as a non-linear device which can sense the small changes in current produced by an RF voltage. Such a detector has been previously been shown to work by our group [37]. In order to describe, model, and test the behavior of these devices, we will use the previously addressed and well known standard Schottky diode microwave theory. For this purpose, we now define the CNT diode mode detector voltage responsivity (Sv^D) (14) in terms of the change in current (ΔI) produced in the IV characteristics of the CNT, the resistance of the device (R), and the RF power absorbed in the CNT (P_{RF}). Finally, inserting the previously derived value of ΔI gives rise to the main expression (15) that will be used in order to describe the responsivity of the diode mode CNT based detector.

$$Sv^D = \frac{\Delta V}{P_{RF}} = \frac{\Delta I \cdot R}{P_{RF}} \tag{14}$$

$$Sv^D = \frac{1}{4} \times R \times \frac{d^2 I}{dV^2} \frac{V_{RF}^2}{P_{RF}} \tag{15}$$

Analyzing (15), we note that the main factors contributing to the voltage responsivity are the second voltage derivative of the current (d^2I/dV^2), the resistance of the device (R), and the impedance produced by the RF voltage. This last term (V^2_{RF}/P_{RF}), depends on the amount of RF voltage that is reflected at any interface, usually at the contacts. Mismatch problems between the 3D electron reservoir (R_o=50Ω) and the impedance of the load CNT (R_L ranges from 50Ω to 900MΩ) have a negative effect for the detection. How ever, this limiting factor in principle is not very large, since a device with a very large mismatch will actually increase the RF voltage across the device. The other two factors that compose Sv^D are the nonlinearity of the IV characteristics (dI/dV) and the resistance (R). Both of these terms depend on each other and should also be in principle, very large. Additionally, it is important to mention that even though the IV characteristics of a diode and a CNT are quite different, the same diode detector theory can still be employed to describe the CNT devices. The main difference of the CNT devices is that the current increases independently of the

applied bias polarity (positive or negative). This difference is not relevant when considering the instantaneous change in current produced by the RF power. The only consequence will be the ability to detect the RF voltage without any preference for the polarity of the applied bias.

Finally, we examine in further detail the IV characteristics of a typical CNT device. As we can see from Fig. 1.12, the current (red) has a very pronounced nonlinearity near the zero bias voltage point; this effect is also visible in the conductance, *dI/dV (blue)*. Such dips in the conductance are called zero bias anomalies (ZBA's) and commonly seen in metallic carbon nanotubes [38]. ZBA's are known to increase with decreasing temperatures and are usually a consequence of the presence of energy barriers at the metal-CNT interface. These barriers tend to increase the contact resistance (i.e. create 'bad contacts') which strongly dominates the IV characteristics compared with that of the CNT itself. Therefore, it is concluded that the diode mode detection in CNTs arises from the presence of strong ZBA's in the IV characteristics of our devices. This type of RF detection will mainly be the product of 'bad' or 'not perfectly ohmic' contacts, and will be measured and studied in detail through several measurements and experiments. For the 'good' or *ohmic* contact case the physical process which gives rise to the diode model will be a different one., and will be discussed in Chapter 3.

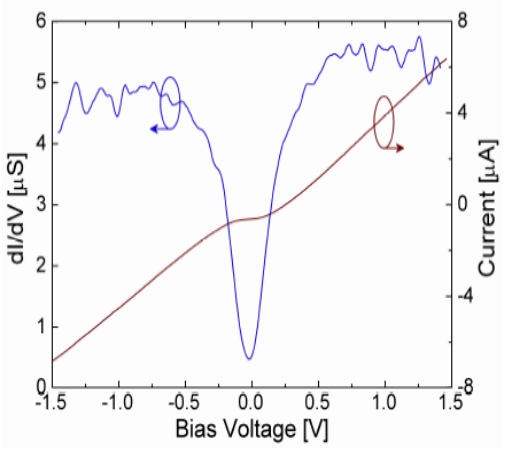

Figure 1.12 Non-linear symmetrical IV curve of CNT device with high contact resistance. From ref. [37].

1.3.3 CNT Bolometer Mode Detector

A bolometer device, as introduced in the previous section, measures the power of an incident electromagnetic signal as it heats the bolometric material, which has a temperature dependent resistance. Below, (Fig. 1.13) a more complex and specific diagram of a typical bolometer is presented. In this model, we define an electrical output, which translates to the measured 'responsivity,' (Sv^B), a DC bias, which gives some initial energy to the electrons inside the bolometer, the absorbed power $P_{THz/MW}$, which raises the temperature of the electrons in the device, and a thermal conductance G_{th} and heat capacity C_h, which characterize the ways in which the device dissipates power into its environment (i.e. a heat sink). In the case of our CNT based bolometers, the heat sink could be the metal-CNT contacts and/or the substrate-CNT interface. Furthermore, like most bolometric materials, we will consider the CNT based detectors to behave as hot electron bolometers (HEB's). In these devices, the system of electrons is heated to higher temperatures than that of the lattice (i.e. the phonons); this effect increases at cryogenic temperatures, since the electrons can be driven out of thermal equilibrium much more easily by the incoming radiation.

The HEB's voltage responsivity (Sv^B) can be predicted from the IV characteristics of the device, as shown for the 2DEG devices [39], superconducting NbN films HEBs [16], and this work's derivation in section 1.3.1. In the latter, suitable expressions that

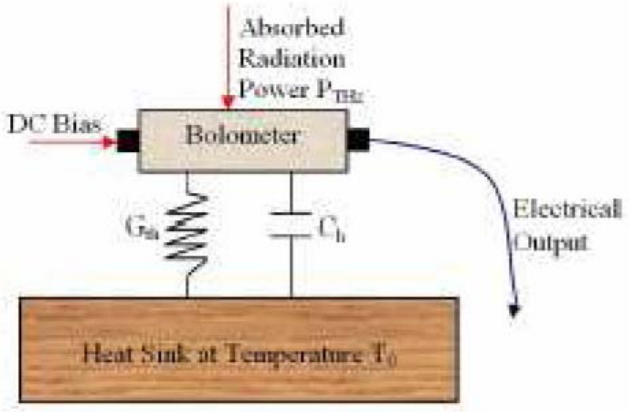

Figure 1.13 Diagram of a typical bolometer. Electrical output changes as DC bias and RF power are absorbed.

describe the detection process are shown in (12) and (13). Additionally, we now define a normalized nonlinear resistance factor *b* (16) and a new but equivalent expression for the responsivity (17). It is important to note that for our CNT HEBs, electro-thermal feedback terms have been avoided (see Appendix 1), since they will only affect the response for very high responsivity values [40].

$$b = \frac{1}{R} \times \frac{dR(T)}{dT} \tag{16}$$

$$Sv^{B} = \frac{\Delta V}{P_{RF}} = \frac{V_O \cdot b}{G_{th}} \tag{17}$$

Furthermore, by analyzing both of these equations (16) and (17), it becomes clear that the CNT bolometric detection process will be dominated by the nonlinear resistance *dR(T)/dT* (where T represents the electron temperature) and G_{th}. A high value for G_{th} is detrimental to the response of the device, since it would imply that a large amount of the energy obtained from the RF power is 'lost' to the heat sink instead of transferred into the electrons. Finally, metallic single SWCNTs have been shown in [35] and [41] to be optimum devices in terms of the two main contributing factors (*dR(T)/dT* and G_{th}) to the bolometric response. Fig. 1.14 shows the nonlinear temperature dependent resistance of a metallic single SWCNT which uses the substrate and contacts to dissipate heat.

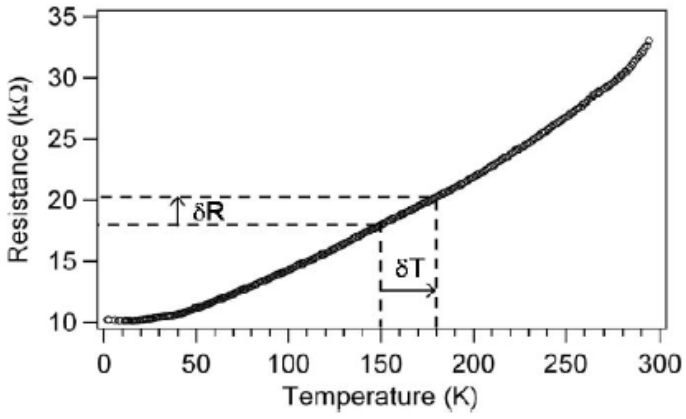

Figure 1.14 Temperature dependent resistance of a single SWCNT 3μm long that gives rise to the bolometer model for detection. From ref [35].

1.4 Scope of the Work in this Thesis

This project brings together two broad, important, and relevant areas of science: RF engineering and nanotechnology. The thesis work presented here makes use of fabrication techniques, measurement setups, and theories used in both fields in order to describe the phenomena observed in our CNT based devices. Three main goals have been achieved in the duration of this project. First, CNT bundle based devices have been characterized at DC, MW, and THz frequencies. Second, "well-contacted" single CNT based devices have been fabricated. Finally, similar characterization measurements were performed for the new "well-contacted" devices.

Throughout this document, the completion of the previously mentioned goals will be demonstrated through measurements, and simulations. The DC measurements served many purposes, such as to constantly monitor the CNTs (since changes in DC resistance often translated to changes to the number of active CNTs), to predict the behavior of the device at MW and THz frequencies, and to obtain insight into the energy barriers present at the contacts. Several MW and THz direct detection experiments on different CNT based devices will also be described. These measurements were made as a function of several variables that affected detection, such as bias voltage, frequency, power, and temperature. Different combinations of these dependencies will be presented. The theoretical tools, such as the diode and bolometer models, used to understand and explain the MW and THz detection processes, will additionally be derived, presented, and tested. Finally, MW S-parameter characterization measurements were also done in order to obtain parameters for a circuit model which describes our CNT based devices. The measurements and simulations were done from 10MHz up to 26.5GHz, and even though this frequency range is much smaller to the one of interest (from 0.6 - 2.54THz) we were still able to obtain valuable insight into how the CNTs might behave at THz frequencies according to the parameters derived for the circuit model.

1.5 Organization of Thesis

This thesis contains four main chapters. Chapter 1 - Introduction, presents an overview of working at THz frequencies, and introduces the potential of CNTs for high frequency (MW and THz) detection. This project motivation is followed by a brief review of current commercial THz detectors, along with the proposed CNT based detector models. Chapter 2 - Experimental Work, contains the experimental setups, results, and preliminary analysis for all the characterization done in the different types of CNT devices fabricated. DC, MW, and THz measurements will be presented in this section. Chapter 3 - Understanding the Detection Process, goes further in detail on the Diode and the Bolometer models proposed. In this chapter other theories and models, such as the *Yang theory* and the *Modified Burke TL Circuit Models*, are also introduced in order to further evaluate and approach the physical processes of the MW and THz detection. Finally, Chapter 4 - Future Work, presents clear concrete steps which the CNT research at UMass Amherst in the THz lab could take in order to improve the performance and understanding of our CNT based THz detectors.

CHAPTER 2
EXPERIMENTAL WORK

2.1 Device Fabrication Progress

Our CNT based diode and bolometer detectors consist of SWCNTs placed across the smallest gap of a log periodic antenna (LPA) embedded in a CPW, as shown in figure 2.1. The LPA is a self-complimentary antenna, which is partially independent of source frequency, since its structure is specified by more than one angle. Also, its impedance and radiation patterns repeat periodically as the logarithm of the frequency. In our case, at THz the LPA has an impedance of 100Ω and at MW frequencies (up to several GHz) of 50Ω. When THz radiation strikes the teeth of the antenna, it produces THz currents that travel along the edges of the metal until they reach the CNT. The CPW serves a dual purpose: Large DC electrical contacts for probing of devices, and transmission lines at MW frequencies for further device characterization. The fabrication of these structures (LPA embedded in a CPW) and the placement of the CNTs are two separate processes which will be described in detail in this section. First, we start by reviewing the fabrication of the antennas through several generations in order to develop an optimum CNT based detector. Each design was tailored to improve a certain feature from a previous configuration.

2.1.1 Four Generations of Log Periodic Antenna

Four generations of LPA's will be described in this section. All of these antennas were fabricated using UV photolithography on high resistivity silicon substrates. High resistivity Si behaves as a lossless medium for THz. Due to its lack of donors it prevents absorptive losses, and also due to its large direct band gap, prevents THz photons from being absorbed across the bandgap. Four different glass masks were designed and used throughout this project. It is also important to note that extensive characterization of these antennas [42] along with their use for our group's work on NbN HEB mixers [16] proves their ability to efficiently couple THz radiation to a load placed across its smallest gap.

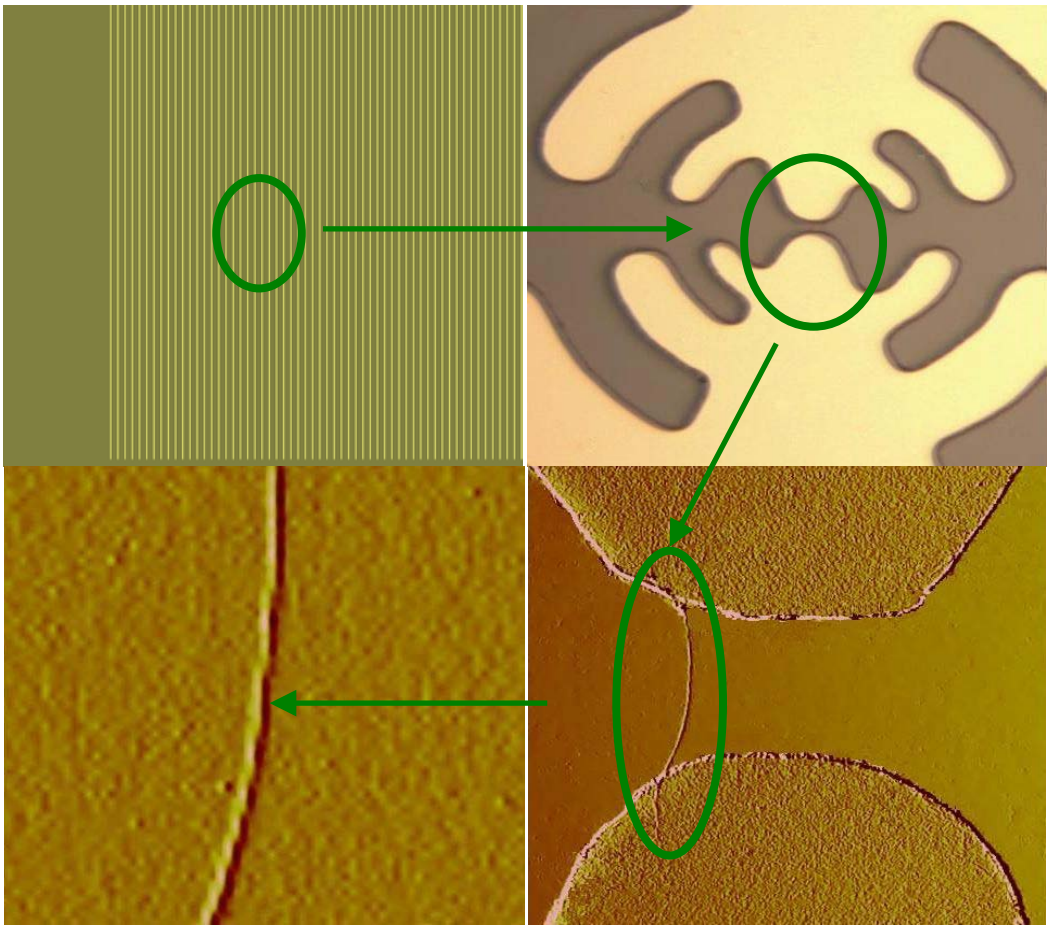

Figure 2.1 Diagram showing the CNT based detector. Above we see the (Top Left) log periodic antenna (LPA) embedded in a co-planar waveguide (CPW), (Top Right) close up of the LPA with the smallest gap marked, (Bottom Right) a SWCNT placed across the gap, and (Bottom Left) a close up of the individual SWCNT.

Below, in Table 2.1, a summary of the key features, characteristics, and the desired objective for each LPA generation are shown. Additionally, Figures 2.2 and 2.3 show the diagram of layers and optical pictures of each generation of devices. LPA1 had much smaller dimensions than all the other generations. These smaller features were used in order to do MW probe measurements on the CNTs. The pitch from the ground to signal conductors was 125 µm and the smallest gap was ranged from 8 - 10 µm. This relatively long gap, when compared to the length of most CNTs used (in solution > 90% 1µm or smaller) made the deposition of CNTs a difficult procedure. The nanotubes measured were not nearly as long,

since all around contact techniques were used in order to reduce their effective length. The top contact layer also served to improve the quality of the contacts thus reducing contact resistance (R_c). Finally, as also summarized in Table 2.1, the main objective of LPA1 CNT based all around contact devices was to use them for MW characterization of the contacts and the SWCNTs through probe measurements. Additionally, responsivity at MW frequencies was recorded.

LPA Generation	Device Dimensions [mm]	Gap Dimensions [μm]		Max. Freq. [THz]	Main Objective
		Width	Length		
1	0.25 x 0.25	10	8-10	1.76	MW. Probe meas. (125 μm pitch)
2	5 x 5	4	1	3.52	Increase operating freq. (3.56 THz)
3	5 x 5	4	1	3.52	Limit CNTs to the gap and Suspend CNTs to reduce Gth.
4	5 x 5	6	3-4	1.76	Obtain single CNT devices

Table 2.1 Summary of characteristics and objectives to be achieved with each LPA generation.

From experiences in [16], [43], and [44] working with antennas from the LPA1 generation, the LPA2 generation was designed with two main objectives in mind: Increase the operating frequency and facilitate individual device handling. For the first, the LPA dimensions were reduced, and several antenna teeth were added (Fig. 2.2). The operational frequency range increased from 0.22 - 1.76 THz (in LPA1) to 0.22 – 3.52 THz (in LPA2). As a result and in order to attempt to obtain shorter CNTs, the gap dimensions (8 μm long by 10 μm wide for LPA1) were also reduced (1 μm long by 4 μm wide for LPA2). Finally, in order to achieve the second objective, the overall dimensions of the CPW were increased, such that each LPA2 device could be scribed into 5 by 5 mm chips.

The LPA3 generation had similar features to the ones previously mentioned for LPA2. The same mask was used for photolithography and as a result, the dimensions and

operational frequencies (see Table 2.1) remained the same. However, once again two unique features distinguished LPA3: A thick oxide trench across the LPA gap and a photo-resist (PR) window around it. First of all, the silicon-dioxide (SiO_2) trench was etched (Fig. 2.3) across the gap of this structure in order to obtain suspended CNTs. The suspension over the substrate meant that the contacts would be the only place for the CNT to release heat, and therefore lower the total thermal conductance (G_{th}) of our devices. The main reason to pursue devices with lower thermal conductance is the already mentioned inversely proportional relationship between thermal conductance and responsivity. Secondly, the photo-resist window across the gap was implemented in order to limit CNT deposition exclusively to this region. Previously [45], it was observed in SEM and AFM images of several LPA2 devices that CNT bundles were not only bridging the LPA across its smallest gap, but also across some of its smaller teeth (Fig. 2.4). This additional and unintentional loading of the antenna was believed to affect its performance negatively. Thus the efforts to limit CNTs to across the smallest gap were pursued with the PR window.

The LPA4 generation was made with a different mask. This time, our aim was to deposit very few or even single/individual SWCNTs that would have ohmic contacts (i.e. low contact resistance). In order to achieve this, and based on experience with previous generations of LPA's the dimensions of the smallest gap were changed to 3-4 μm long by 6-8 μm wide. These dimensions allowed us to deposit very few CNTs, from within the lower tail of the length distribution of the CNTs in solutions (only 10% of CNT were longer than 1 μm). Also, this design did not have the two sets of smaller teeth across which long bundles or individual CNTs were 'shorting' the antenna. Nonetheless, by removing these smaller teeth from the design, the antenna's maximum theoretical operating frequency dropped to 1.76 THz. One last optional feature added to the LPA4 generation design was the addition of a top layer of metal, in order to produce ohmic contacts. By contacting the CNTs with metal from the top 'all around contacts' ensured the complete disappearance or reduction of energy barriers present at the contacts. This technique has previously been employed in order to produce ohmic like contacts for nanomaterials. Not all devices from LPA4 had "all around contacts". In Figure 2.2 bottom right, we can see that near the gap there are two different

edges, each one corresponding to the bottom and top LPA. For a clearer view refer to Figures 2.3 and 2.5.

Figure 2.2 Optical pictures of the four generations of LPA used in this work: LPA1 (Top Left), LPA2 (Top Right), LPA3 (Bottom Left), and LPA4 (Bottom Right).

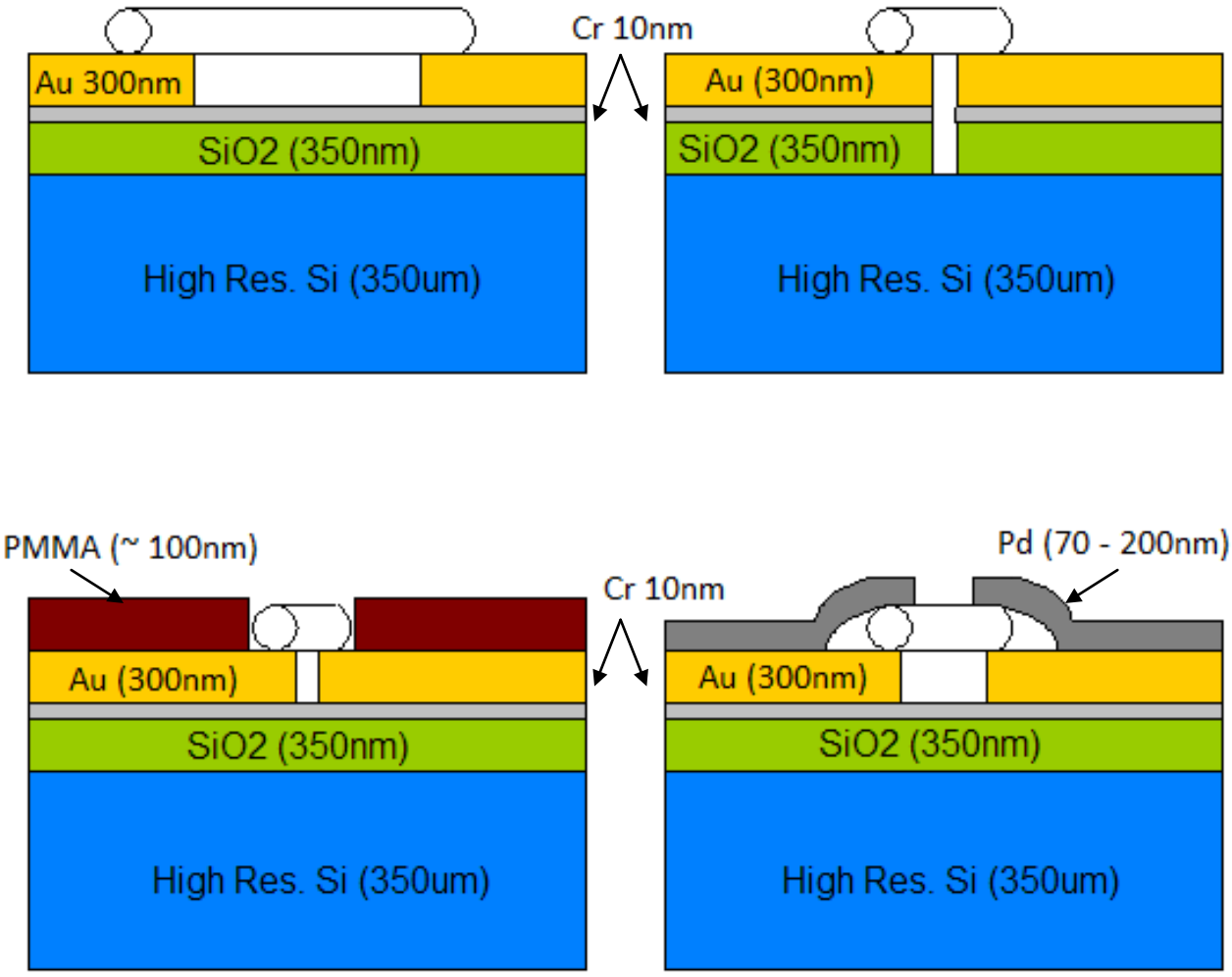

Figure 2.3 Diagrams of cross sections (at the LPA smallest gap) of the four generations of LPA used in this work: LPA1 (Top Left), LPA2 (Top Right), LPA3 (Bottom Left), and LPA4 (Bottom Right). Note gaps sizes are drawn to scale relative to each other.

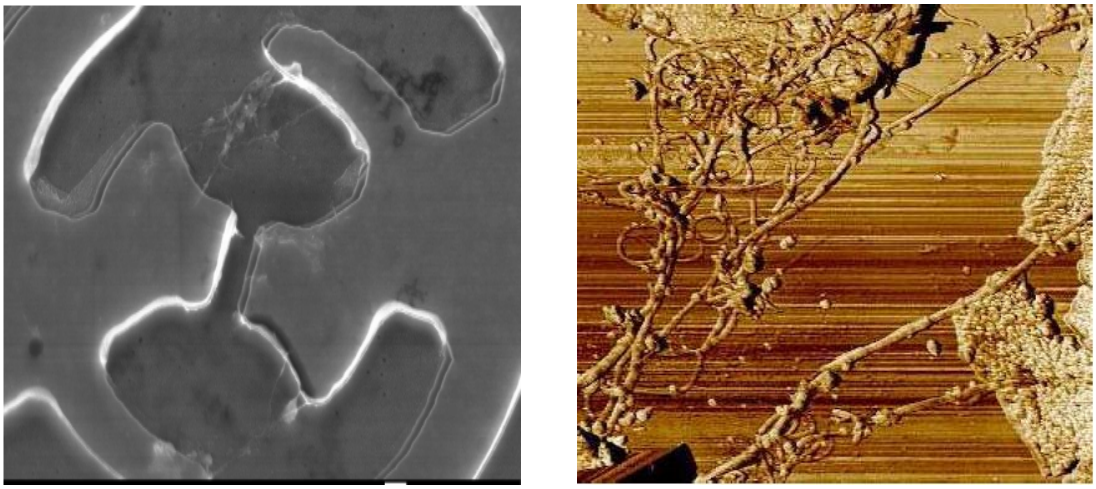

Figure 2.4 SEM (left) and AFM (right) images illustrating CNT bundles bridging outer teeth of LPA2. For reference, the gap (1µm) in the SEM image is located at the center of the picture, while the one in the AFM image is to be found at the top right corner of the photo. Obtained from ref. [45].

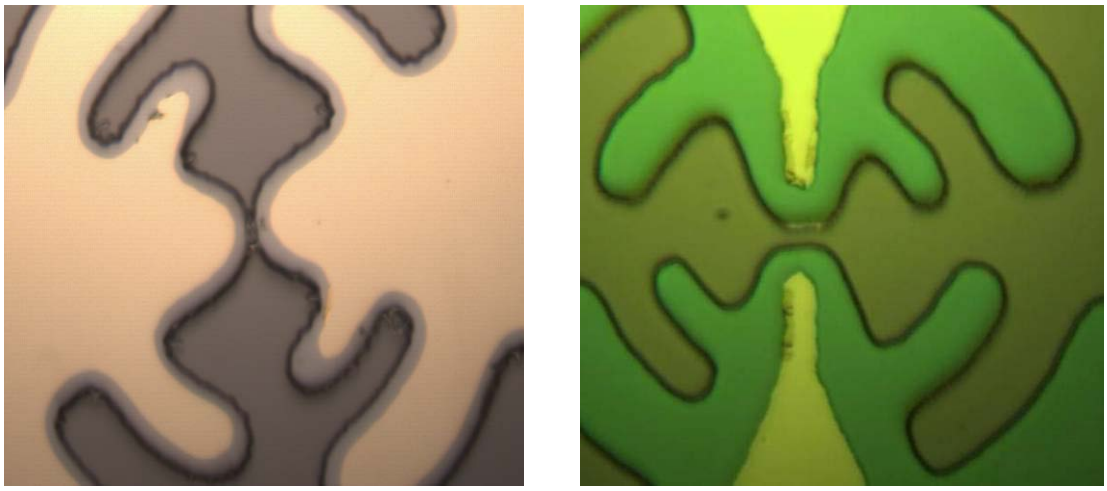

Figure 2.5 Optical pictures of two different top contact configurations for LPA4. The first one (left) was done by simply aligning the mask on top of a previously deposited first layer of metal and then overexposing the photo-resist to UV. Final gap size and effective CNT length achieved was ~1 µm. The second configuration (right) was done using a step mask process. The final gap size and effective CNT lengths obtained ranged from 3 to 4 µm.

2.1.2 CNT Placement: Dielectrophoresis

Dielectrophoresis (DEP) is the process in which a force, due to a non-uniform electric field, is applied on a dielectric particle [46]. Most particles exhibit dielectric forces independent of the presence of charge in them. However, the strength of this force is greatly dependent on the geometry of the particle, strength of field, frequency of oscillating field, dielectric properties of the particle and of the medium, among other things. DEP has been used extensively for manipulation of bacteria, other biological organisms [47], nanoparticles, nanowires, and even CNTs [48]. Several of the CNT DEP studies concentrate on a variety of issues: Calculating and predicting DEP forces [49], reproducibility of CNT placement [50], electrode shape influence [51], separating metallic from semiconducting CNTs [52], influence of other DEP related variables (substrates, CNTs with or without surfactants, different metals for electrodes, thickness of SiO_2, etc) [53], real-time control of DEP process [54], and large scale assembly of CNT based devices [55]. In this project an extensive survey of the literature, and even more extensive experimentation have been done, in order to define DEP parameters that were optimum for our ultimate objective: To be able to place quickly, cleanly, and well contacted, a few individual CNTs across the smallest gap of our LPA's.

Metallic SWCNTs used in this work were obtained from two vendors: Cheap Tubes [56] and Brewer Science [57]. Different DEP parameters, as well as solution preparation procedures and concentrations were used for CNTs from each company. In general, CNTs were suspended in de-ionized water (DIH_2O) and then diluted to the desired concentration (from mgs/ml to ngs/ml). Subsequently, CNTs in solution were centrifuged for 2 – 4hrs at 5000RPM, in order to rid the solution of larger impurities and to decrease the CNT concentration even further. Afterwards the supernatants, which still contained CNTs, were removed, sonicated, and used in the DEP process.

The DEP process, shown in figure 2.6, consisted in applying an AC voltage (typically 1-10Vpp and 5-50MHz) across the LPA. A small drop of CNT solution (usually b/w 0.1 – 1μl) was then deposited across the smallest gap of our LPA's. The DC current and resistance were monitored in real time by applying a small bias through a bias tee, in order to determine when a CNT or a few CNTs had bridged the LPA gap (Fig. 2.7); typical values for a well contacted single CNT was in the range of hundreds of KΩ at room temperature [35]. After

the desired resistance was reached, the AC voltage was halted, and the remaining drop blown away with nitrogen gas. CNTs remained attached to the metal contacts due to strong Van der Waals forces, which also cause them to easily entangle and form thicker ropes or bundles. Throughout the duration of this project hundreds of CNT devices were contacted. Most of these served to simply refine several different DEP related parameters: Tubes from different vendors, solution concentrations, AC voltage amplitude and frequency, DC bias, DEP time, etc. Additionally, we extensively used SEM and AFM in order to characterize our results from DEP (Fig. 2.8). In general the values of resistance obtained ranged from a few KΩ ,for thickly dense bundles of tubes, to hundreds or even thousands of KΩ for some single CNT devices.

Finally, the devices were annealed at 200 for 2 to 4 hours. Annealing has been shown to improve the quality of the metal-CNT interface [25] and it almost always reduced the resistance of the devices. As fabricated per the procedures described above, typical resistances measured for devices ranged from 10 – 200 KΩ. A more complete description of the resistance of the measured devices at several temperatures will be presented in the next section: 2.2 Device Characterization.

After all fabrication steps were completed, wafers were scribed into individual 5 x 5 mm chips and then proceeded to be tested at DC, MW, and THz frequencies. On occasion, such as for some DC and MW measurements, the testing could be done on-chip by using a probe station, but usually in order to proceed with cryogenic tests, individual devices were mounted in a metal block and placed inside an IR-Labs cryogenic dewar (Fig. 2.9). Connections between the chip, block, and dewar were made using indium wires, SMA connectors, and coaxial cables respectively.

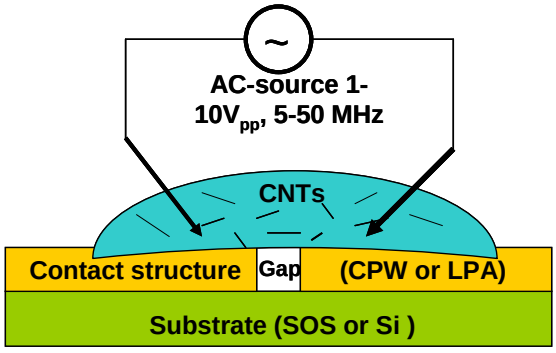

Figure 2.6 Simple DEP schematic.

Figure 2.7 Example of DC current being monitored over time. The ‘base-line’ resistance corresponds to the medium (drop of solution), the big step-like jump corresponds to some CNTs bridging the gap; subsequent steps corresponds to addition of more CNTs.

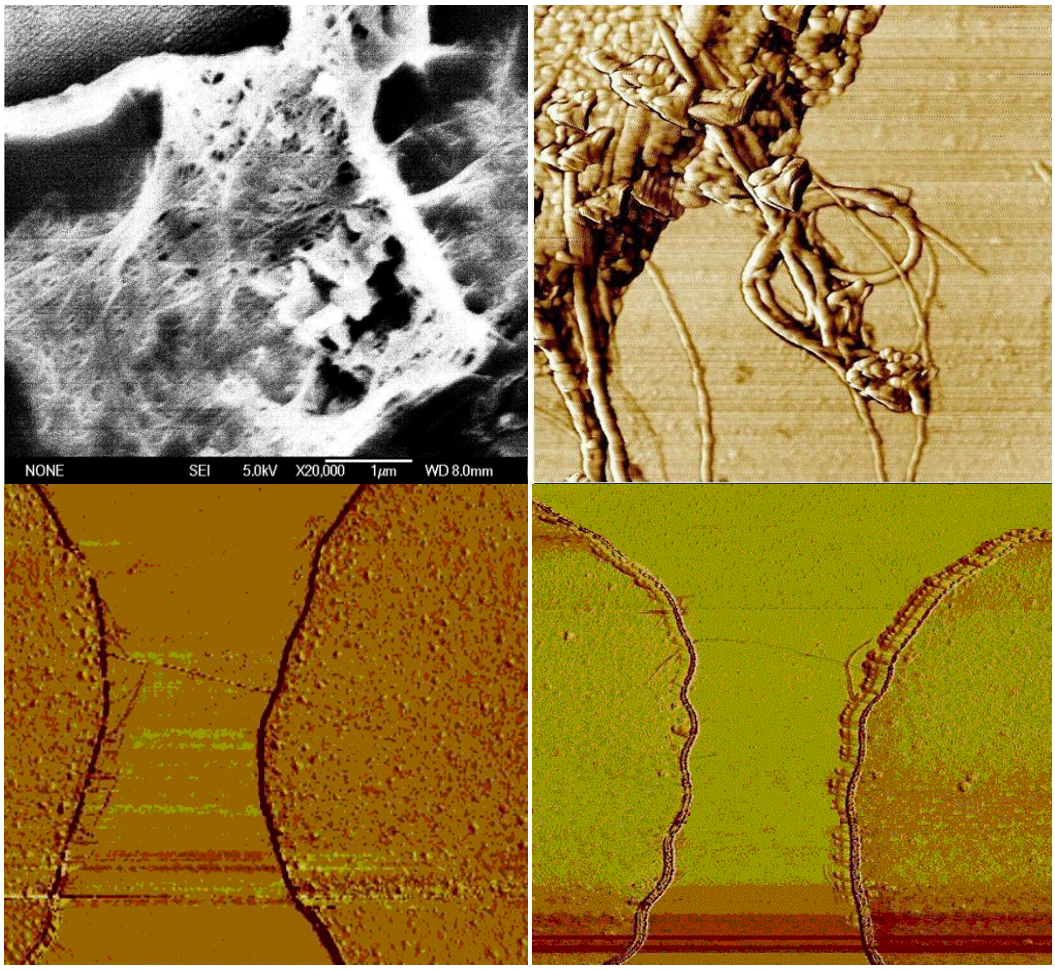

Figure 2.8 SEM and AFM pictures of various CNT based devices made by DEP. Top left: Thickly dense mat of bundles of CNTs. Top right: Entanglement of CNT bundles and single CNTs. Bottom left and right: Single CNT bridging the smallest gap of an LPA.

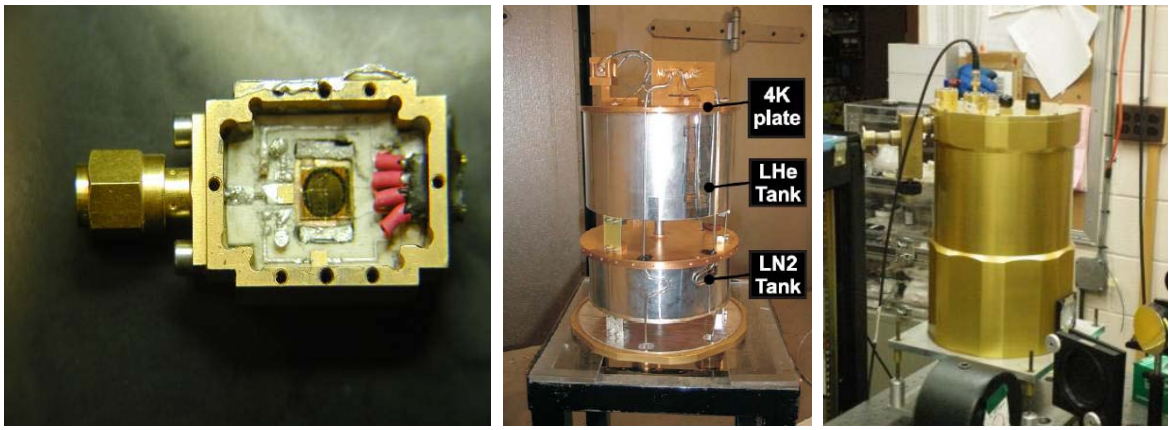

Figure 2.9 Metal block (left) and cryogenic dewar (center and right) where 5 x 5 mm chips were mounted for testing.

2.2 Characterization of CNT Devices

We now proceed to describe the experimental setups and present and analyze the results obtained from our testing of several CNT based devices; measurements were done at DC, MW, and THz frequencies. The DC testing consisted in measuring the IV characteristics at fixed temperatures (290K, 77K, and 4.2K) and occasionally, at several more temperature intervals. The MW testing consisted of two main measurements, direct detection experiments and S-parameter measurements. Finally, the THz testing consisted of direct detection THz experiments at fixed temperatures and as a function of increasing temperature.

2.2.1 DC Characteristics

2.2.1.a Experimental Setup

The DC testing was done using the two-wire, and in some cases the four-wire measurement configurations, of a source meter (Keithley 2600) controlled by a LabView program. The four-wire setting was used in order to obtain more accurate and steady values of very small currents (in some cases nA). Additionally, an Omega temperature sensor (Fig. 2.10) was attached to the metal block and interfaced with the source meter through LabView. This setup allowed us to record accurately the IV characteristics of our CNT devices as a function of temperature (4.2 – 300 K).

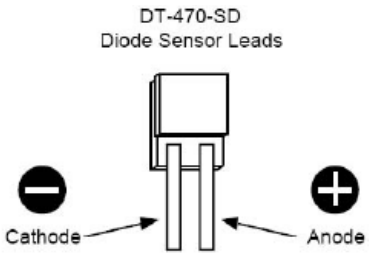

Figure 2.10 Diagram of Omega temperature sensor attached to metal block

2.2.1.b Results and Analysis

In this section the results and analysis of the DC testing of several CNT devices are presented. First, the IV curves of two devices (C4 and 3D3), representative of the two kinds of IV results obtained for all the others, are shown and analyzed in Figures 2.11 and 2.12. Four graphs are presented for each device as a function of bias voltage: current, resistance, differential conductance (*dI/dV*), and the second voltage derivative of the current (d^2I/dV^2). Second, the IV characteristic of all the other devices which were also measured at MW and/or THz frequencies are also shown here. Table 2.2 lists all the tested devices in this work and their resistance at operational temperatures of 300K, 77K, and 4.2K.

As mentioned earlier, two kinds of IV results were obtained through-out this work; device C4 (from the LPA2 generation) and 3D3 (from the LPA4 generation) were representative of each type. The difference in these two lies in the quality of the contact between the CNT-metal interfaces. Depending on how well the nanotube is contacted, one can have large energy barriers, which translate to high contact resistance values. This contact resistance adds to the inherent CNT resistance and in some cases it affects the transport properties of the device. This kind of device (i.e. C4) with 'bad contacts' will be referred to through-out this work as *'nonlinear'*. The case in which current saturation, a distinct property of the nanotubes themselves, is observed in the devices will be referred to as *'ohmic."* These two terms thus describe *the type of contacts* that was obtained to the SWCNTs.

Furthermore, analyzing *nonlinear* device C4 (Fig. 2.11), it is evident from the current and differential conductance plots, that its non-linear behavior arises from the presence of a ZBA [38]. Then, the rising current with increasing voltage characteristics can be interpreted as being due to tunneling through an energy barrier generated by the metal-CNT interface. At higher bias voltages, the tunneling current increases and the resistance decreases, and at

lower temperatures, fewer electrons are able to tunnel for a given voltage and as a result the current decreases and the resistance increases. Additionally, from the second voltage derivative of the current (d^2I/dV^2). one can start predicting how the diode mode detection would behave as a function of voltage and temperature. We should expect high MW detections at low bias voltages and low temperatures. Device C4 did not behave as a diode detector, as will be shown later; nonetheless, its d^2I/dV^2 is representative of other devices which did.

Moving on to describe the *'ohmic'* device 3D3 (Fig. 2.12) we also note the presence of a non-linearity on the IV curve at high voltages; however, in this case the overall curvature is opposite (concave down). This non-linearity is evidence of current saturation at high voltages; as described earlier, OP-electron scattering processes becomes present after around 160mV for a single CNT. Oppositely, for small bias voltages the current increases linearly (i.e. therefore named 'ohmic') until it reaches the saturation point. Additionally, taking into account the theoretical current saturation for a single SWCNT (~25μA [12]), it can be deduced that more than one nanotube is present across the gap. In fact, AFM images (Fig. 2.13) reveal that device 3D3 had a single CNT and a three-CNT bundle across its gap. AFM analysis was very helpful in general in order to determine the number of tubes present and their diameters; nonetheless, this information did not clarify which one (the single tube or the bundle), if any of these two, dominates in transport.

Finally, the current saturation of device 3D3 is evidence of the intrinsic properties of the CNT, instead of the contacts; this suggests that the energy barriers at the contacts have been greatly reduced or even disappeared. Such performance can be attributed to a better and higher quality metal-CNT interface. It is also important to notice, from the resistance and conductance plots, that at low bias voltages and low temperatures, electrons do not have enough energy to tunnel through the much smaller contacts barriers. As a result a decreased current and conductance presents themselves as an increased resistance and a dip in the conductance, respectively near the zero bias. This ‘barrier’ at low temperatures and low bias voltages will have an effect on how the device behaves detecting in the diode mode at MW or even THz frequencies.

Lastly, from the d^2I/dV^2 plot, a measure of the device's nonlinearity is obtained. In this plot it is evident that higher values of d^2I/dV^2 are obtained under low bias and low temperature conditions. This effect is attributed to the presence on the same barriers present in *nonlinear* devices (i.e. C4).

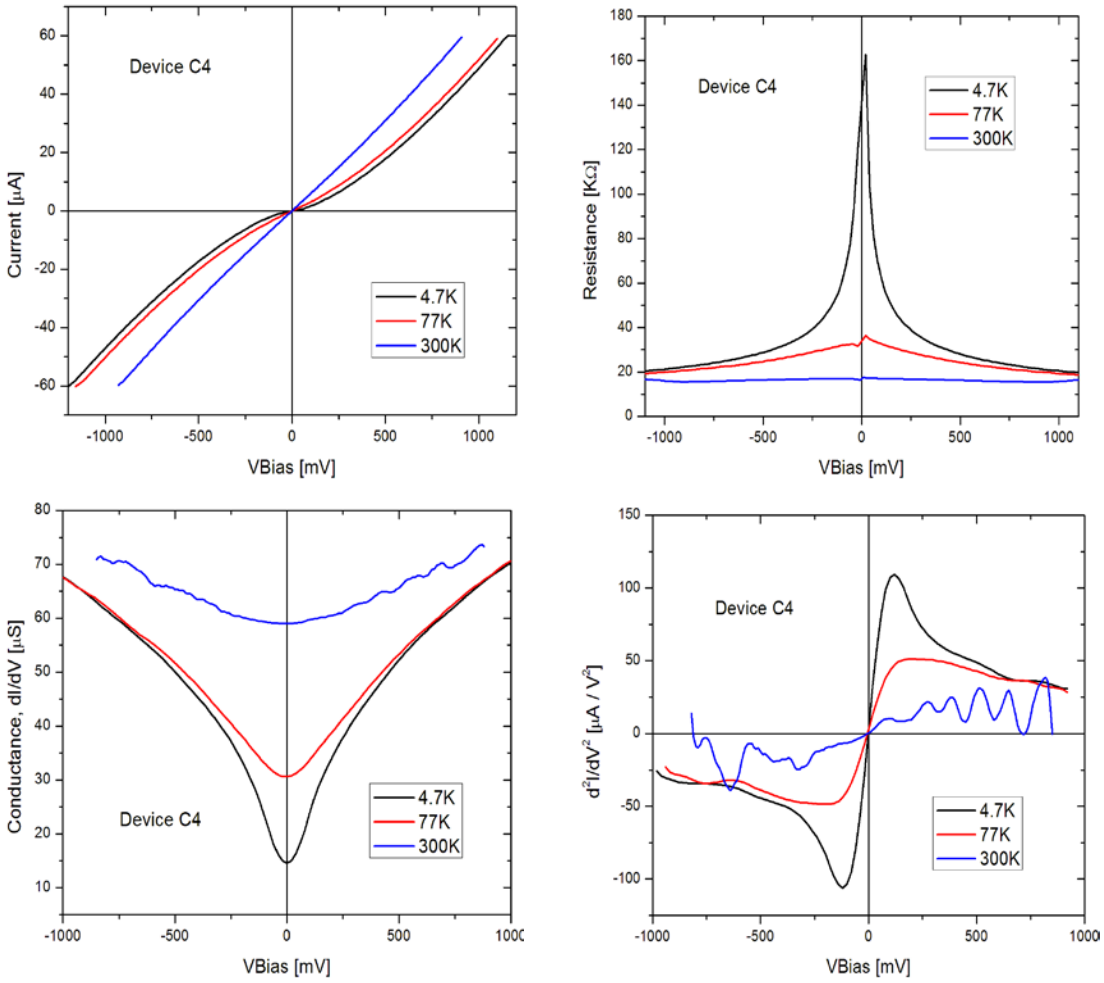

Figure 2.11 'Non-linear' device C4-LPA2 DC characteristics at 4.2K (black), 77K (red), and 300K (blue): Current (top left), resistance (top right), conductance (bottom left) and d^2I/dV^2 (bottom right) as a function of bias voltage.

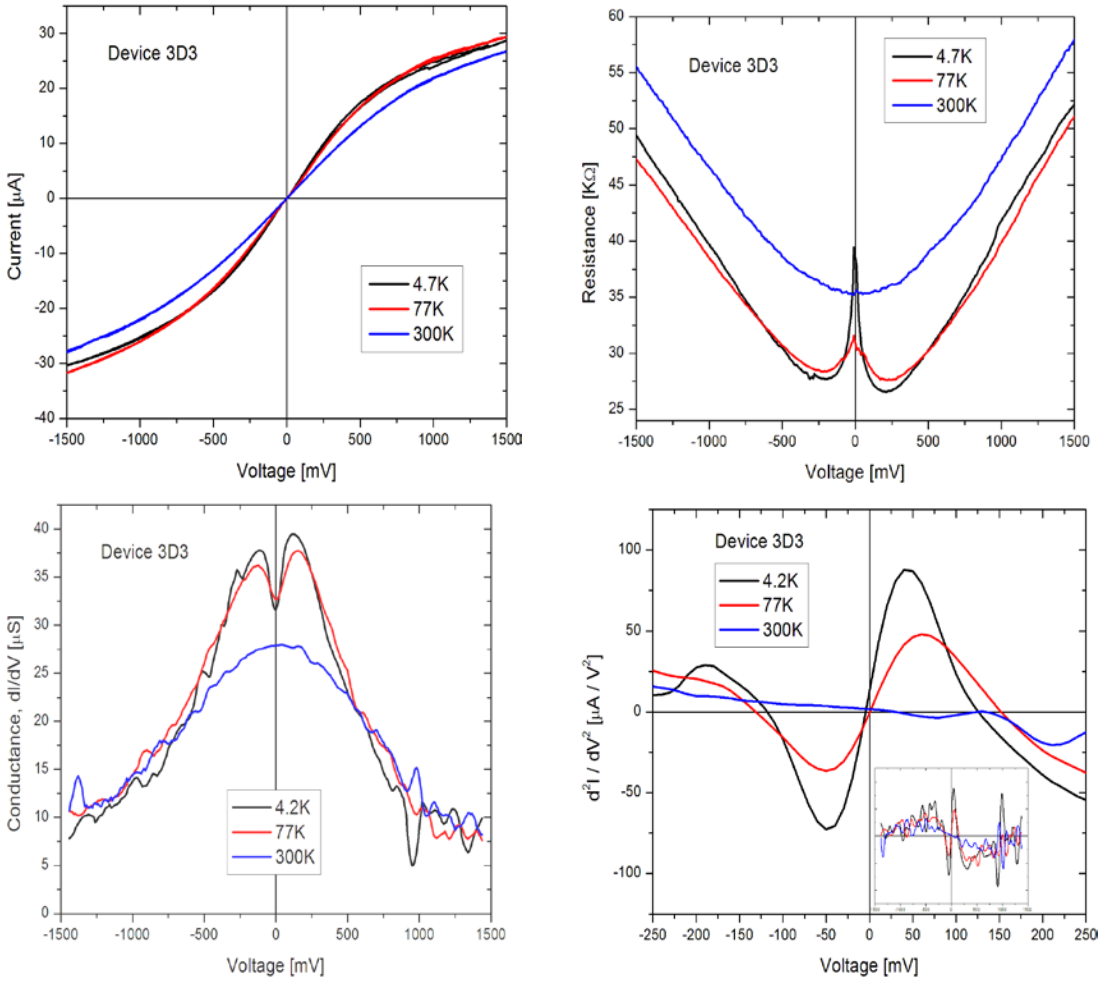

Figure 2.12 'Ohmic' device 3D3-LPA4 DC characteristics at 4.2K (black), 77K (red), and 300K (blue): Current (top left), resistance (top right), conductance (bottom left) and d^2I/dV^2 (bottom right) as a function of bias voltage.

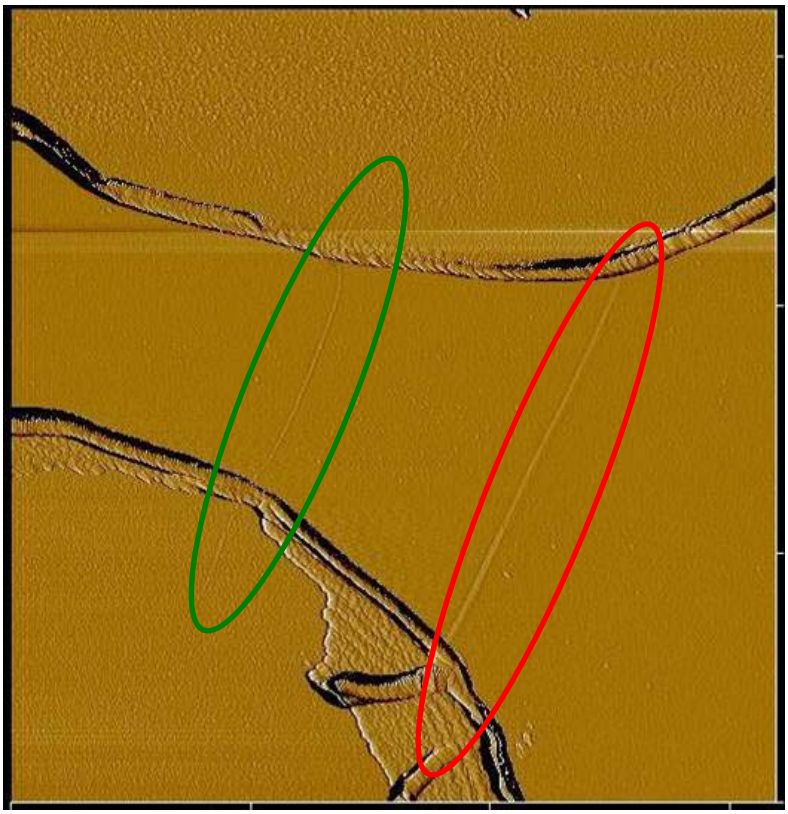

Figure 2.13 *Ohmic* device 3D3 from the LPA4 generation which only had a bottom layer of metal. Notice the two branches of CNTs across the gap. The one in the middle (inside green circle) is a single CNT of 1.5nm diameter, while the one towards the right (inside red circle) is a 5nm diameter CNT bundle.

Having described the nature of the DC characteristics of *nonlinear* and *ohmic* devices, we move on to present devices tested at MW and THz also. IV and RV curves at their respective operational temperature are shown in Appendix 2.; in this section a summary (Table 2.2 and 2.3) of their resistances –at very low voltages (i.e. 5 -20 mV)– and the tests performed on each one are presented. Also, note the legend below Table 2.2; it describes other specifics about each device, such as whether a device behaves as *nonlinear* or *ohmic*, or whether it had a top layer of Pd in addition to the Au regular bottom layer. A total of 42 devices' resistance are shown below; 25 from the LPA1 generation, 3 from LPA2, 8 from LPA 3, and 6 from LPA4. Resistances at room temperature vary from a few tens of ohms (i.e. device D3A2) to hundreds of kΩ. Amongst all these devices, a wide variety of CNT

configurations was obtained, from a single SWCNT to dense and complicated networks of tubes. The resistance provides an insight into the CNT configuration (i.e. lower resistance means more nanotubes in parallel) of each device; however, it can also be misleading since it describes the 'quality' of the contact as well (i.e. different values of contact resistances). With this in mind it is important to look at the legend when attempting to draw conclusion from Tables 2.2 and 2.3.

LPA Generation	Device	Resistance at V=0* [KW]			Measurement
		300K	77K	4.2K	
1	**D4A3**	0.47			S-Para / MW S_v
	A2A1	10.5			
	A1B1	15			
	A5C2	15			
	B5B1	27			
	A6A3	40			
	D3A2	0.05			S-Para
	D3A3	0.05			
	D3A1	0.09			
	D3C2	0.11			
	D3B3	0.15			
	D3B1	0.20			
	D3C3	0.20			
	B7C1	0.66			
	D2C1	0.70			
	D2C2	0.83			
	B2B1	0.90			
	B2C3	1.00			
	C6C2	1.20			
	B7A3	1.30			
	A3C3	1.50			
	B7C3	1.65			
	C3C3	6.7			

Table 2.2 Summary of DC characteristics and measurements performed of all devices tested from LPA 1 generation.

Legend:

Bold Text	- *Ohmic* Device
Non-Bold Text	- *Nonlinear* Device
Blue Text	- Top layer of Pd added
Black Text	- Bottom Au layer only

LPA Generation	Device	Resistance at V=0* [KW]			Measurement
		300K	77K	4.2K	
2	C1	8.1	24	40	THz S_v
	C4	17	36	162	
	C5	58	124		MW S_v
3	4A1	24	47		THz S_v
	4C4	20	31		
	1C4	85	190		
	3C3	54	117		
	4B2	42	110		
	4A2	10	22	200	
	4A3	50	97	870	
	2B1	16	28		
4	**F2**	360	20 000	150 000	MW S_v
	C2	130	135		
	F2-R	140	140	10 000	
	C3	24		90	
	3D3	36	32	40	DC

Table 2.3 Summary of DC characteristics and measurements performed of all devices tested from LPA 2, 3, and 4 generation.

2.2.1.c Temperature Dependent Results

The DC characterization and the analysis presented in the section above only shows three selected temperatures (4.2K, 77K, and 300K). However, in order to obtain a more accurate and complete description of how the devices operated, and to predict their behavior at MW and THz frequencies, temperature dependent IV characterization of *nonlinear* and *ohmic* devices, also took place. The current-voltage and resistance-voltage characteristics, both as a function of temperature, are shown in Figures 2.14 and 2.15. Additionally, in Figure 2.16, three resistance-voltage-temperature three dimensional plots are shown. The curves in Figures 2.14 - 2.16 are from devices from the LPA2 (C1, and C4) and the LPA4 (3D3, and F2) generations.

Among the *nonlinear* devices, the previously discussed contact resistance based nonlinearity can be observed. Some of them exhibited a greater non-linearity than others.

This is due to the inability to reproduce identical CNT-metal contact interfaces. This issue was addressed with the addition of an extra top layer of metal. The top contact layer helped with better contact reproducibility. It is important to note that for devices C1 and C4, the IV curves appear to level-off or curve downwards at high voltages; this effect is not due to any CNT based property, but simply indicates that the compliance of the source meter was reached.

For the *ohmic* devices, the ZBA presents itself in both cases (3D3 and F2) only at the low bias; this effect can be observed from the drastic resistance increase (Fig. 2.14 and 2.15). As mentioned earlier, at the low bias and low temperature, electrons do not have enough energy to tunnel through the contact barriers. For device 3D3, the ZBA becomes apparent at temperatures lower than 200K and it gradually increases. On the other hand, for F2, the ZBA does not show up noticeably until about 40K (see Fig. 2.16), after which it drastically increases. This sudden resistance increase is attributed to the fact that F2 is a single CNT device (Fig. 2.22) with different contacts and number of tubes than the ones of 3D3. Besides, neither of these two devices had a top layer of Pd, thus making contact resistance effects hard to predict and compare. Finally, for reference we emphasize here (and in Table 2.2 and 2.3) which measurements were performed on devices presented in Figures 2.14 - 2.16. Devices C1 and C4 were used for THz direct detection measurements, F2 was measured at MW for direct detection also, while 3D3 was simply measured at DC; the latter simply served to refine DEP parameters. Nonetheless, measuring its DC characteristics as a function of temperature will allow us to predict the theoretical performance of similar devices as detectors.

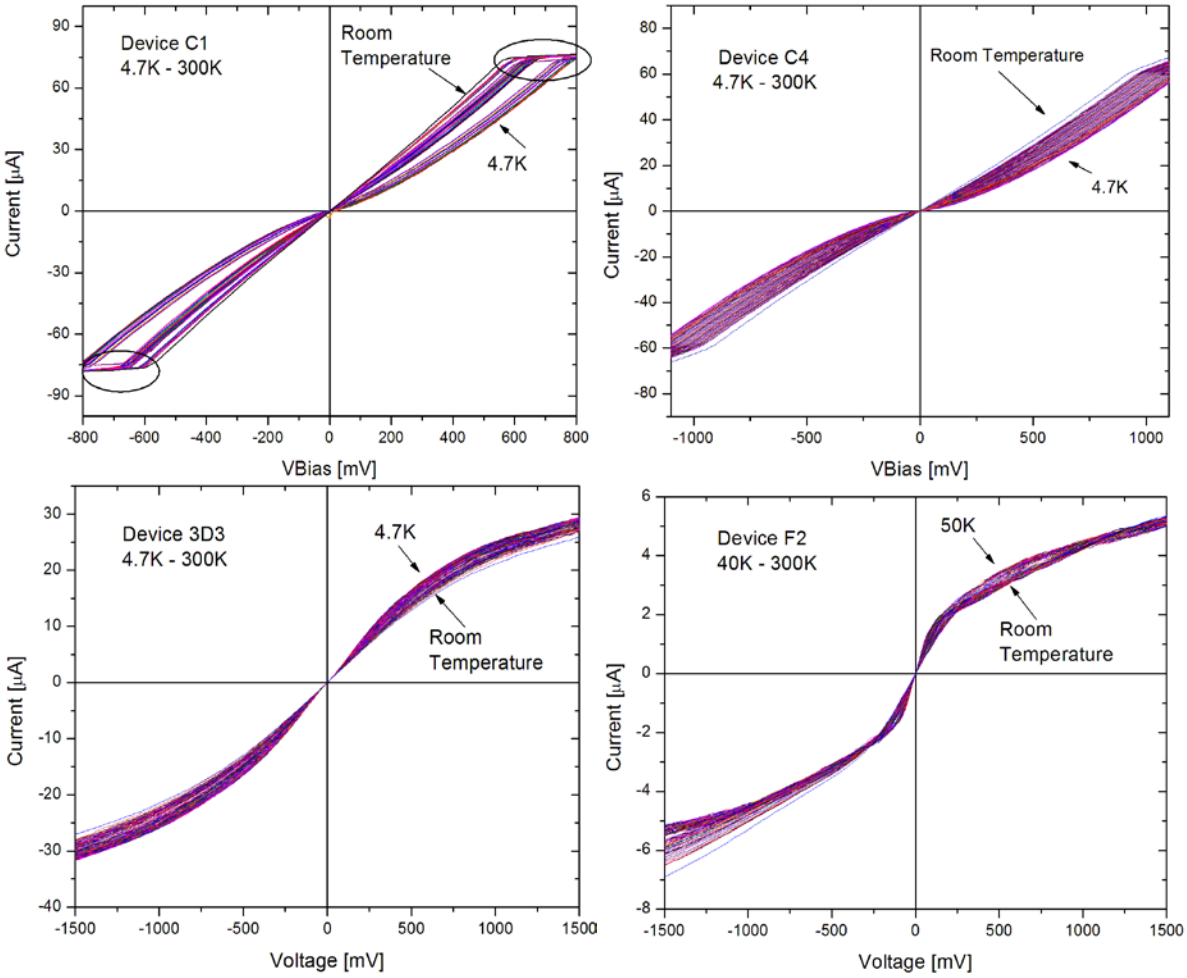

Figure 2.14 IV characteristics as a function of temperature for three LPA2 devices –C1 (top left), C4 (top right), and C3 (middle) – and two LPA4 devices – 3D3 (bottom left) and F2 (bottom right).

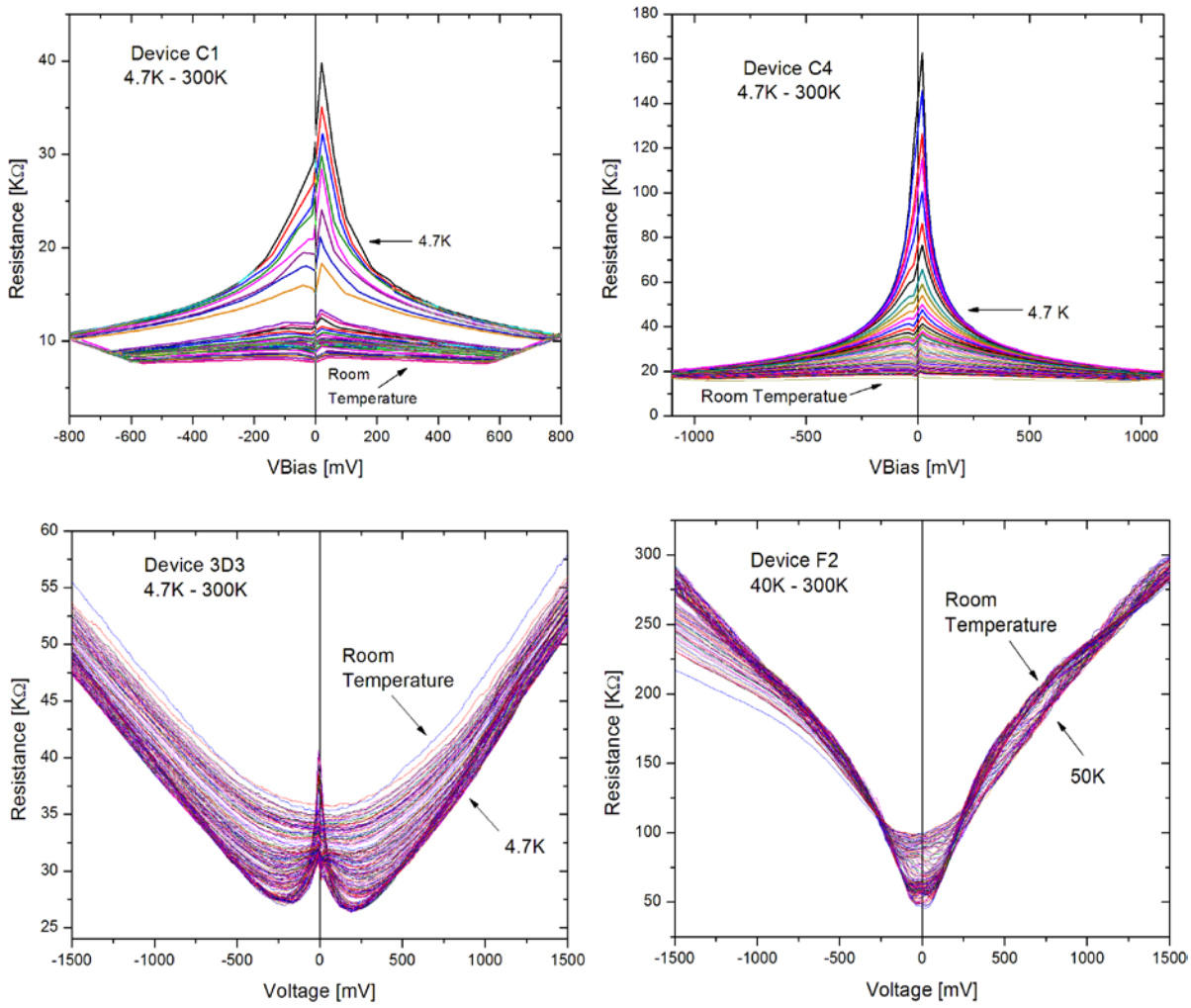

Figure 2.15 RV characteristics as a function of temperature for three LPA2 devices –C1 (top left), and C4 (top right)– and two LPA4 devices –3D3 (bottom left) and F2 (bottom right).

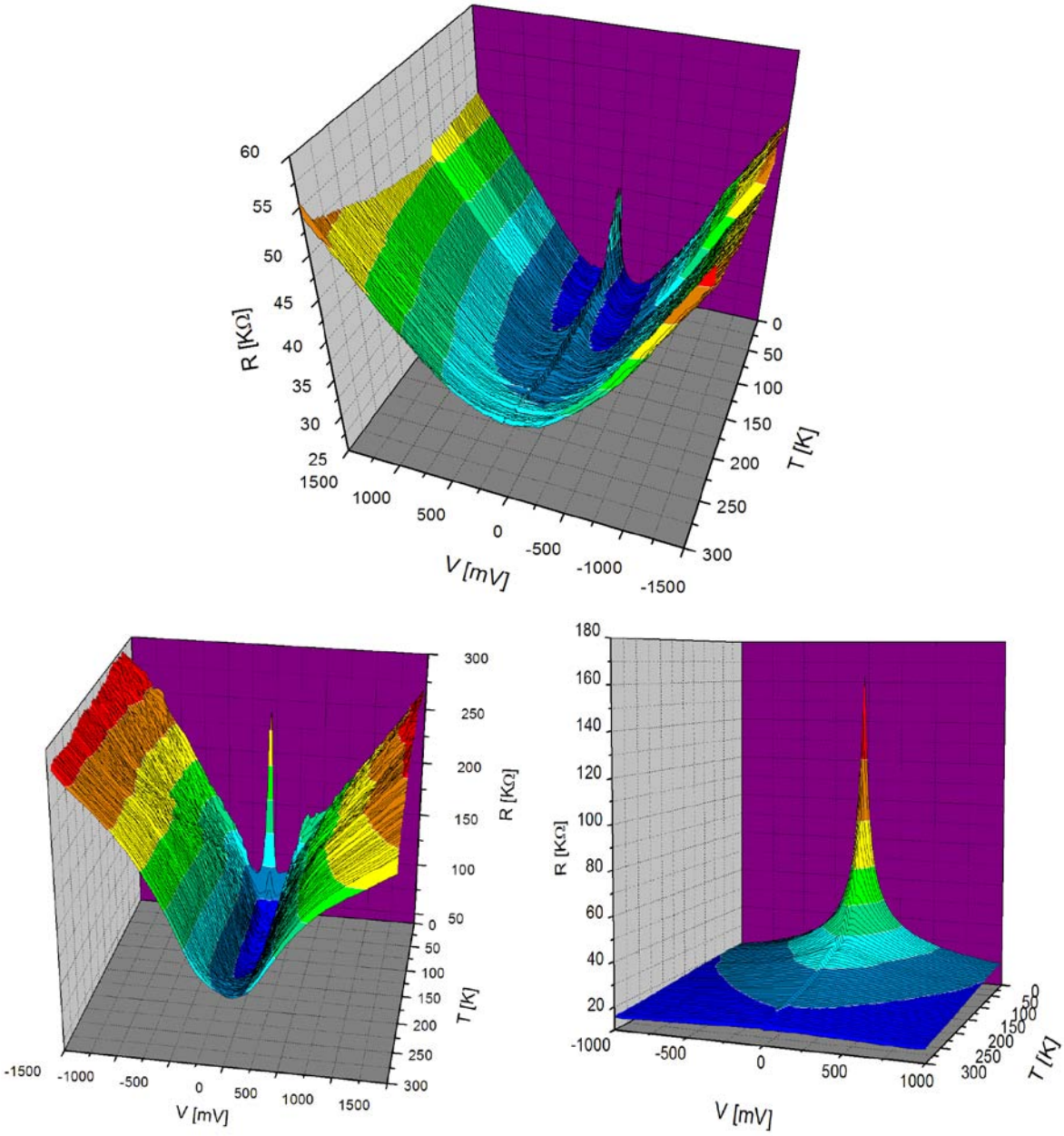

Figure 2.16 Current-voltage-temperature graphs for 3D3 (top), F2 (bottom left), and C4 (bottom right). Note opposite trend for resistance as a function of voltage between *nonlinear* (C4) and *ohmic* (3D3 and F2 at higher temperatures) devices, and a similar trends at low voltage and decreasing temperatures.

2.2.2 Microwave Direct Detection

2.2.2.a Experimental Setup

The direct MW response was measured by recording changes in current across a 100KΩ resistor −connected in series with the CNT based device− as an RF signal was turned ON and OFF. This current difference, ΔI, or voltage, ΔV, along with the known amount of power delivered to the device was used to experimentally calculate the detection responsivity. The setup below (Fig. 2.17) shows the components used in this technique: A Keithley source meter, a lock-in amplifier, a bias tee, a MW generator, a lock-in amplifier, and a function generator.

As can be seen in the schematic, the DC bias and the MW signal were fed to the device through a bias tee. Additionally, the MW signal was modulated by a function generator, while the DC bias also passed through a 100KΩ resistor. This passive component was connected in series with the DUT, and thus changes in the DUT's IV characteristics (produced by the RF) could be measured across it. For this purpose, both ends of the resistor were connected to a lock-in amplifier, whose reference signal was the one modulating the RF pulse. Therefore, any voltage measured across the 100KΩ resistor was a direct response to changes in the DUT's characteristics caused by the incoming RF signal. The 'detected' lock-in voltage was recorded for several RF frequencies and powers, as well as device temperatures and bias voltages. Finally, in order to calculate the experimental responsivity, the previously introduced expression (Equations 12 and 14) was used.

$$(25) \qquad S_V = \frac{\Delta V}{P_{MW}} = \frac{V_{MWon} - V_{MWoff}}{P_{MW}}$$

Furthermore, like in the DC characterization setup, the source meter and lock-in amplifier were interfaced through LabView; this allowed for fast and accurate recording of responsivity as a function of DC Bias. The direct MW responsivity measurement was done with devices either mounted in the block and dewar (Fig. 2.10) or directly probed. Both configurations had different advantages and challenges. For example, in-dewar measurements allowed us to cool devices to cryogenic temperatures (300K, 77K, 4.2K)

which decreased scattering and increased important nonlinearities; however, MW power was lost through the indium wires, and parasitic reactances in the block configuration had an effect on the frequency response at the higher MW frequencies. Therefore, these measurements were limited to a maximum frequency of 3 GHz. On the other hand, the opposite situation affected the probed measurements. In this case, good impedance matching through out the entire cascade (from the source generator to the chip) of components was achieved; however, we were limited to performing experiments at room temperature only. The maximum frequency in the probe measurements was 26 GHz.

As will be presented next, direct response decreased drastically at higher temperatures, therefore the responsivity of probed devices (measured at 300K only) was small.

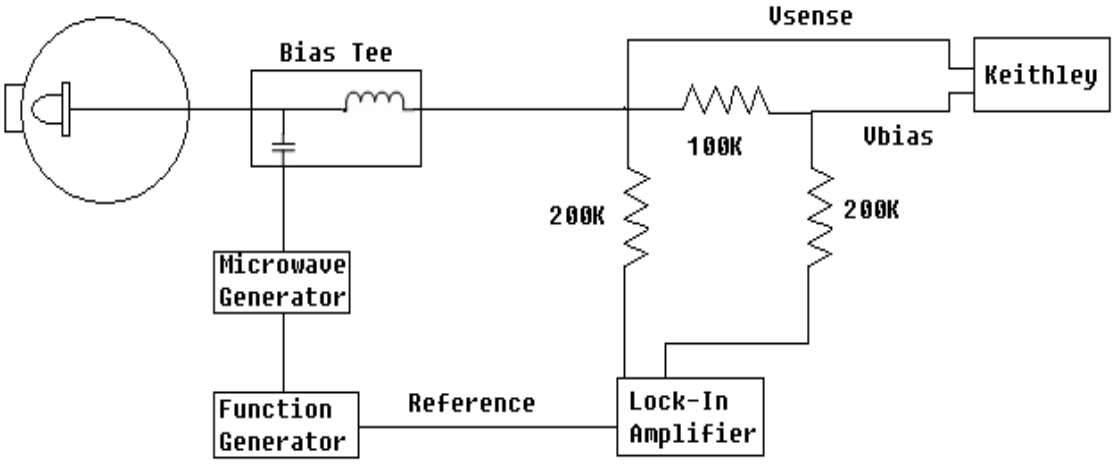

Figure 2.17 Schematic of experimental setup used for MW direct detection.

2.2.2.b Responsivity Results

Several devices (see Table 2.2 and 2.3), mainly from the LPA1 and LP4 generations, were tested for direct MW responsivity. The first ones (from LPA1) were measured on a probe station, while the latter ones (from LPA4) inside a cryogenic dewar (These devices will be referred to as 'in-dewar'). The recently discussed advantages and disadvantages of each testing configuration were evident in the results. Moreover, AFM images of these devices (Fig. 2.18 - 2.21) allowed us to identify the type of CNT arrangements obtained from DEP. Height analysis of the AFM data revealed that in several cases, such as for devices F2

and C3, single CNT deposition was achieved. More details about the CNTs in each device are provided in the caption of each figure.

Overall, MW responsivity was measured as a function of RF frequency (Fig. 2.22 and 2.23), RF power (Fig. 2.24), and bias voltage (Fig. 2.25 and 2.26). In this section, the results and general discussion are presented; more in depth analysis as well as evidence of diode and bolometer model behaviors, will be shown in Chapter 3. Once again for details on the LPA generation to which devices belonged, their resistance at certain operating temperatures, and to correlate results with the type of device (i.e. n*onlinear, ohmic,* or whether a top metal layer was present) refer to Tables 2.2, 2.3 and Appendix 1.

First, we discuss the MW detection as a function of frequency. For the devices tested inside the dewar (Fig. 2.22), the measured response was fairly flat up to 3GHz. Maximum responsivity values ranged from 1000 to 3000 V/W at 4K, 10 to 1000 V/W at 77K, and 100 to 300 V/W at room temperature. The wide range and high fluctuation of these peak responsivity values at each temperature was due to the different IV characteristics that arise from different CNT configurations. The contacts also take an important role in this process. For example, by simply improving the contacts of device F2 through an additional 2-hour annealing session, IV characteristics with lower contact resistance (Rc) were obtained, and responsivity then increased by a factor of 10 at 77K and almost 100 at 4.2K. This annealed device has been treated as a 'different' device and throughout Chapters 2 and 3 has been referred as F2R. Moving on to examine the probed devices (Fig. 2.23), it is evident that the response was also fairly flat up to about 15GHz, after which in some cases it gradually increased or decreased. This high frequency responsivity behavior is not well understood. S-parameter measurements have also been done on these same devices in an attempt to understand how the CNTs and contacts behave along this frequency range. These measurements will be discussed in the next section. Furthermore, the responsivity values from the probed devices, only measured at room temperature, ranged from almost 100 to 200 V/W below 1GHz. This range of response values is consistent with the responsivity of 'in-dewar' devices measured under similar conditions (i.e. at 300K and low frequencies). Comparisons between results at cryogenic temperatures and those at room temperature are difficult to make since the IV characteristics changed drastically.

Next, we proceed to qualitatively analyze the responsivity of devices as a function of MW power (Fig. 2.24). This measurement was done in order to confirm that the devices remained in their linear regions of operation while testing. All plots from Figure 2.24 showed the clear saturation of responsivity as MW power was increased. Note that the equations employed to predict the responsivity are valid only in the small signal range. Thus we expect the responsivity to saturate as the microwave power is increased beyond the value for which the microwave voltage swing exceeds that required by the small signal approximation. Subsequently, the power used for frequency and bias dependent measurements was set such as to keep devices in their linear regions. Additionally, we examine the point at which device responsivity starts to decrease (i.e. roll-off). For the 'in-dewar' devices the roll-off point varied from -25 to around -5 dBm while, for all probed devices responsivity started to decrease at around 0 dBm. The different roll of points from the 'in-dewar' measurements were mainly due to their lossy and parasitic nature already mentioned. A particular situation where clear evidence of varying roll-off points between devices can be observed is between devices F2 and F2R. On these plots in Figure 2.24 the response of device F2 barely begins to decrease at -5dBm, while the one of F2R does so at around -20 dBm. Additionally, from these same two plots, the already mentioned drastic improvement of responsivity (by factors of 10 and 100 at 77K and 4K respectively) can be clearly seen.

Finally, we analyze the responsivity of all devices as a function of bias voltage (Fig. 2.25 and 2.26). The 'in-dewar' devices results at three temperatures, 300K, 77K, and 4.2K are shown at the top, middle and bottom of Figure 2.25 respectively. In all of these cases, but particularly for those at cryogenic temperatures (77K or lower) there is a sharp responsivity peak near the zero bias. This peak also rapidly diminishes to near the noise level of the measurement when a small bias is applied in any direction (i.e. positive or negative). However, as the voltage keeps being increased, a steady but small increase of the responsivity signal is observed (see logarithmic plots). This response at the high bias voltages does not reach the same level of the first sharp peak; however, its presence hints

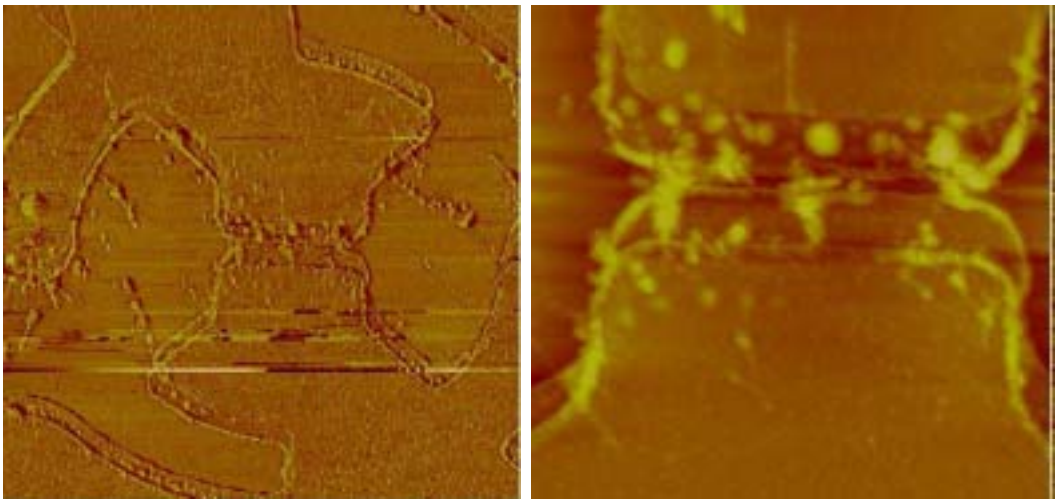

Figure 2.19 AFM image of device C5 from the LPA2 generation. Several CNTs and bundles bridge the gap and the smallest teeth of the antenna. Gap size is about 300nm.

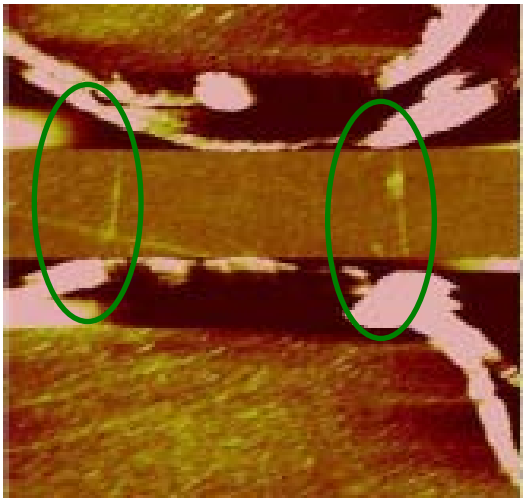

Figure 2.20 AFM images of device C2 from the LPA4 generation. Note two branches of CNTs (inside green circles) across the gap. Two layers of metal are also visible here.

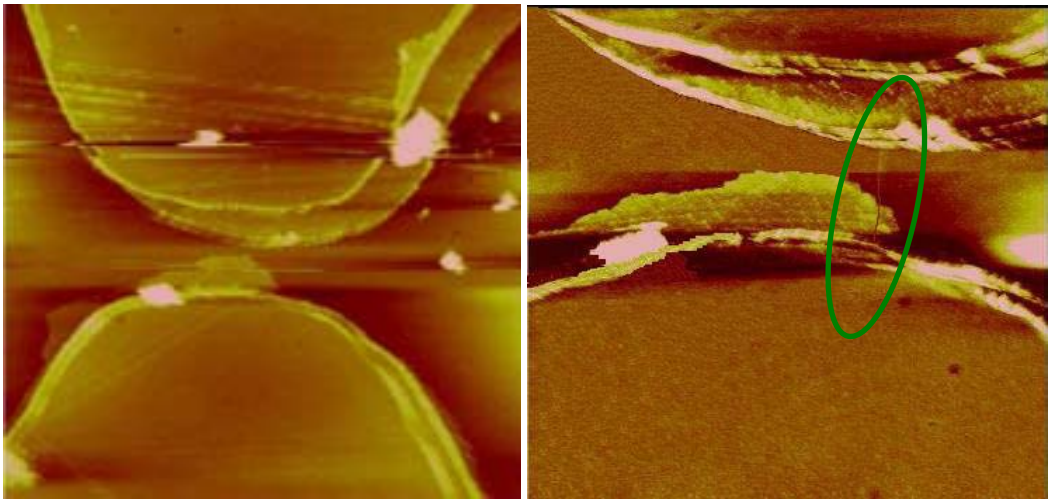

Figure 2.21 AFM images of device C3 from the LPA4 generation. Single CNT (inside green circle) has an effective length of about 1μm and measured diameter of around 1.5nm. Note the two overlapping layers of metal (Au and Pd) used in order to obtain all around contacts.

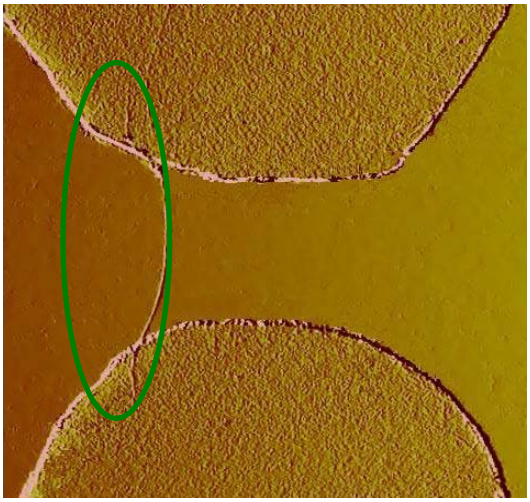

Figure 2.22 AFM image of device F2 from the LPA4 generation. This device was the first occasion when single CNT (inside green circle) deposition was achieved by using DEP in our lab. Only Au bottom layer was used. Effective CNT length of about 1μm and diameter of 1.52nm.

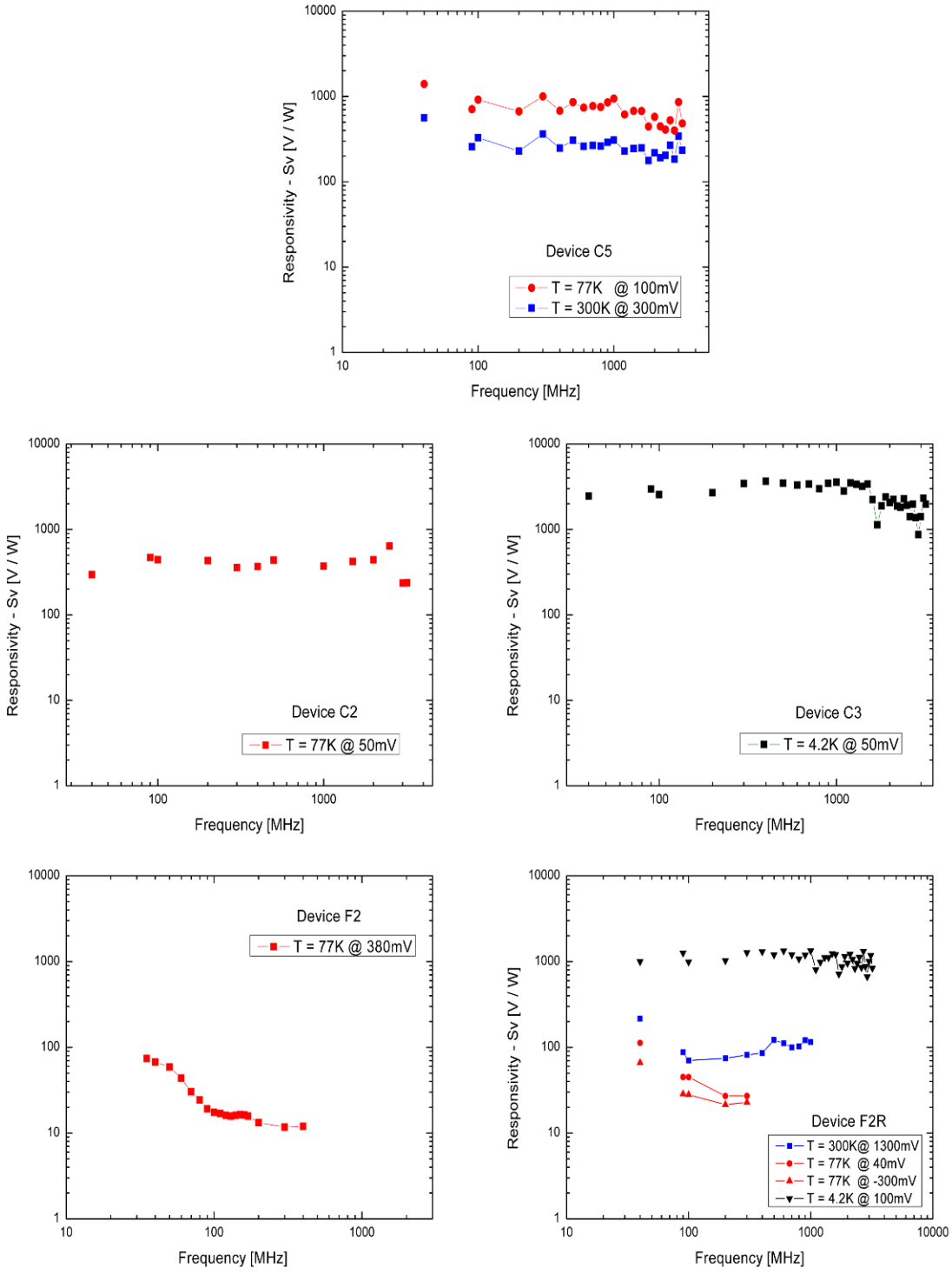

Figure 2.22 MW responsivity vs. frequency for LPA2 and LPA4 generation devices: C5 (top), C2 (middle left), C3 (middle right), F2 (bottom left), and F2R (bottom right).

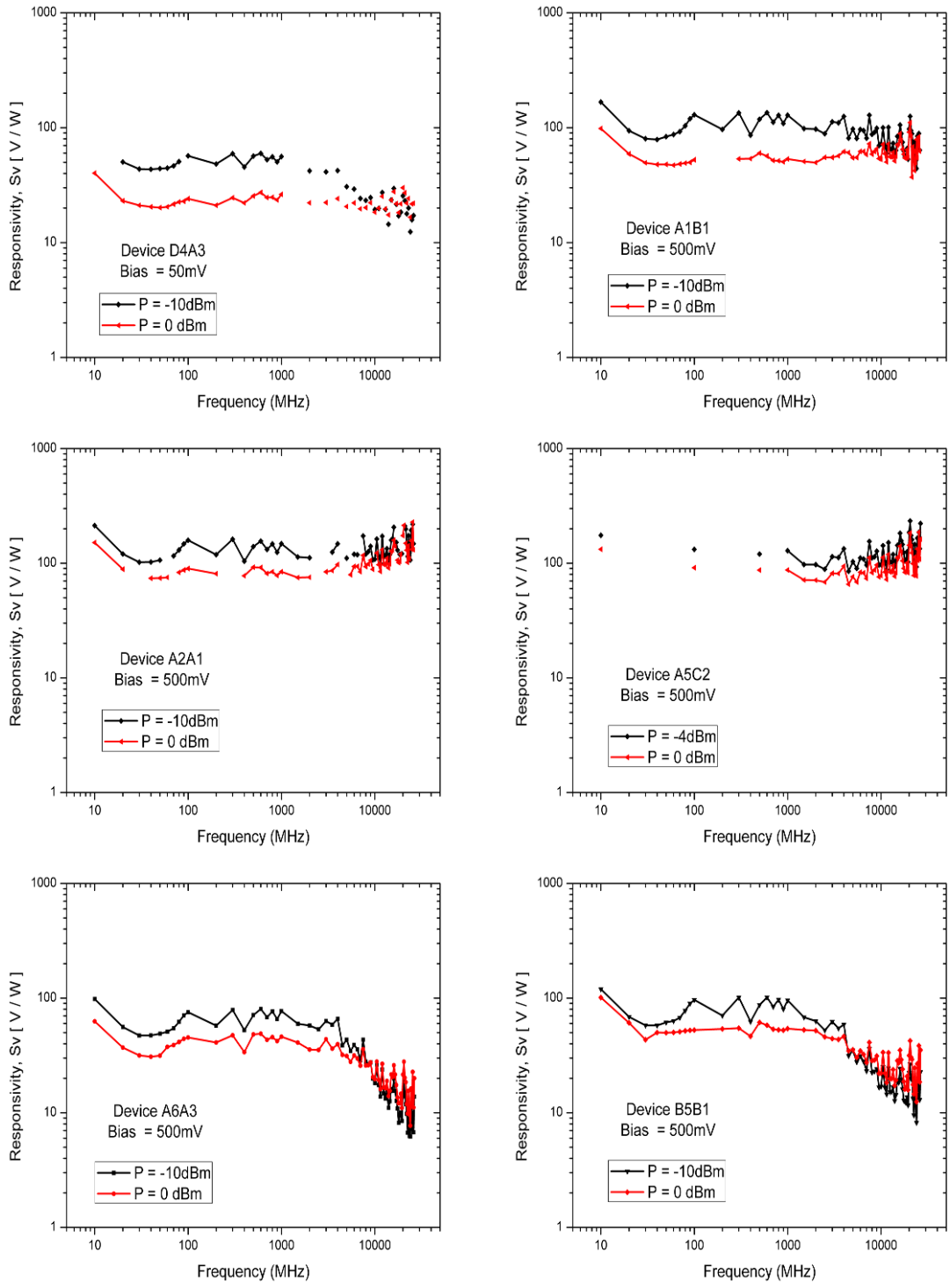

Figure 2.23 MW responsivity as a function of frequency for LPA1 Generation devices: D4A3, A1B1, A2A1, A5C2, A6A3, and B5B1. All measurements done at 300K.

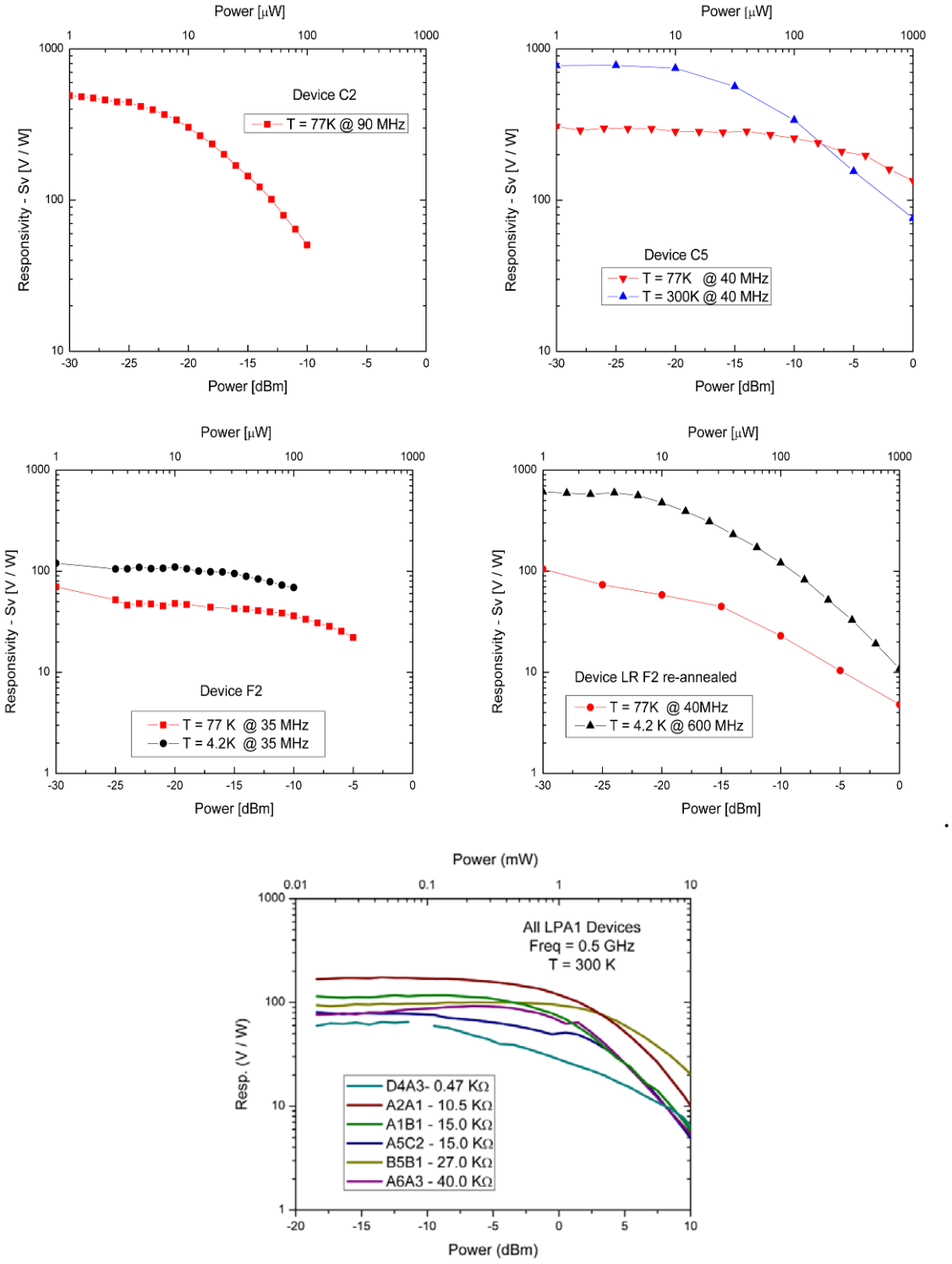

Figure 2.24 MW responsivity vs. increasing MW power for all devices tested at MW frequencies.

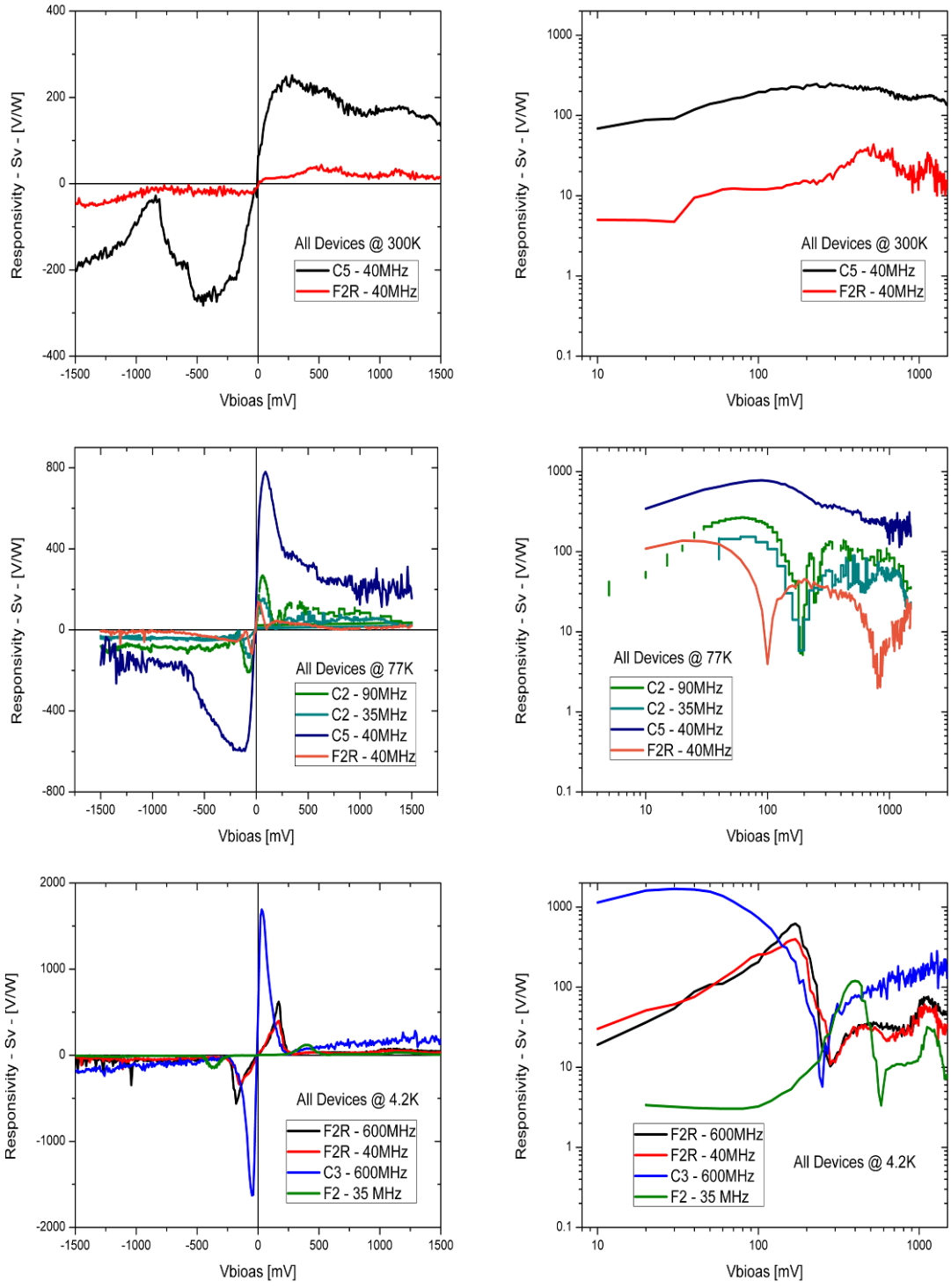

Figure 2.25 MW Sv vs. voltage at three temperatures: 300K (top), 77K (middle), and 4.2K (bottom). Plots shown in linear scale (left column) and logarithmic scale (right column)

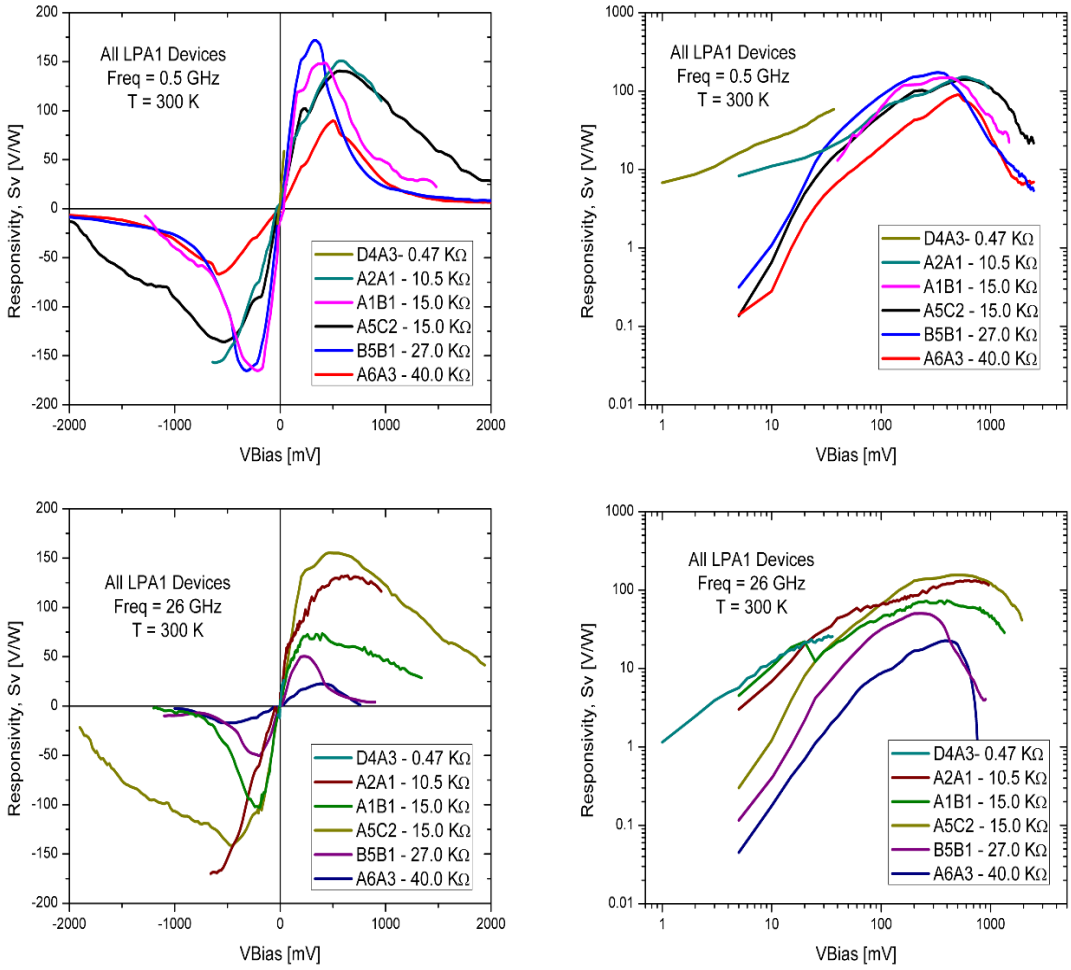

Figure 2.26 MW Sv vs. voltage at room temperature at two different frequencies: 0.5GHz (top) and 26 GHz (bottom). Note that plots are shown in linear scale (left column) and logarithmic scale (right column).

at the existence of at least more than one mechanism which gives rise to the MW detection. Furthermore, all of this bias dependent measurements were done applying a MW signal of -20dBm and frequencies that ranged from 40 to 600 MHz. Moving on to describe the probed devices responsivity as a function of voltage results (Fig. 2.26), it is

clear that sharp responsivity peaks are not present. In this cases, a steadier increasing responsivity signal is observed which after a certain voltage is reached, similar to that for the 'in-dewar' devices, decreases gradually. Furthermore, the bias dependencies shown in Figure 2.26 were measured by applying a MW signal of -10dBm at 0.5GHz (top) and 26GHz

(bottom). Finally, both slightly different bias dependent behaviors observed for the 'in-dewar' and probed devices are explained in more detail in Chapter 3.

2.2.3 S-Parameter Characterization

2.2.3.a S-Parameter Measurements and De-embedding Process

In the introductory chapter of this thesis, it was mentioned that nanotubes can be treated as transmission lines composed of a kinetic inductance (L_k), a quantum capacitance (C_Q), and an electrostatic capacitance (C_E) [28]. Also, it was mentioned that contact effects needed to be considered. Therefore, a contact resistance (R_C) and a capacitance (C_C) were added to the Burke TL model. This new model was named *Modified TL Burke Model* and was first introduced (Fig. 1.7) in section 1.2.2. Furthermore, the devices presented have been shown -through the DC characterization and MW responsivity results- to be deeply affected by the quality of the contacts. As such, S-parameter measurements were performed to find the parameters of the proposed circuit and therefore obtain a better understanding of the CNT-metal interfaces.

For this purpose, an Agilent vector network analyzer and microwave probes from Picoprobe® [58] were used. The probes were designed with the ground-signal-ground (GSG) configuration, operation range from DC up to 40GHz, and a 200 μm pitch. Their insertion loss was less than 1dB to 40GHz, and their return loss was greater than 20 to 26dB to 26GHz. Furthermore, in order to eliminate the effects from the cables and probes in our measurements, a SOL (short-open-load) one port calibration was performed using on substrate calibration standards. Figure 2.27 shows Smith charts of the un-calibrated setup, the SOL standards, and some typical devices of various resistances. Finally, the S-parameters of approximately one hundred and fifty devices, with a top layer of metal from the LPA1 generation, were measured. Figure 2.28 shows an example of the measurements obtained for a 1 KΩ device. The results for all devices measured will not be shown in this section; instead they will be presented as additional data in Appendix 2. This section simply includes the already discussed measurement setup, the de-embedding techniques used, and the results from our circuit simulations.

Next, in order to obtain an accurate description of the S-parameters of the CNTs themselves, the LPA1 structures were considered. For this purpose, devices with and without nanotubes were measured in an attempt to isolate the MW reflections due to the LPA1 structure from the ones due to the CNTs. Devices were arranged in 18 quadrants (Fig. 2.29), throughout the 3 inch high resistivity wafer, each containing 9 antennas. The middle antenna in each square was purposely left without CNTs, and as such it acted as the localized on-wafer open 'standard' used for de-embedding.

Furthermore, our devices could be treated as a capacitive reactive lumped element (LPA1) in parallel with the nanotubes (Fig. 2.30). As such, it was logical and convenient to use the Y-matrix representation for the de-embedding of the CNT data. From the circuit shown in Figure 2.29, it can be deduced that the Y-matrix of the CNTs can be obtained by simply subtracting the LPA Y-matrix from the measurement. Thus we have

$$[Y]_{CNT} = [Y]_{meas} - [Y]_{LPA} \tag{26}$$

where the LPA Y-matrix was obtained from the measured S-parameters of open devices (i.e. without any CNTs) and the 'measured' Y-matrix from the devices with CNTs. Y_{LPA} was very small and it varied slightly within different regions of the wafer; therefore, it was important that localized measurements of LPA devices with no CNTs were performed. This overall Y-matrix de-embedding technique has satisfactorily been previously used with similar CPW structures and CNT based devices [37].

Finally, we look at the measured and de-embedded Y-matrices obtained (Fig. 2.31) for a sample device. Note that the Y11 (or in Fig. 2.28, the S11) data for the devices with and without SWCNTs clearly are very distinct, and that calibration noise effects are quite small compared with this difference. Both of these factors reinforced the accuracy of the de-embedding process. For all analyzed devices, the magnitude of the admittance and impedance were calculated, as well as the phase of the latter. These extracted data (shown in Appendix 2) was then compared with simulated values obtained from the circuit model previously introduced.

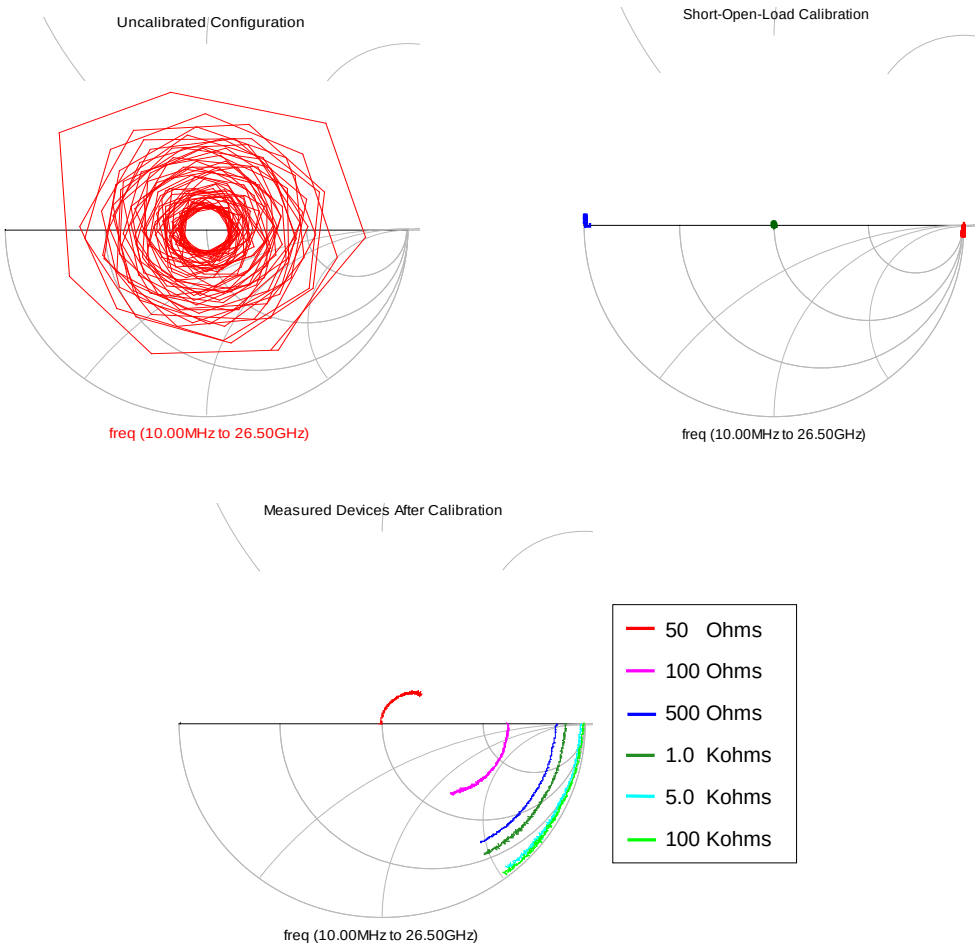

Figure 2.27 Smith charts showing the un-calibrated measurement setup at the end of the probes (top left), the measured SOL calibration standards (top right), and the measured S11 - after calibration- of several devices with different DC resistances (bottom).

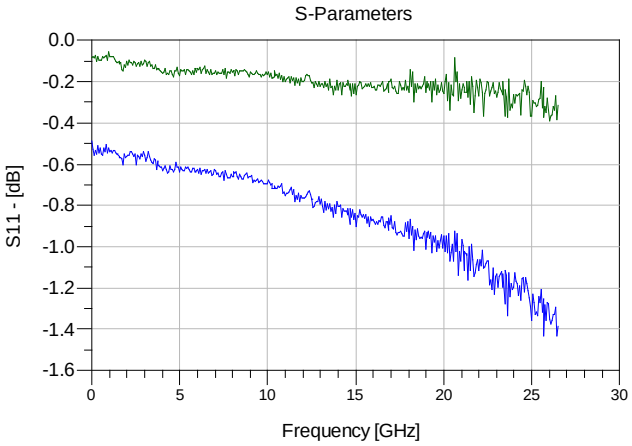

Figure 2.28 Measured S-11 for a device with CNTs (blue) and without CNTs (green).

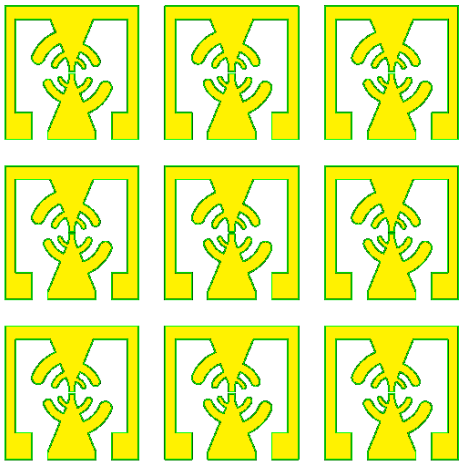

Figure 2.29 Example of a quadrant of LPA1 devices on the wafer. Note that middle device was left without CNTs to serve as localized open standard for de-embedding of CNT data.

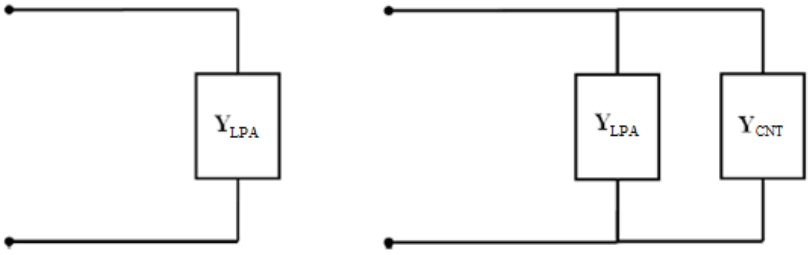

Figure 2.30 Circuit model of lumped elements for an LPA1 without CNTs (left) and with CNTs (right). From ref. [37].

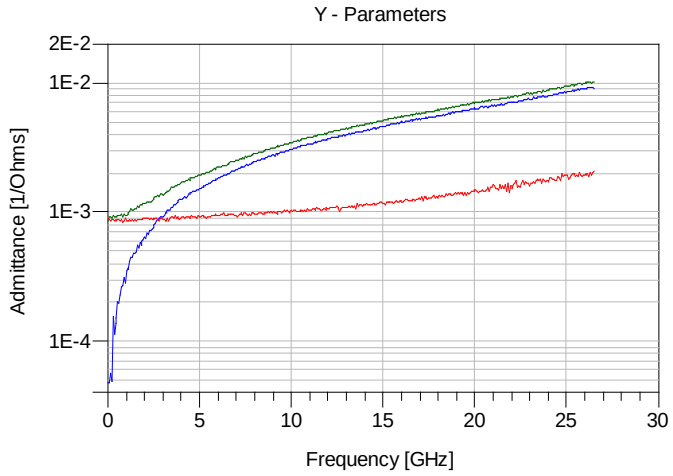

Figure 2.31 Magnitude of Y-parameters for a measured device with CNTs (blue), and without CNTs (green). Also, de-embedded admittance data for CNTs by themselves (red).

2.2.3.b Circuit Model Simulations

The *Modified TL Burke Model* (Fig. 1.7) was once more adjusted for the more experimentally realistic situations of our measurements. Effects of a small quantum capacitance (C_Q) and an even smaller electrostatic capacitance (C_E) will be too small to properly identify. Therefore, these two parameters were removed from the circuit model. The circuit model used in the simulations is shown in Figure 2.32. It basically consists of a kinetic inductance in series with the CNT resistance and contact resistances and capacitances added at each end.

Based on each device's IV characteristics, CNT configuration, and MW response the impedance data for 23 devices were fitted to the circuit model shown below. By simulating the model in ADS and varying the circuit parameters, a best fit with the experimentally data was obtained. An example of a typical fit is shown in Figure 2.33; the complete set of such fits is given in Appendix 2. In general, good fits to the model are found up to frequencies of about 10-15 GHz. Above these frequencies, there exists a discrepancy between the model and the measured data, well outside the calibration noise. This issue has previously been observed in similar measurements [59] and it was attributed to inhomogeneous scattering between tubes within bundles and at CNT-CNT contact points. The best fit parameters obtained are summarized in Tables 2.4 through 2.9. The devices are presented in two groups:

One in order of their total resistance, and a separate group with the devices for which MW responsivity measurements were also performed. For each group, the total resistance found from the de-embedded S11 measurements was compared with that measured at DC. Overall general agreement was found, demonstrating that the model fits are consistent at DC, and by implication also at low MW frequencies. Note also that, in order to provide further details about the devices characteristics, Tables 2.4 - 2.9 use a similar legend to the one in shown for Tables 2.2 and 2.3. This legend is shown for reference once again below Figure 2.32. Finally, the values obtained for the circuit parameters (i.e. R_C, C_C, R_{CNT}, and L_K) will also be discussed further in Chapter 3.

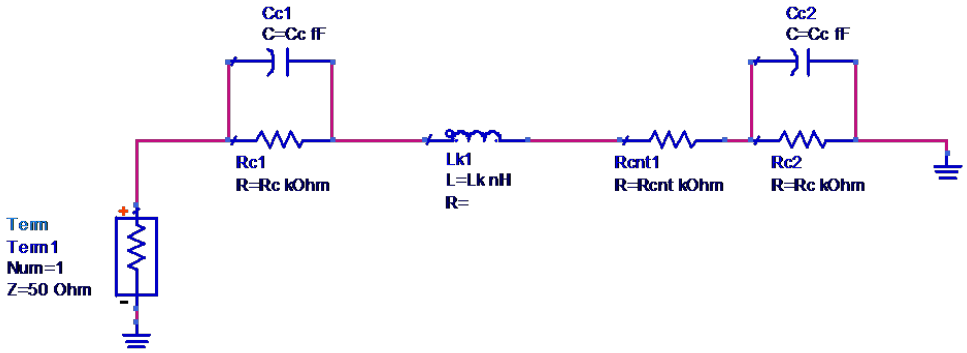

Figure 2.32 Circuit model used simulation of CNTs behaving as TL's.

Legend:	**Bold Text**	- *Ohmic* Device
	Non-Bold Text	- *Nonlinear* Device
	Blue Text	- Top layer of Pd added
	Black Text	- Bottom Au layer only

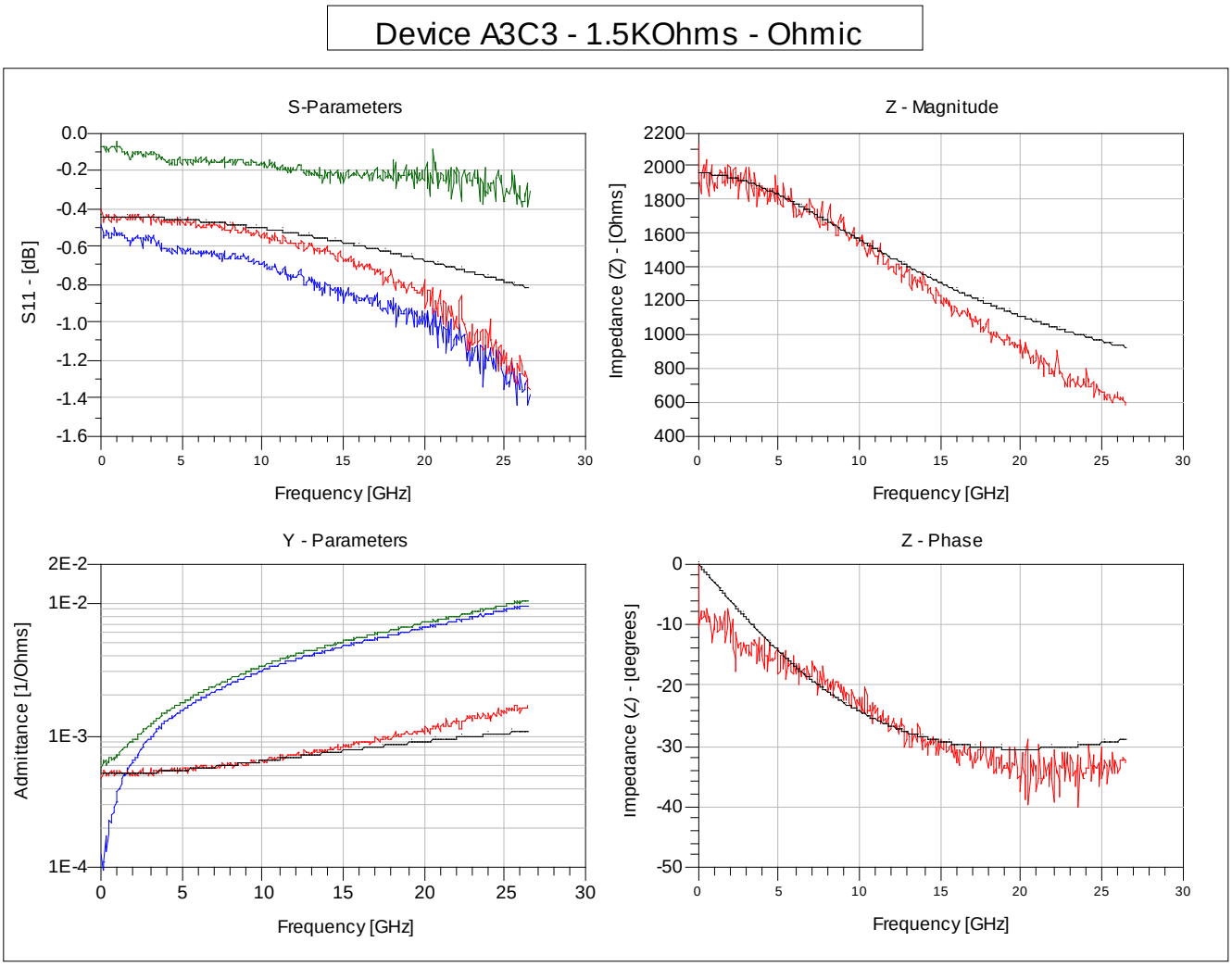

Figure 2.33 Example of how simulated data -obtained from circuit shown in Fig. 2.32- was fit to the de-embedded results. There are four plots shown in each fit: S-parameters (top left), admittance magnitude (bottom left), impedance magnitude (top right) and phase (bottom right). The de-embedded data is shown in red for all plots, while the measured data for devices with CNTs and without are shown in blue and green respectively for the S parameter and admittance plots. Finally, the simulated data are shown in black lines with circles. Note the clear and well defined difference between the measured devices with and without CNTs.

Devices	Rcnt [Ω]	Rc [Ω]	Rc1 [Ω]	Cc [fF]	Cc1 [fF]	Lk [nH]
D3A2	22.1	10.8	16.9	215	170	0.33
D3A3	21.2	10.9	16.6	210	35.0	0.28
D3A1	36.1	18.7	42.45	204	114	0.47
D3C2	65.0	35.3	24.5	180	198	0.56
D3B3	74.1	35.1	50.1	162	96	0.74
D3B1	86.1	73.0	59.0	51.0	93.0	0.62
	170	12.39	34.07	292	316	0.37
D3C3	121	50	50	151	105	0.52
D4A3	159	120	191	31	22	1.25
B7C1	240	70.1	430	17	17	0.81
D2C1	358	270	200	23	83	0.50
D2C2	430	410	170	23	74	0.19

Table 2.4 Circuit parameters obtained from fitting of simulated to measured S-parameters for devices of resistances ranging from 50 to around 800 Ω.

Devices	DC Impedance [Ω]			Good Fit up to: [GHz]
	Measured	Simulated	% Diff.	
D3A2	50	49.8	0.4	15
D3A3	50	48.7	2.6	15
D3A1	90	97.3	7.7	15
D3C2	110	125	12.6	15
D3B3	150	159	6.0	10
D3B1	200	218	8.7	15
	200	216	7.9	15
D3C3	200	221	10.0	15
D4A3	470	470	0	15
B7C1	660	740	11.5	15
D2C1	700	828	16.8	15
D2C2	825	1010	20.2	15

Table 2.5 Comparison of measured vs. calculated DC impedance. The "Measured' column refers to values obtained from IV curves, while the 'Simulated' column simply adds the values of Rc1, Rc2, and Rcnt from table 2.4.

Devices	Rcnt [KΩ]	Rc [KΩ]	Rc1 [KΩ]	Cc [fF]	Cc1 [fF]	Lk [nH]
B2B1	0.373	0.254	0.435	45	13.0	1.1
B2C3	0.55	0.361	0.248	44	30	0.907
C6C2	0.401	0.867	0.14	11.9	30.7	0.12
B7A3	0.85	0.262	0.37	50	20.0	0.16
A3C3	0.54	0.85	0.56	23	14	0.65
B7C3	0.84	0.433	0.64	37	12	0.141

Table 2.6 Circuit parameters obtained from fitting magnitude and phase of simulated and measured (obtained from S-parameters) impedance. Devices of resistances close to 1 KΩ.

Devices	DC Impedance [KΩ]			Good Fit up to: [GHz]
	Measured	Simulated	% Diff.	
B2B1	0.90	1.062	16.5	20
B2C3	1.00	1.159	14.7	15
C6C2	1.20	1.408	16.0	15
B7A3	1.30	1.482	13.1	15
A3C3	1.50	1.95	26.1	15
B7C3	1.65	1.913	14.8	15

Table 2.7 Comparison of measured vs. calculated DC impedance. The "Measured' column refers to values obtained from IV curves, while the 'Simulated' column simply adds the values of Rc1, Rc2, and Rcnt from table 2.6.

Devices	Rcnt [KΩ]	Rc [KΩ]	Rc1 [KΩ]	Cc [fF]	Cc1 [fF]	Lk [nH]
D4A3	0.159	0.12	0.191	31	22	1.25
A2A1	8.1	2.674	2.08	4	8	35
A1B1	5.2	7.463	4.08	2.4	2.7	74
A5C2	0.4	6.67	4.8	6	4.4	2
B5B1	7	15.09	11.09	1.7	0.8	56

Table 2.8 Circuit parameters obtained from fitting of simulated to measured magnitude and phase of the impedance for devices which were also measured for MW responsivity. Resistances range from 0.47 to 27KΩ.

Devices	DC Impedance [KΩ]			Good Fit up to: [GHz]
	Measured	Simulated	% Diff.	
D4A3	0.47	0.47	0.0	16
A2A1	10.5	12.854	20.2	15
A1B1	15.0	16.743	11.0	15
A5C2	15.0	11.87	23.3	15
B5B1	27.0	33.18	20.5	15

Table 2.9 Comparison of measured vs. calculated DC impedance. The "Measured' column refers to values obtained from IV curves, while the 'Simulated' column simply adds the values of Rc1, Rc2, and Rcnt from table 2.8.

2.2.4 Terahertz Direct Detection

2.2.4.a Experimental Setup

The principle behind the experimental setup used for THz detection experiments was similar to the one employed for the MW measurements. Basically devices received some THz power at certain frequencies, and the difference in voltage when the THz signal was modulated from ON to OFF was measured. However, this measurement was more complex due to the difficulties and limitations when dealing with THz signals. The THz source used was a CO_2 pumped far infra-red (FIR) gas laser (Fig. 2.34). Our group has vast experience dealing with this particular source (named SIMON), and other THz lasers. This particular laser, is capable of emitting up to 20mW of THz power for some of the strongest and most stable transitions levels of the CO_2 laser.

Furthermore, coupling the THz radiation to the CNT based device also required more planning than for the MW experiments. Quasi-optical techniques were used in order to deliver the THz power to the CNTs. A high resistivity silicon focusing elliptical lens was glued with bees was to the back side of 5 x 5 mm device chip (Fig. 2.35). The matching of dielectric constants between the lens and the substrate, the appropriate thickness of the latter, and the THz transparency of the bees wax, were critical factors for this scheme to work. In order for the THz to strike the antenna at the focal point of the lens, the substrate needed to be 350 μm thick. Our group has done extensive studies on this technique and has found that a

loss of about 3 dB is to be expected when THz are coupled in this manner [42]; nonetheless, our source was powerful enough that a 3dB loss would still allow more than enough power to go through. The THz radiation that did manage to go through the lens would be picked up by the teeth of the LPA, which would convert it into THz currents. These currents would then travel along the edges of the metal, according to other groups' HFSS calculations, and go into our CNTs placed as loads in the middle of the gap. This technique was strongly reliant on a nicely focused Gaussian THz incoming beam that hit the lens. In order to do so, a variety of off-axis parabolic (OAP) focusing elements (Fig. 2.36) were used. This THz beam was then carefully aimed at the window of the dewar, behind which the CNT based device with the lens, had been carefully placed. At this point, we encountered again another optical loss (1dB) due to the Zitex window. In general, since the THz power that reached the antenna was reduced by at least a factor of two, optical losses (~ 4dB) needed to be accounted for when calculating the intrinsic detected responsivity of the devices.

Finally, once all the optics and quasi-optical schemes had been properly configured, the setup (shown in Fig. 2.37) to measure THz direct detection was very analogous to the one previously employed at MW. The same lock-in amplifier technique was used to measure the difference in voltage across the 100KΩ resistor in series with the CNT device, and the THz source was also modulated ON and OFF at 1 KHz. This modulation of the FIR beam was achieved by using an acoustical-optical modulator (AOM). Similarly, just as for the MW responsivity experiment, the modulation signal also served as the reference for the lock-in amplifier, thus only measuring voltage differences in phase with the THz power.

Fig. 2.34 CO_2 pumped FIR gas laser used as THz source.

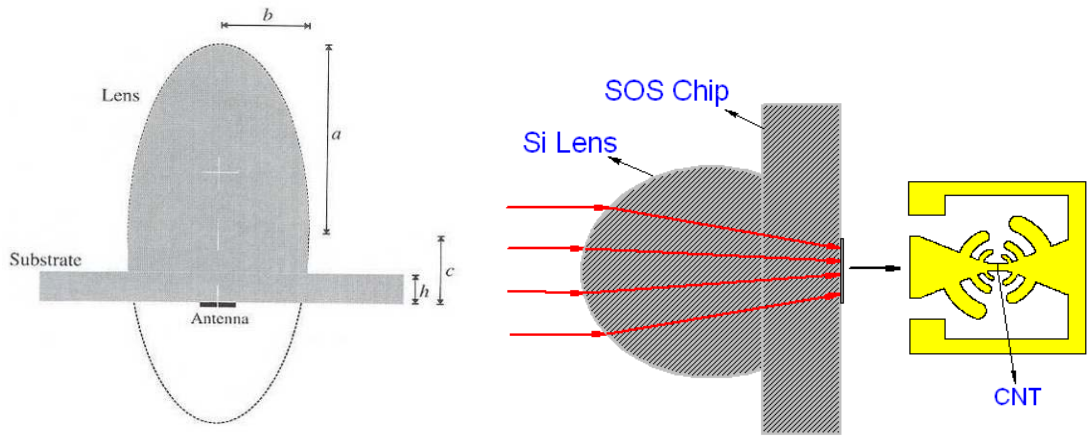

Figure 2.35 Elliptical lens design (left) and THz beam path through the elliptical lens with respect to LPA chip (right).

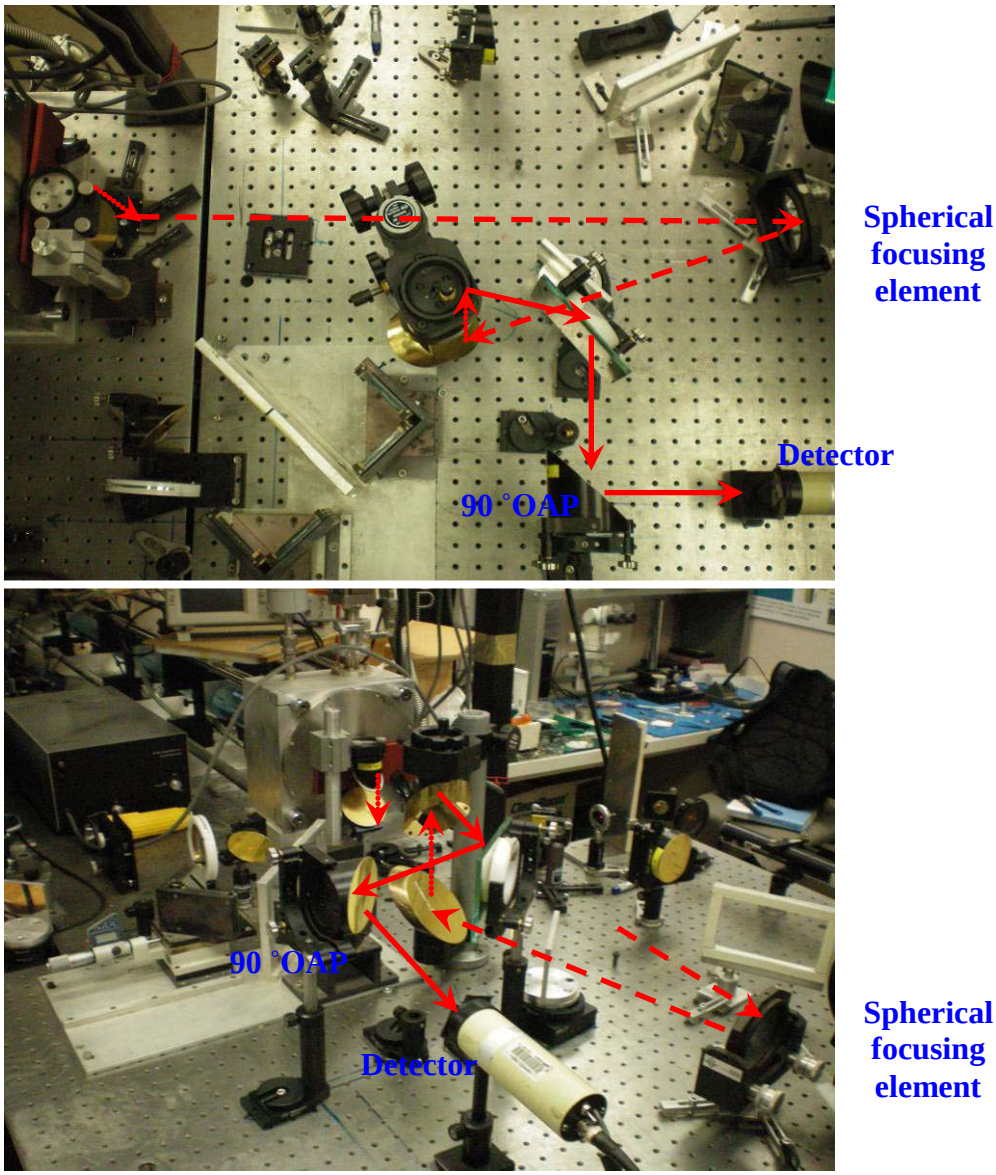

Figure 2.36 THz beam path used for THz detector measurements. The straight and sliced arrows represent the beam path at two different heights, 240 and 100mm respectively. The dotted lines represent a change in height.

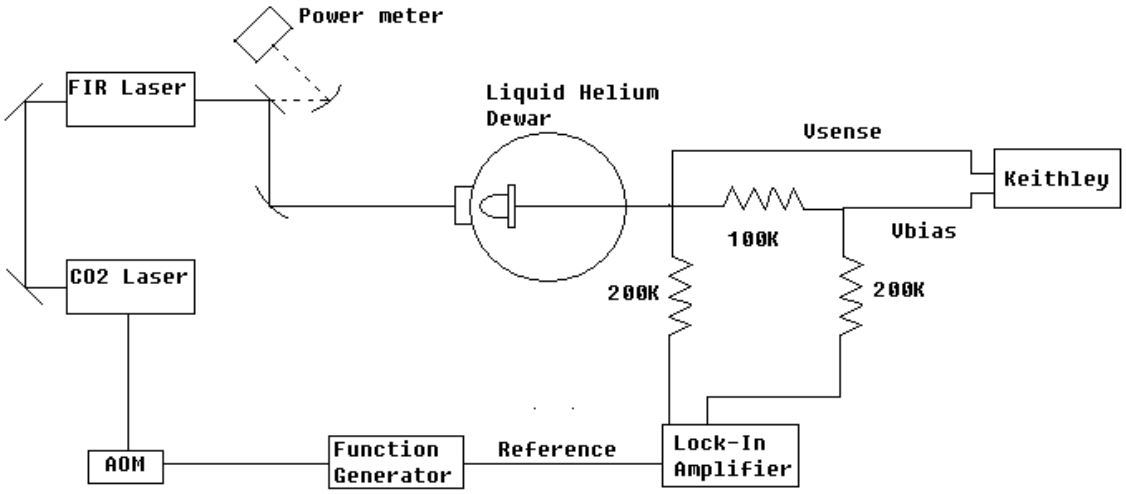

Figure 2.37 Schematic of experimental setup used for THz detection experiments.

2.2.4.b Responsivity Results

Using the experimental setup described above several LPA2 and LPA3 devices were tested for THz responsivity. The response was calculated using expression (12), where the voltage difference -caused by the change in resistance of the CNT device when heated by THz- across the 100KΩ resistor was divided by the applied THz power. Measurements were primarily taken at 77K and 4.2K for a variety of frequencies ranging from 0.694 to 2.56 THz. Before presenting and describing the results from the THz detection experiments, some of the devices are introduced through SEM pictures (Fig. 2.38 - 2.40). It is clear that all of these devices were composed of several bundles of CNTs, and in some cases, even complicated networks. These types of CNT configurations made it difficult to isolate individual CNT effects, and also challenging to understand and predict their ideal performance. Lastly, all of these devices showed the previously described *nonlinear* contact behavior, and as such heavily are reliant on contact effects. Refer to Tables 2.2 and 2.3, as well as to Appendix 2 for the more detailed description of the IV characteristics of these devices.

First, the device THz response as a function of bias voltage is presented (Fig. 41 - 45). In all of these figures, plots of measured responsivity (black dots) versus bias voltage as well as theoretical fits (i.e. diode or bolometer model) are shown. In some

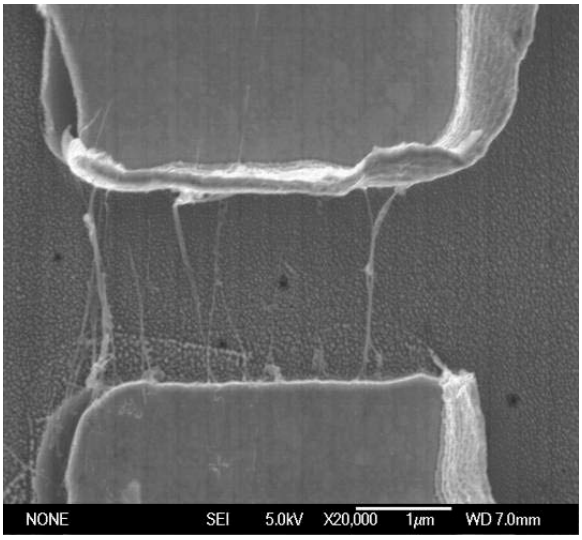

Figure 2.38 SEM image of devices 3C3. Several nanotube bundles in parallel bridge the 1μm gap of the antenna. It will remain unclear which one, if any of these dominates in the electrical transport and THz detection process.

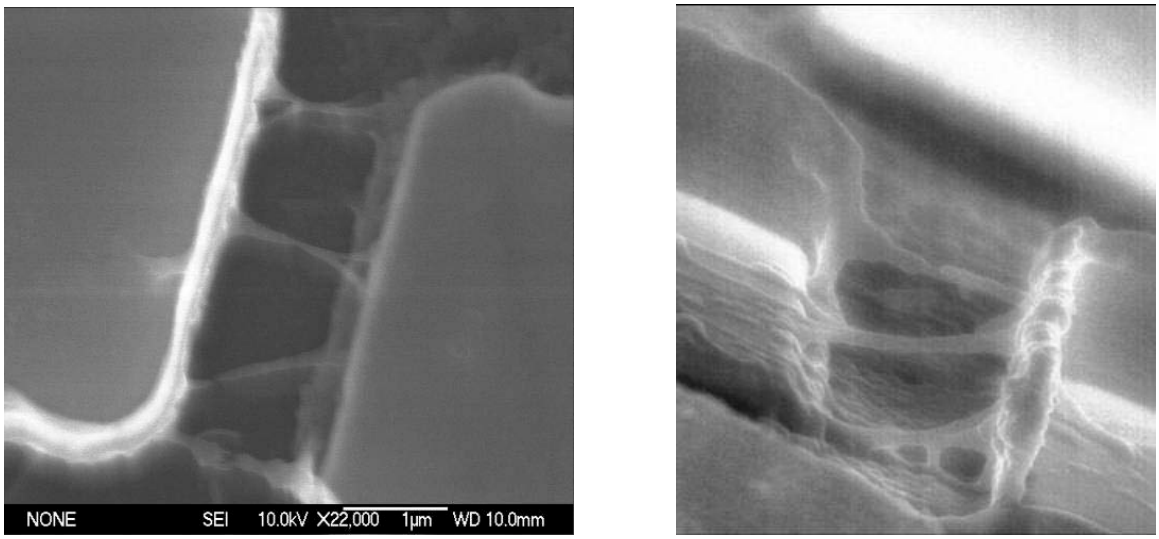

Figure 2.39 SEM images for device 4A2 from a top (left) and side (right) view. From both figures one can see that several thick CNT bundles bridge the gap of this device. Also, CNTs are limited to the gap only, with small overlap between CNT and metal. Finally, in the image at the right, note suspension of bundles over SiO2 trench.

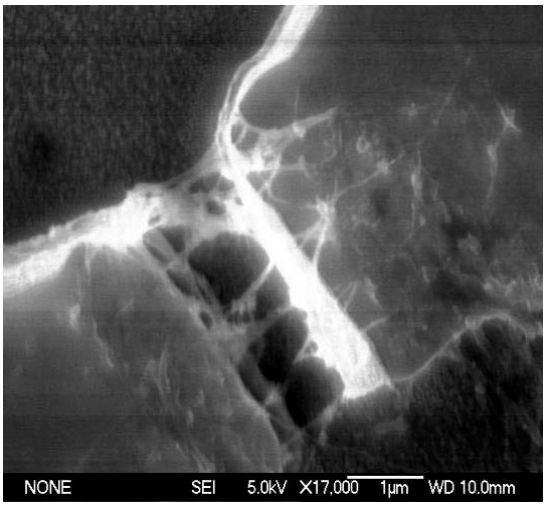

Figure 2.40 SEM images for devices 4A3. Complicated network of CNT bundles with big overlap with metal bridges the 1μm gap.

cases one of these theoretical models was a clearer fit to the measured data, while in some other the situation was reversed. Details on the nature behind these models and their parameters, as well as their physical implication for particular devices will be discussed in Chapter 3. In this section, results for THz direct detections are merely presented and briefly described.

The responsivity of device C4 at 77K (top plot of Fig. 2.41), showed a gradual increase which peaked at around 3 V/W at 300mV. This response was kept fairly constant even as the bias was increased to 1.5V. For the same device, at a temperature of 4.2 K (also in Fig. 2.41), the THz responsivity plots clearly changed patterns. The frequencies tested were 0.76, 1.05, 1.40, and 1.63 THz. For all frequencies, a sharp responsivity peak near the zero voltage is evident. Furthermore, this response rapidly decreased as the bias was increased. Peak THz detection of almost 60 V/W (after accounting for optical losses) was measured at 0.76THz; however, this response also rapidly decreased for higher frequencies. Additionally, we note that even with the change in responsivity pattern at 4.2K, the bolometer model was the one found to be a good fit to all the experimental data.

Similarly, device 4A3 was tested as a function of applied bias and frequency. In Figure 2.42 five plots for THz responsivity are shown for frequencies ranging from 0.694 to 1.63THz. Also, the same two temperatures (77K and 4.2K) were explored. Overall, when compared to C4, device 4A3 had similar values of response at 77K -ranging from almost 3 to 0.1 V/W); however, the response did not increase drastically when the device was cooled to 4.2K. THz responsivity at this lower temperature and at 0.694THz was around 0.1V/W. Once again we note that the model to which the experimental data seems to fit better is the bolometer model (based on dR/dT); furthermore, in two of the plots the diode model fit (based on d^2I/dV^2) was also calculated at 77K and 4.2K, and very little resemblance with experimental data was found. Next, Figure 2.43 shows the THz responsivity of several other devices, all measured at 77K. The responsivity of these was similar to the ones already described; therefore, we will not describe them in further detail. It suffices to mention that the responsivity of these devices was lower in most cases, than that of the C4 and 4A3.

Continuing to describe the results from the several THz detection experiments performed, we move on to device 4A2 (Fig. 2.44). This device (shown in Fig. 2.39) had clear CNT bundles suspended across the gap of the LPA, and thus was expected to behave differently. Primarily, a higher responsivity was anticipated since in principle, the suspension should have reduced the overall thermal conductance. Unfortunately, as is evident from the plots in Figure 2.44, the response did not drastically increase; actually, it remained within the similar 1 to 4 V/W range like in the other devices. Nonetheless, a different mode of operation was found for the first time at THz frequencies: The diode model. In four of five instances the diode model was found to be the better fit to the measured experimental data. The last case, in which the device behaves as a bolometer, was due to the break of one of the main branches of CNTs. Therefore, the resistance of the device and the contact effects of the device changed. It was not expected to find agreement with the diode model after this break of CNTs. Similarly, the THz response of device 3C3 (Fig. 2.45) was best described by the diode model also. Note that the overall responsivity for this last device (3C3), was smaller than the one for 4A2.

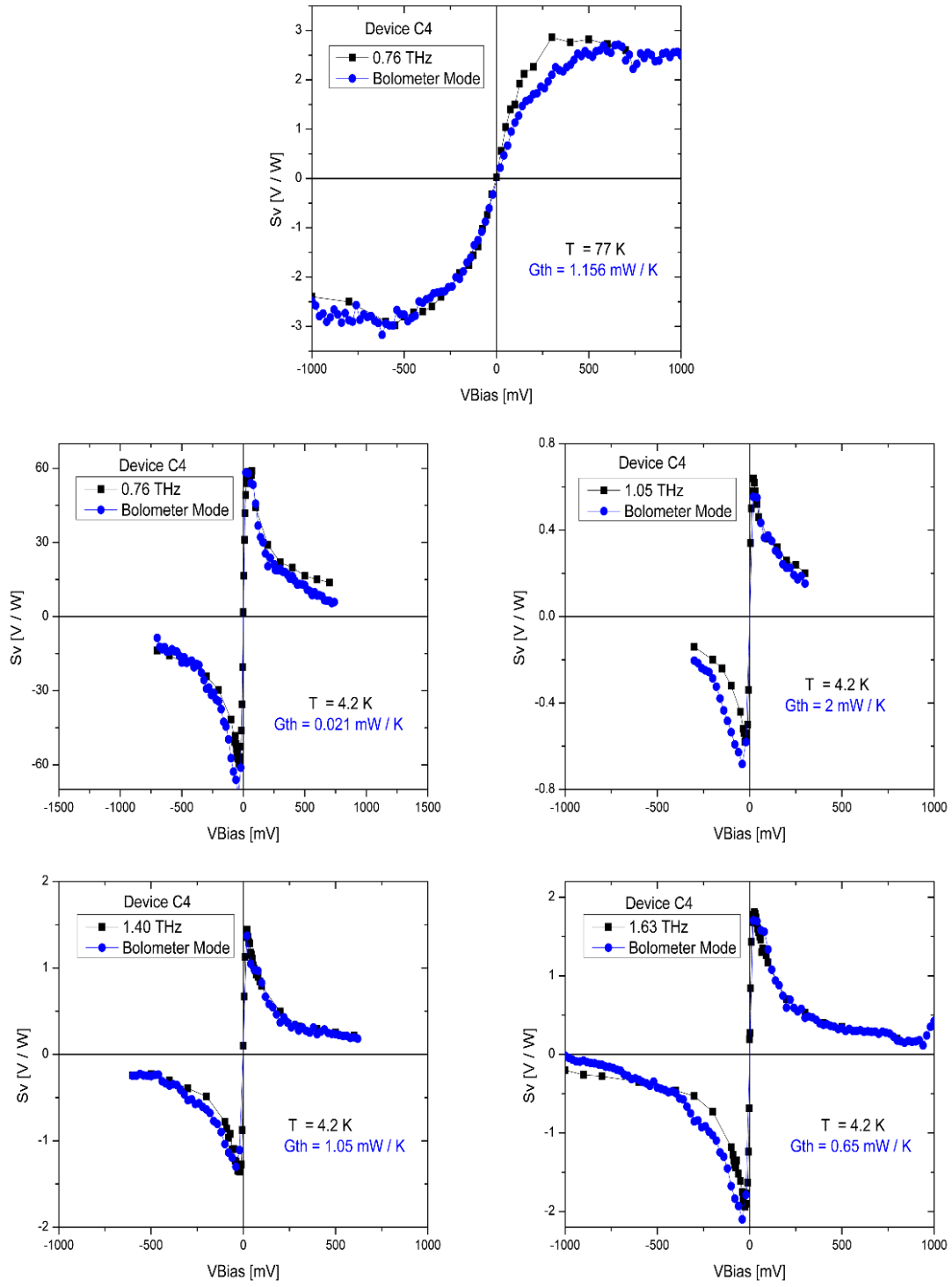

Figure 2.41 THz detection for device C4 (LPA2). Response as a function of bias showed for frequencies ranging from 0.76 THz to 1.63 THz and temperatures of 77K and 4.2K.

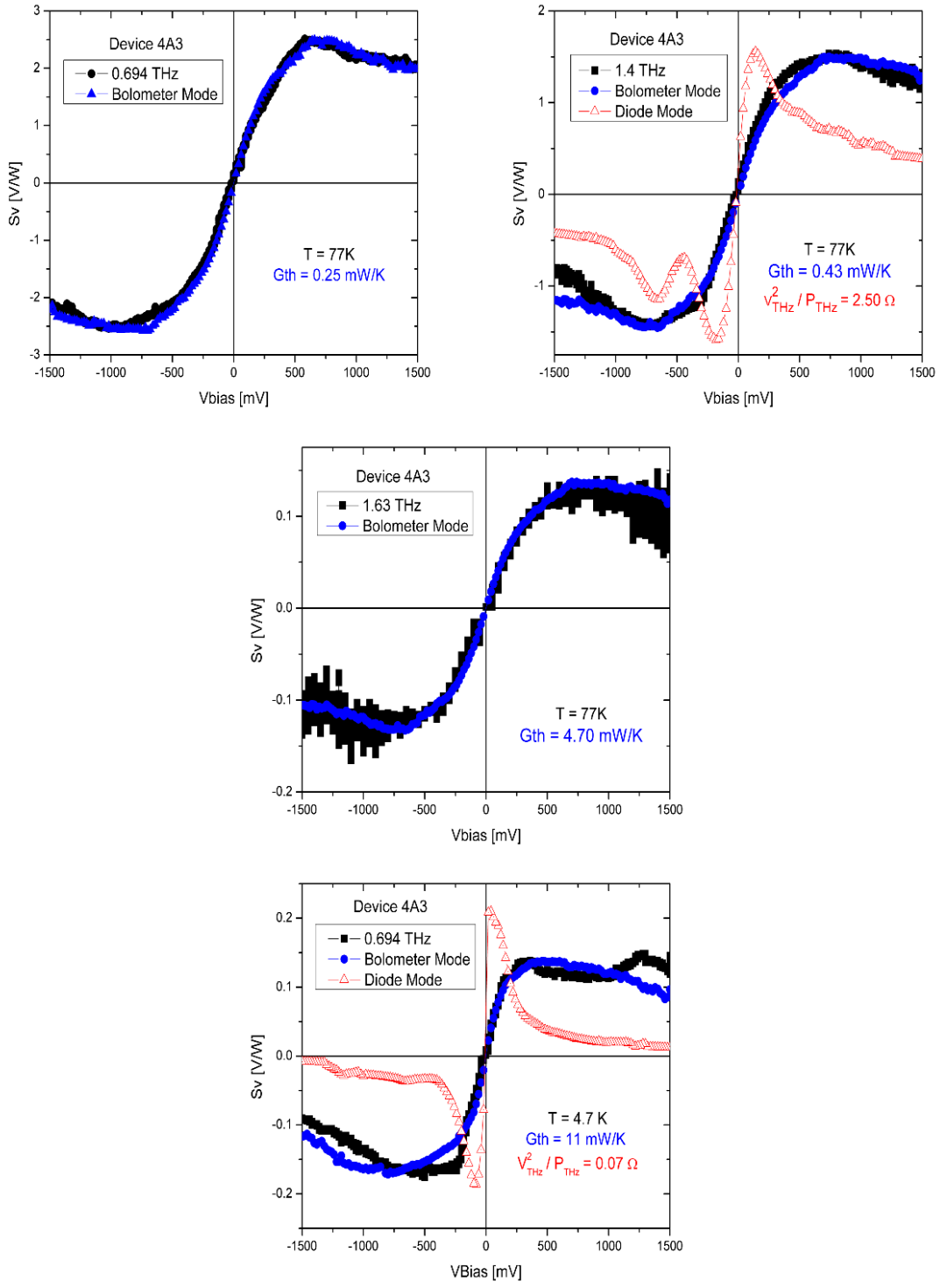

Figure 2.42 THz detection for device 4A3 (LPA3). Response as a function of bias showed for frequencies ranging from 0.694 THz to 1.63 THz and temperatures of 77K and 4.2K.

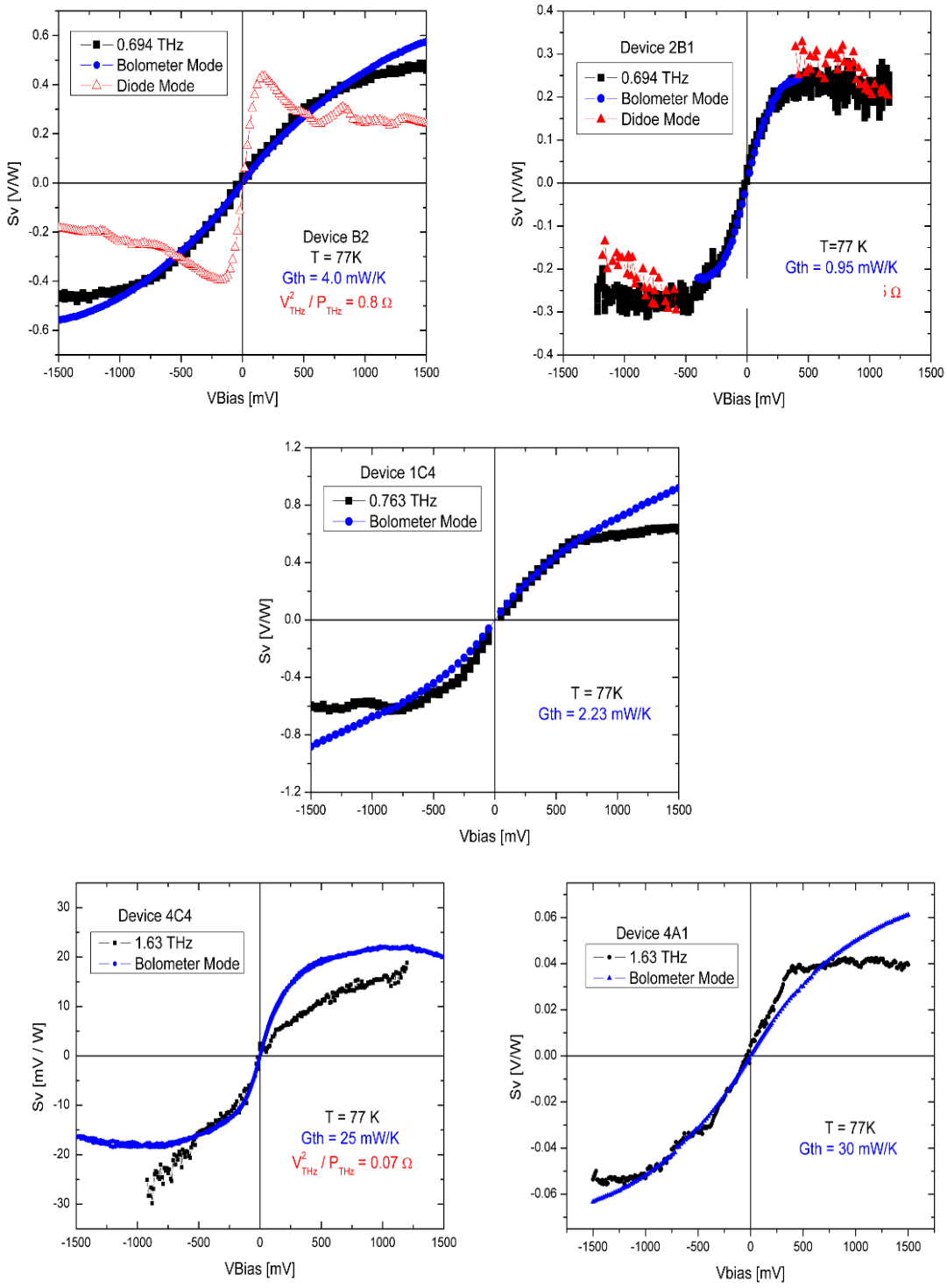

Figure 2.43 THz detection for various devices from the LPA3 generation. Response as a function of bias shown for frequencies ranging from 0.694 THz to 1.63 THz all at 77K.

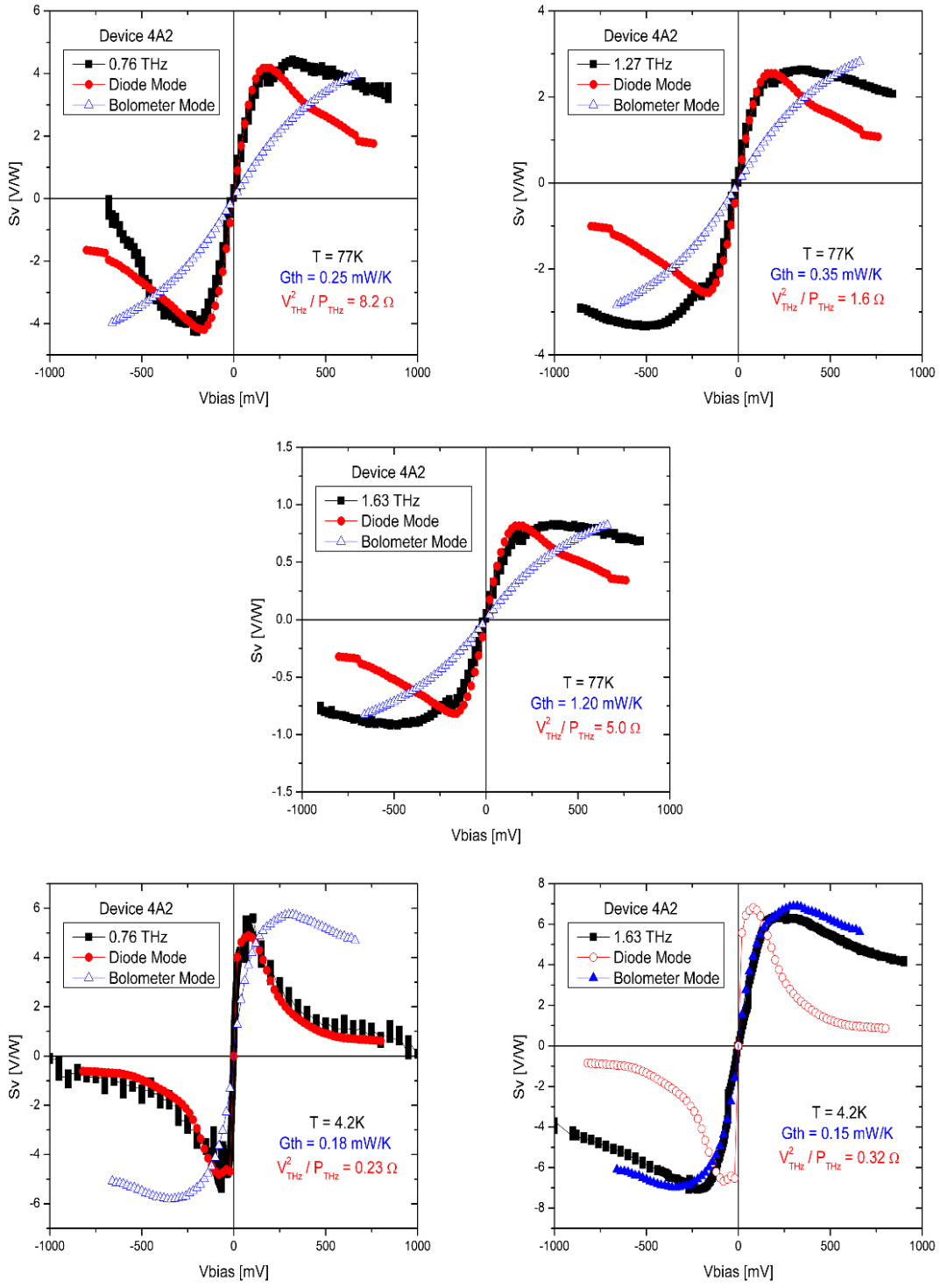

Figure 2.44 THz detection for device 4A2 (LPA3). Response as a function of bias shown for frequencies ranging from 0.760 THz to 1.63 THz and temperatures of 77K and 4.2K.

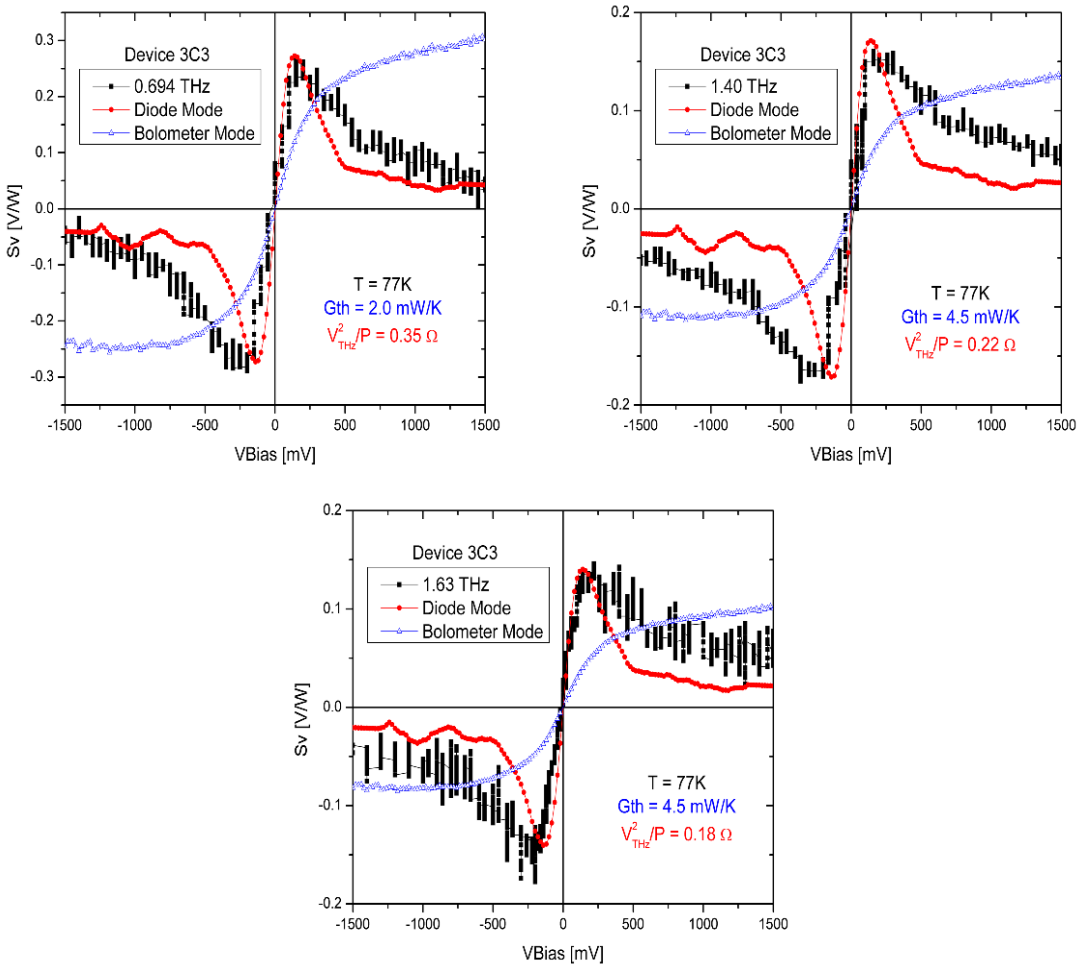

Figure 2.45 THz detection for device 3C3 (LPA3). Response at 77K showed as a function of bias for three frequencies: 0.694, 1.40, and 1.63 THz.

Finally, we present a summary of the peak values for THz direct responsivity, of some of the main devices, as a function of both frequency (Fig. 2.46) and temperature (Fig. 2.47). From the first graph, it is difficult to extract a definite relation on how the THz response varies as the frequencies were increased up to 2.56 THz. However, there is an overall tendency for the response to decrease when the frequency is increased. The absence of any sort of resonance (expected from our "modified Burke model") on the response, cannot be clearly explained. Nonetheless, it is important to note that in order to observe any resonant behavior, contact effects cannot constitute a major part of the detection process.

On the other hand, from the second graph (Fig. 2.47) the THz response dependence on temperature is clear. The overall diminishing responsivity as the temperature is increased is consistent for all devices. However, as evident by the many decreasing responsivity curves, the rate at which the response disappearance occurs is different from device to device. Several parameters (mainly CNT resistance, contact resistance, and thermal conductance) change as the temperature increases, and as such, it is difficult to point to the exact reason of the smaller response. Further temperature dependent measurements of the THz response need to be done in simpler devices (i.e. single well contacted CNT device) in order to attempt to understand the underlying physics behind this signal degradation. More discussion of both the frequency and temperature dependencies, and the physical processes involved will be presented in Chapter 3.

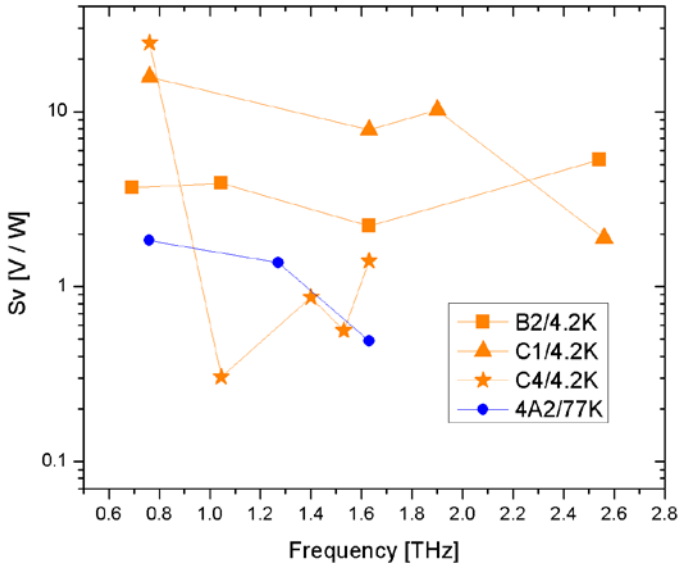

Figure 2.46 Summary of direct THz responsivity vs. frequency for several devices at 4.2K (orange) and 77K (blue).

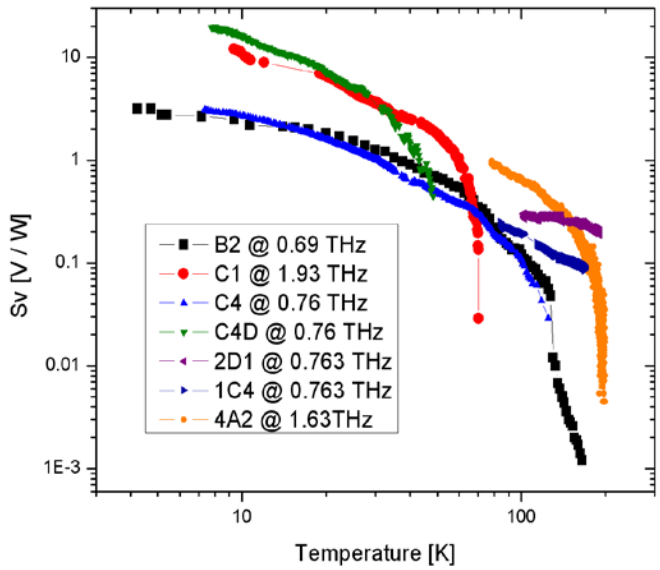

Figure 2.47 Summary of direct THz responsivity vs. temperature for several devices at several THz frequencies.

CHAPTER 3
UNDERSTANDING THE DETECTION PROCESSES

In Chapter 1, we thoroughly introduced the diode and bolometer mode detector framework. Additionally, all the results for the DC, MW, and THz characterization for some of the best devices that have been fabricated by our group over the past two years, have been presented in Chapter 2. Even more, the DC temperature dependent characterization, the S-parameter measurements, and several SEM/AFM images provided us with extra tools in order to analyze the device direct responsivity to both MW and THz signals. With this theoretical and experimental apparatus in mind we will attempt to understand and explain the behavior of each device as a diode or bolometer mode MW/THz detector.

3.1 CNT Diode Mode Detectors

3.1.1 Physical Implications of Detection: ZBA and CNT based Diode mode

As previously mentioned in Chapter 1, the diode mode detection arises from the ZBA anomalies characteristic of CNTs. These sharp irregularities on the IV curves are the effects of *nonlinear* contact situations, which are produced when bad quality contacts give rise to energy barriers at the CNT-metal interface. Most of our devices, specially those from LPA generations 2, and 4, for which MW responsivity results were shown in Figures 2.22, 2.24, and 2.25, exhibited the *ZBA based diode mode*. Furthermore, even though this process is slightly different at THz frequencies, some of the devices (4A2 and 3C3) measured for THz responsivity -results shown in Figures 2.44 and 2.45- showed diode like responsivity operation.

$$Sv_{diode} = \frac{1}{4} \times R \times \frac{d^2 I}{dV_2} \times \frac{V_{MW}^2}{P_{MW}} \tag{27}$$

Determination of whether the devices followed the diode or the bolometer model was done by calculating the theoretical responsivity of each device. In order to do so, the

previously derived responsivity expression for the diode mode from (15), also repeated here as (27) for reference, was evaluated individually.

Let us first consider devices F2R and C3, in the low bias (i.e. less than 200mV) and low temperatures regimes. The respective IV characteristics (see Appendix 1) under these conditions clearly show the presence of a big contact barrier. It is clear than even in the case of C3, where a top layer of metal was present, completely *ohmic* contacts at both metal-CNT interfaces were not achieved. As such, *nonlinear* effects dominated transport under the low bias low temperature regions. Furthermore, in order to calculate response from (27), the resistance R and the d^2I/dV^2 factors were calculated from the IV curves at 4.2K for each device, while the V^2_{RF}/P_{RF} term was used as a fitting parameter. Theoretically, based on the impedance of the LPA at MW (Z_{MW}=50Ω) and THz frequencies (Z_{THz}=100Ω), this term should equal 200 or 400Ω , respectively. In other words, if we had a case where a large mismatch would have doubled the RF voltage, the V^2_{RF}/P_{RF} term obtained should have been near these values. Theoretical ideal responsivity values of device 4A2 for this 'perfectly matched' scenario have been calculated (Fig. 3.1) at 77 and 4.2 K simply for reference.

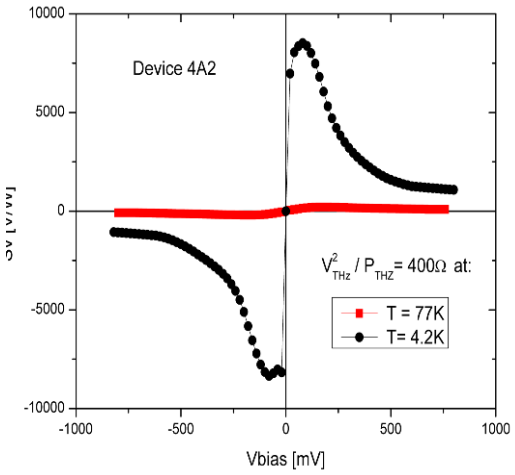

Figure 3.1 Ideal calculated diode like response for device 4A2 at 77K and 4.2K, if the V^2/P term would equal 400. This situation assumes that the RF voltage is doubled at the device.

Finally, the results of the fits are shown in Figures 3.2 and 3.3. In these plots we note that the calculated responsivity using the diode model, satisfactorily fits the experimental

data measured at 4.2 K (shown in black) for the four devices shown (3C3 was measured at 77 K). For F2R and C3 at 600MHz the V^2_{RF}/P_{RF} factor was 140 and 1300 Ω respectively, while for devices 4A2 and 3C3 at 0.760 and 0.694THz it was 0.23 and 0.25 Ω. The diode mode was thus much more efficient at MW than at THz. Two additional situations need to be addressed from the previous fits. First, the fact that a value greater than the maximum expected (200 Ω) for V^2_{RF}/P_{RF} was calculated for MW detection in one device (C3) and second, the fact that diode like CNT based detectors work at THz frequencies.

The nature of the first issue is important, since it questions the validity of these results (i.e. diode mode CNT detection) and the traditional microwave theory used to describe these situations. The answer to this discrepancy could involve a more rigorous reformulation of our models or it could even be a hint of other known physical processes in CNTs (i.e. Coulomb blockade). Unfortunately, no clear resolution can be provided based on the data gathered up to this point. In order to identify Coulomb blockade one typically varies a gate voltage, which was not easy to implement in our structure. We note that no 77 K measurements were performed for which V^2/P exceeded its expected theoretical value, and that the Coulomb blockade effects are not expected to occur at 77 K.

The second issue, the explanation of CNT detection in the diode mode at THz, is also quite complex. Claiming that a complete understanding of these processes has been obtained would not be accurate. Here, we simply hypothesize a probable explanation based on known contact effects. It has been well documented [37] that CNT-metal interfaces exhibit a contact resistance and a capacitance, and both of these have a relation to how much overlap there exists between the CNT and the metal. Therefore, by examining the SEM pictures of devices 4A2 and 3C3, we note that this CNT-metal overlap is very small. We believe these devices had uncharacteristically small contact capacitances, and as a result THz currents were not able to go through the contact resistances. If this was the case, this diode mode detection would be entirely reliant on the contact resistance nonlinearity, and not only in the low voltage low temperature energy ZBA effects. This effect could prove to consistently give rise to a new type of diode like detectors. However, at this point this possible explanation remains but a hypothesis; more devices with similar configurations need to be fabricated and tested in order to properly validate this theory.

Now, we move on to briefly consider devices from the LPA1 generation, and their MW detection characteristics (Fig. 2.26). The first attribute that is important to remember is that these devices had very nice *ohmic* contacts, which at least at room temperature did not show any signs of any energy barriers. By examining their IV characteristics (Appendix 1) and MW responsivity results it is clear that the effects observed are simply those of the CNTs themselves (i.e. no contact effects). The clear current saturation which results in 'concave down' IV curves is the one entirely responsible for the MW responsivity. Similar fits to the ones described above have also been performed and it is evident that the detection follows d^2I/dV^2 as in the diode model discussed earlier for the contact nonlinearity. Also, the LPA1 devices show a much higher MW responsivity at 300 K than any other devices. They could not be tested at lower temperatures due to limitations of the measurement setup, but are likely to be capable (at low temperatures) of similar high responsivities as devices F2R and C3 of the LPA4 generation.

We will refer to two main types of diode models described in this section as the *'ZBA based diode model'*, and *'CNT based diode mode*'.

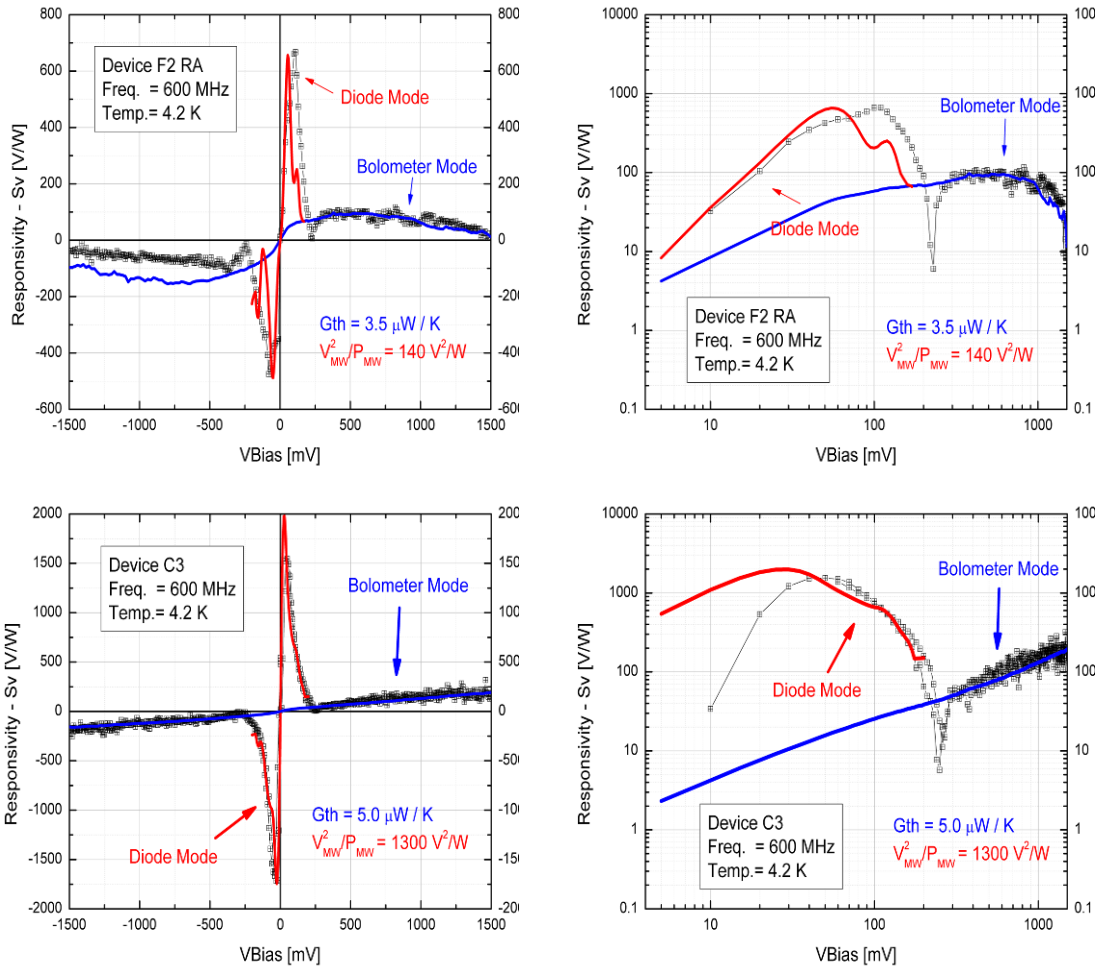

Figure 3.2 Direct MW responsivity vs. voltage in linear (left column) and logarithmic (right column) scales for devices F2R (top) and C3 (bottom). Measured responsivity is shown in black dots, while diode and bolometer mode fits are shown in red and blue respectively. Both of these devices, as confirmed by AFM analysis, consisted of only one single SWCNT. Additionally, the MW response for both measurements was measured by applying 600MHz signal at 4.2K.

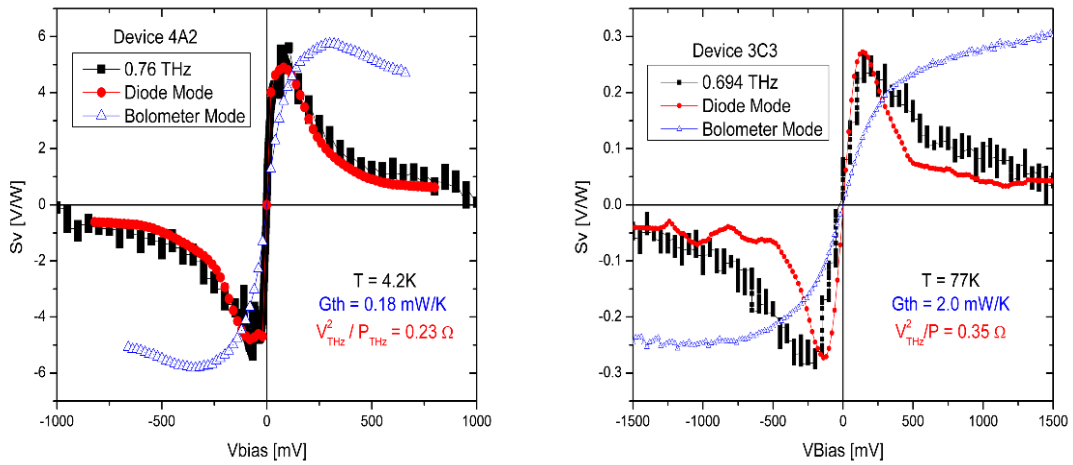

Figure 3.3 Direct THz responsivity vs. voltage for devices 4A2 (left) and 3C3 (right). Measured responsivity is shown in black dots, while diode and bolometer mode fits are shown in red and blue respectively.

3.2 CNT Bolometer Mode Detectors

3.2.1 Physical Implications of Detection

Using similar tools (i.e. the results from the DC, MW, and THz characterization) as the ones employed to describe the physical implications of the diode mode sensors, we now proceed to describe the bolometer mode CNT detectors. We will examine devices which have shown bolometric type detection at MW and THz frequencies. Two different principles of operation will be distinguished, and the nature behind each of them will be explained. Furthermore, as previously mentioned when describing the bolometer model of detection, the direct response either at MW or at THz is mainly the product of a non-linearity present in the resistance-temperature (dR(T)/dT)) characteristics. This temperature dependent resistance (Fig. 3.4) is what gives rise to the detection.

First we start by examining devices F2R and C3 under their high bias and low temperature regimes of operation. These two devices detected MW frequencies of up to 3GHz (limited by the source chosen, not the devices), and their IV curves (Appendix 1)

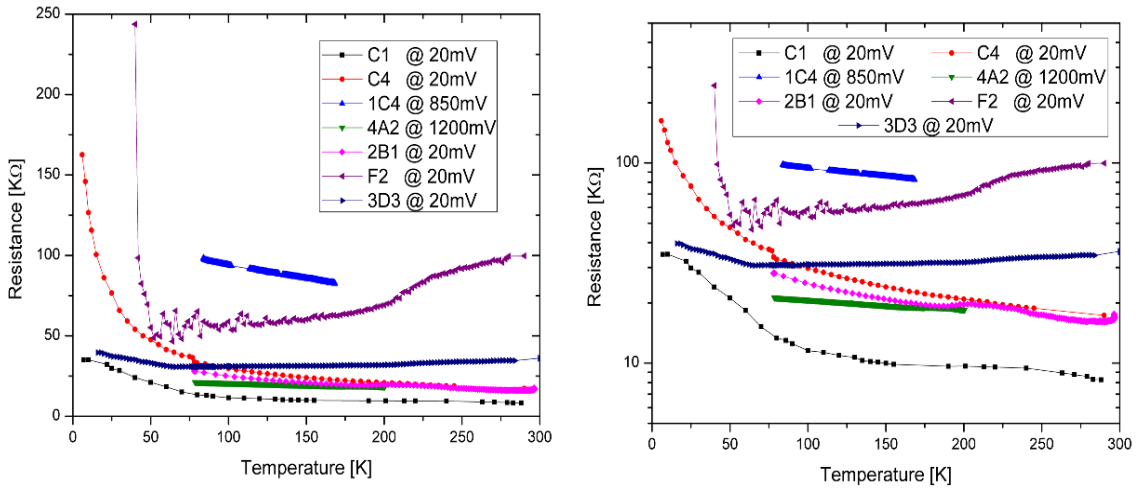

Figure 3.4 Resistance as a function of temperature for various devices. Refer to table 2.2 and 2.3 for details regarding LPA generation, resistance values at selected temperatures, and tests performed on each device.

clearly exhibited the current saturation characteristic of CNTs. As such, it can be deduced that at high voltages we have by-passed any contact effects present at the low bias. In other words, higher voltages inject more energy into the electrons that move inside the tube and therefore they go over any energy barrier present. Consequently, this saturation is clear evidence that any detection effect derived or observed will be solely a consequence of the CNT itself.

Now, in order to describe the detection, just like in the diode mode case, a the theoretical responsivity was calculated using

$$Sv_{bolometer} = \frac{I_O}{G_{th}} \times \frac{dR}{dT} \tag{28}$$

For this calculation, the I_O and the dR/dT terms were obtained from the DC characteristics at 4.2K, while the G_{th}, was the variable fitting parameter. Theoretically and experimentally, several values for G_{th} for a single CNT of different lengths have been carefully calculated and measured in [35] and [60]. Furthermore, for temperatures near 4.2K the thermal conductance is in general on the order of a few nW/K. However, the empirical values

obtained from our fits (shown in Fig 3.2) differ by three orders of magnitude. Simultaneously, for our group, the 3.5 - 5μW/K is one of the smallest thermal conductance values obtained for a CNT device fabricated at UMass. This discrepancy (i.e. of almost three order of magnitude) can be attributed to different CNT configurations (length, suspended vs. supported, etc), major power losses due to mismatch (~21dB load mismatch attenuation), and the presence of small barriers at the contacts. Note that the impedance mismatch has a quite different effect in the bolometer mode since in this mode power must be absorbed. Once again, by looking at the plots from Figure 3.2 it is evident that the CNT based bolometric model is the one that describes detection in devices F2R and C3, for the high voltage and low temperature regions. This type of bolometric detection has not been observed by our group previously at MW frequencies. In conclusion, we have shown that CNT devices bolometrically detect MW and THz signals to almost 400 and 60 V/W respectively with approximately 3 to 5 μW/K values of thermal conductance. It is also important to note that not all the devices measured at MW frequencies exhibited the bolometer-like mode at high bias; this was simply the result of more efficient CNT heating due to smaller energy barriers obtained by improving the contacts.

Additionally, similar fits were also used in order to account for devices from the LPA3 generation which detected at THz. Nonetheless, due to the contact dominated situation, the necessary heating of electrons inside the CNT bundles would have been very small. Thus, in the cases described below, we hypothesize a different type of bolometer: *"the two-step bolometer."* In this type of bolometer, we propose the existence of heating of the bundles due to THz currents that bypass the contact resistances (R_C) due to the well documented [37] contact capacitances (C_C). These C_C have been previously measured by our group to be between 10 - 40fF. These values, at THz, would be enough in order to effectively shunt the contact resistances (R_C) also present. In general, it is proposed that as a first step, THz currents are absorbed by the CNT bundles with the help of the C_C. In the second step, the heated electrons tunnel through the contact barriers into the contact reservoir, where they can be measured as a change in the device's DC current (or voltage). It is clear that more measurements of C_C are needed in order to further justify the validity of the "two-step" bolometer. These additional values are now available in Chapter 2 of this thesis, and they

serve as evidence of large contact capacitances present in our devices. It is important to remember that we are making the assumption that these Cc, present at MW frequencies (up to 10-15GHz), will still be relevant all the way up to the THz frequency range., which may not be the case.

Furthermore, just like in the previous CNT based MW bolometer, thermal conductance (G_{th}) values were empirically calculated from the fits to the THz data. The values obtained at 77K and 4.2K ranged from a few hundreds to thousands μW/K.

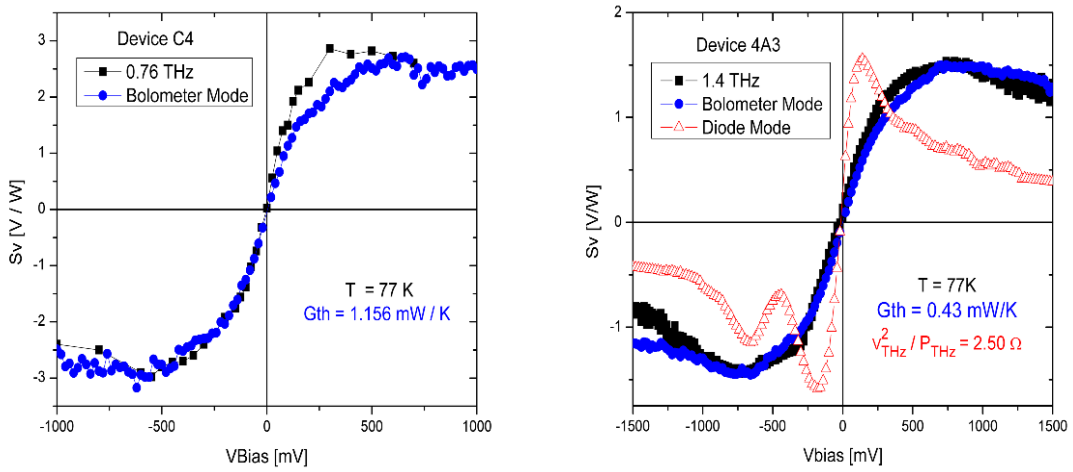

Figure 3.5 THz detection of devices C4 and 4D3 conforming with the bolometer model. Both measurements were done at 77K, and at 0.76 and 1.4THz respectively.

CHAPTER 4
FUTURE WORK

4.1 Device Fabrication Techniques: CNT CVD Growth and E-Beam Lithography

Through-out the duration of this three year long project several fabrication techniques have been learned, implemented, and improved in order to obtain the type of devices presented. In this thesis alone, several schemes in order to facilitate the placement of CNTs on our LPA structures have been outlined. However, the difficulty, time consuming nature, and limitations of using several mask steps and placing CNTs using DEP cannot be overstated. Currently, there exists new resources available at UMass which will allow our group to move away from the fabrication methods used for this work and improve the quality of devices drastically. Basically, the new availability of a well equipped nanofabrication facility (CHM clean room) in which our group has already been working in for the past few months, opens several possibilities on how to improve our devices. Two approaches are suggested: CNT CVD Growth and E-Beam Lithography. The first one would require extensive initial preparation, but once the setup and the recipes have been worked out, it could lead to much better control of the CNTs. Single CNT devices could be fabricated more easily than with DEP, and systematic measurements varying the CNT configurations (i.e. 1,10,20 tubes) could be done. The second proposed idea, has already been in progress for the past month or so. Basically, by using e-beam lithography we could deposit metal contacts anywhere along a nanotube. In this manner, we could select the effective length of devices as well as improve the quality of contact interfaces. Additionally, since the metal layer would be deposited on top of the tube, two mask steps or more cumbersome schemes to properly contact the CNTs would become obsolete.

4.2 THz Measurements: Heterodyne Experiment

For the continuation of the THz explorations of CNTs, we plan to perform heterodyne measurements using two lasers. Preferably, these experiments will be done on devices obtained using some of the fabrication techniques suggested above. As such, these devices

will not have nearly as much contact related effects, and the CNT properties at THz could be probed easier. A heterodyne measurement is a standard way of characterizing high frequency direct detectors; for this purpose, we explore some hypothetical situations and consequences of performing this measurement. First we estimate the conversion gain (G_C) in the heterodyne mode from the responsivity in the direct detector mode [61]:

$$G_C \approx \frac{2S_V^2 P_{LO}}{R_L} \tag{29}$$

Here, P_{LO} is the local oscillator power and R_L the load resistance at the IF. Now, if we considered even a moderately good S_V = 1,000 V/W, P_{LO} = 10^{-6} W, and R_L = 100 Ω, we estimate a conversion gain of -17 dB. Furthermore, since the responsivity of our CNTs can potentially be much higher (Fig. 4.1) the prospects for realizing a very efficient mixer are excellent. Moreover, the predicted temperature dependence of the responsivity (Fig. 4.1) is very slow, showing the potential for operation at least up to about 100K. However, Eq. (29) assumes that the IF output is matched to the IF amplifier and this would require a matching circuit. Alternatively, some IF mismatch may be tolerated, or for example traded against using higher LO power.

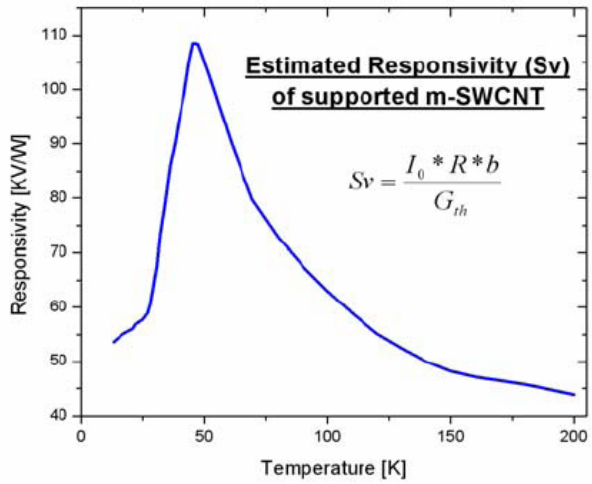

Figure 4.1 Calculated ideal responsivity for 3μm SWCNT. From ref. [62]

4.3 MW Measurements: Cryogenic and Bias Dependent S-parameter Measurements

In this thesis, results from S-parameter measurements on several CNT devices ranging from 50 Ω to 40 KΩ, were presented. These results served to understand better how the different CNT resistances and configurations affected the MW reflections at the CNT-metal interfaces. However, it has also been a recurring theme throughout this thesis that contact effects (i.e. energy barriers) affect CNT properties much more drastically near the zero voltages. As such, the MW reflections (i.e. S-parameters) could drastically be reduced by simultaneously applying a bias voltage and introducing enough energy for electrons to tunnel through the barriers. For this purpose, bias dependent S-parameter measurements become important. This initiative has already taken place for some of the measured devices that were presented in the earlier chapters; however, appropriate de-embedding and further analysis of this data needs to be completed. This analysis will constitute a very immediate future goal.

Furthermore, it was also evident from the DC, MW, and THz measurements that at cryogenic temperatures these so-called 'barriers' increase. Therefore, cryogenic probed S-parameter measurements should also be explored in order to understand better the CNTs ZBA's.

APPENDIX 1

BOLOMETER RESPONSIVITY DERIVATION DETAILS

First, let us recall the circuit model for a typical bolometer, as well as the four main equations (8) - (11) that were obtained in chapter 1.

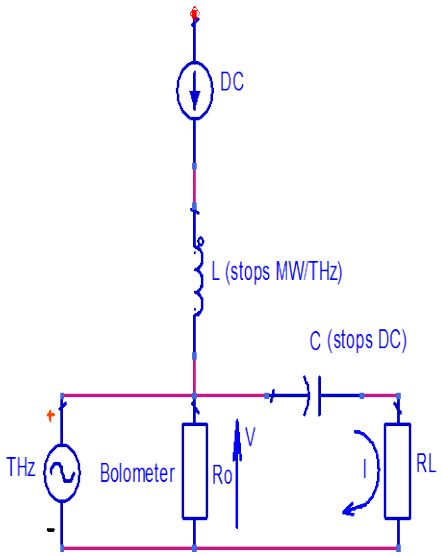

Figure AP1.1 Circuit model for a typical bolometer. Note that in this case, the 'incident' RF power is represented by a THz source

(8) or (AP-1) $V_o + \Delta V = (I_o - \Delta I) \times (R_o + \Delta R) = \underbrace{I_o R_o}_{Vo} + \underbrace{I_o \Delta R - R_o \Delta I}_{\Delta V}$

(9) or (AP-2) $P_{DC}^0 + \Delta P_{DC} = (V_o + \Delta V) \times (I_o - \Delta I) = \underbrace{I_o V_o}_{P_{DC}^0} + \underbrace{I_o \Delta V - V_o \Delta I}_{\Delta P_{DC}}$

(10) or (AP-3) $$R_L = \frac{\Delta V}{\Delta I}$$

(11) or (AP-4) $C_o = \frac{dR}{dP} \approx \frac{\Delta R}{\Delta P} \longrightarrow \Delta R = C_o \cdot \Delta P = C_o \cdot (\Delta P_{RF} + \Delta P_{DC})$

Our main objective now will be to obtain an expression for the change in current (ΔI) as a function of the RF power (P_{RF}) and the load resistance (R_L). For this, we first proceed to write (AP-2) in terms of ΔI, R_L, and R_o by substituting (AP-3). Then we have

(AP-5) $\Delta P_{DC} = I_o \Delta V - V_o \Delta I$, from (AP-2)

(AP-6) $\Delta P_{DC} = R_L I_o \Delta I - R_o I_o \Delta I$, by inserting (AP-3)

(AP-7) $\Delta P_{DC} = (R_L - R_o) \cdot I_o \Delta I$, simply re-writing (AP-6).

We repeat the procedure with equations (AP-1) and (AP-3). We obtain

(AP-8) $\Delta V = I_o \Delta R - R_o \Delta I$, from (AP-1)

(AP-9) $R_L \Delta I = I_o \Delta R - R_o \Delta I$, by inserting (AP-2)

(AP-10) $\Delta I (R_L + R_o) = I_o \Delta R$, simply re-writing (AP-9).

Now, we insert (AP-4) in (AP-10) to obtain a change in RF power $\Delta P_{RF.}$ We then have

(AP-11) $\Delta R = C_o \cdot (\Delta P_{DC} + \Delta P_{RF})$, from (AP-4)

(AP-12) $\Delta I (R_L + R_o) = I_o C_o \cdot (\Delta P_{DC} + \Delta P_{RF})$, by inserting (AP-11) in (AP-10).

Now, we replace (AP-7) for ΔP_{DC} in (AP-12) and we solve for ΔI. Then we obtain,

(AP-13) $\Delta I (R_L + R_o) = I_o C_o \cdot [(R_L - R_o) \cdot I_o \Delta I + \Delta P_{RF}]$, (AP-7) in (AP-12)

(AP-14) $\Delta I = \Delta P_{RF} \times C_o \times I_o \dfrac{1}{(R_L + R_o) \cdot \left(1 - C_o I_o^2 \dfrac{R_L - R_o}{R_L + R_o}\right)}$, solving for ΔI

Then, we apply the definition of responsivity (12) and obtain

(AP-15) $$Sv \equiv \frac{\Delta I_{RF} \cdot R_L}{P_{RF}} \quad , (12)$$

(AP-16) $$Sv = I_o C_o \times \frac{R_L}{\left(R_L + R_o\right) \cdot \left(1 - C_o I_o^2 \frac{R_L - R_o}{R_L + R_o}\right)}$$

Finally, we ignore the second term (electro-thermal feedback term) of (AP-16) since it will only affect our results if the responsivity is very high [40]. Now we substitute (6) for Co to obtain

(AP-17) or (13) $$Sv = \frac{I_o}{G_{th}} \frac{dR}{dT}$$

Expression (AP-17), also referred as (13) in the main text, will be the main equation describing bolometric responsivity that will be used through out this document.

APPENDIX 2:
ADDITIONAL DATA

In this section one can find analyzed data referred to in the previous chapters of this document. Specifically this section contains data from two measurements: DC testing and MW S-parameters measurements.

- <u>DC Testing:</u>

IV curves at selected temperatures, 300K (blue), 77K (red), and 4.2K(black) for all devices tested in this work not shown in the *DC Characterization* section.

- *LPA2 Generation Devices:* C1, C5

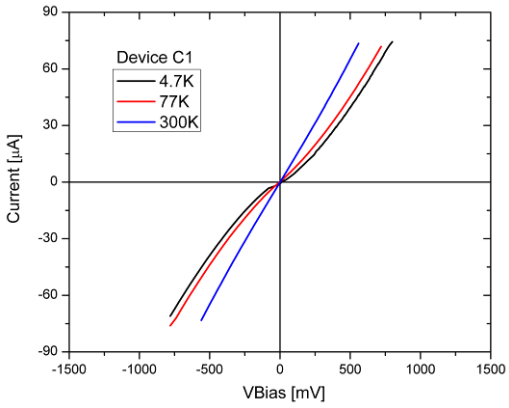

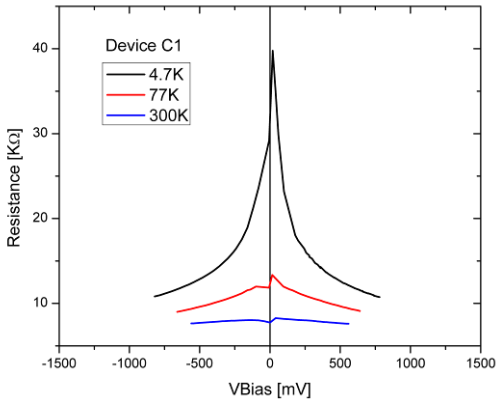

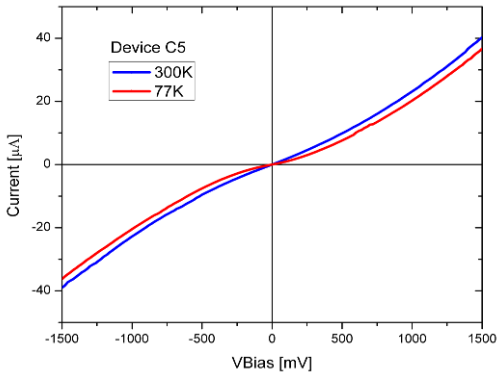

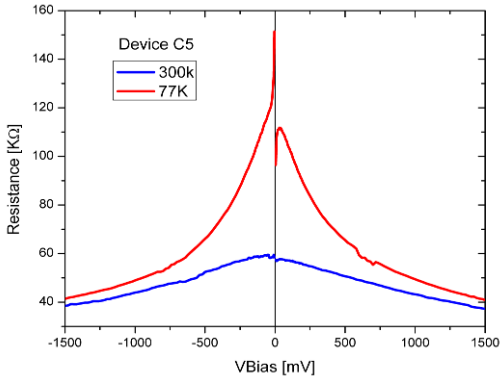

- *LPA3 Generation:* 1C4, 2B1, 3C3, 4A1, 4A2, 4A3, 4B2, and 4C4

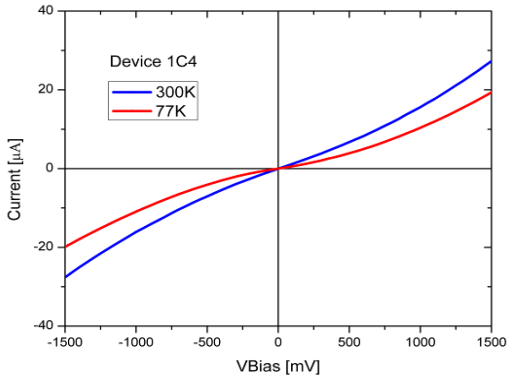

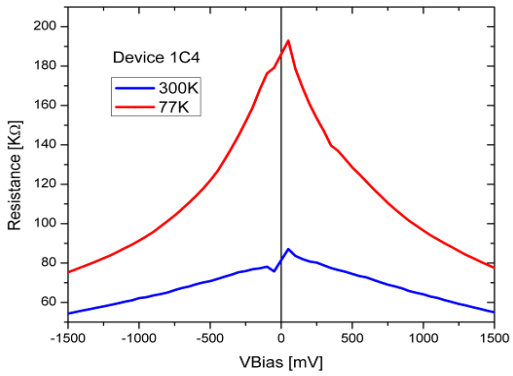

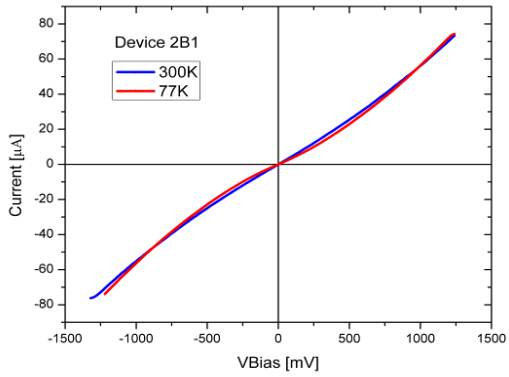

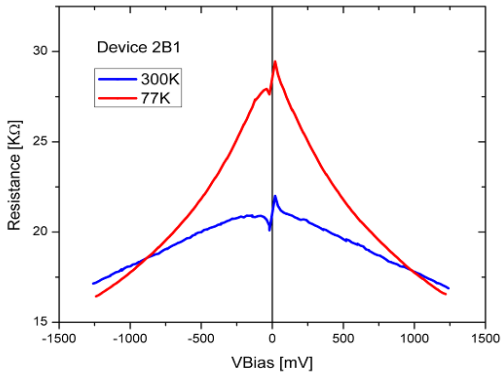

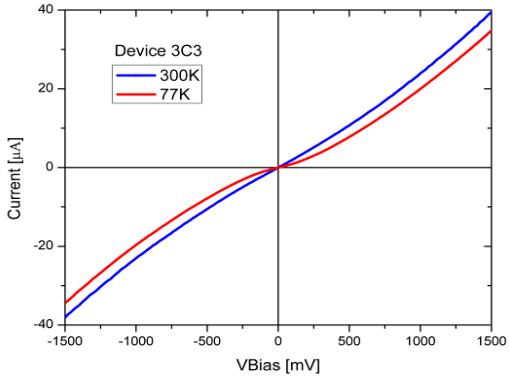

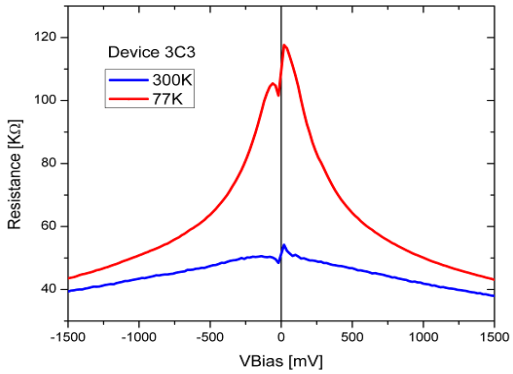

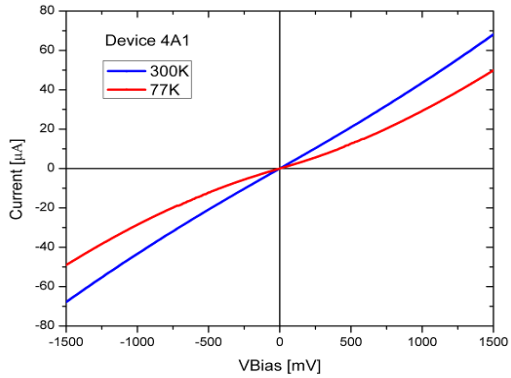
Device 4A1
300K
77K
Current [μA]
VBias [mV]

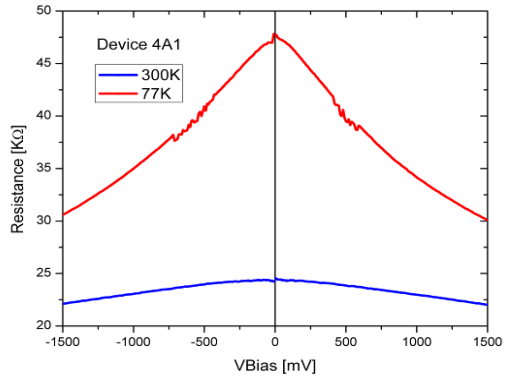
Device 4A1
300K
77K
Resistance [KΩ]
VBias [mV]

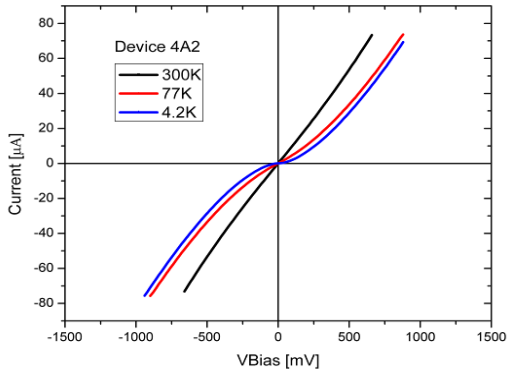
Device 4A2
300K
77K
4.2K
Current [μA]
VBias [mV]

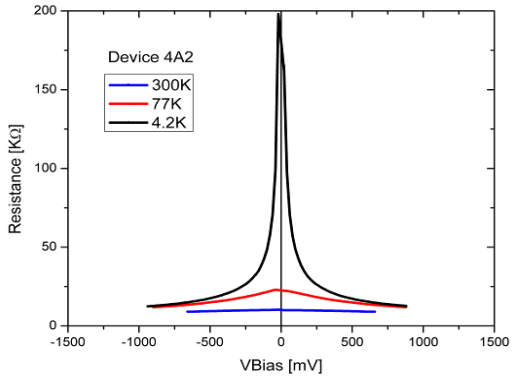
Device 4A2
300K
77K
4.2K
Resistance [KΩ]
VBias [mV]

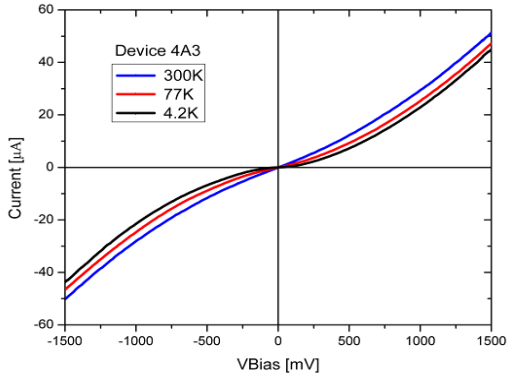
Device 4A3
300K
77K
4.2K
Current [μA]
VBias [mV]

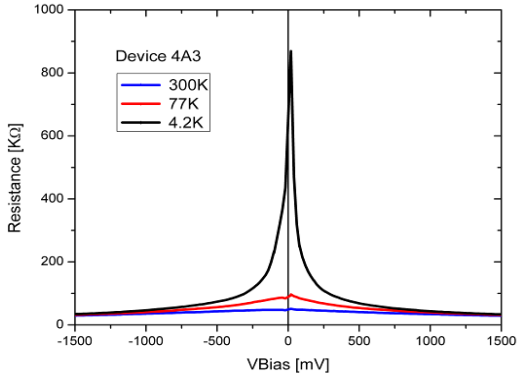
Device 4A3
300K
77K
4.2K
Resistance [KΩ]
VBias [mV]

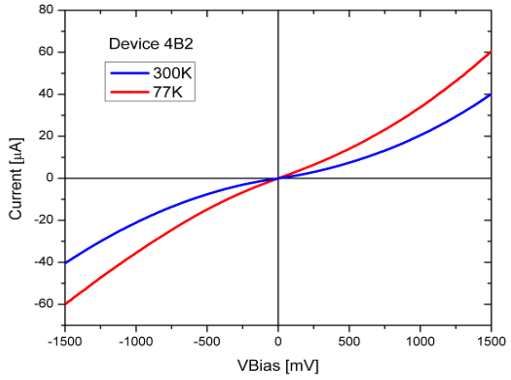
Device 4B2
300K
77K
Current [μA]
VBias [mV]

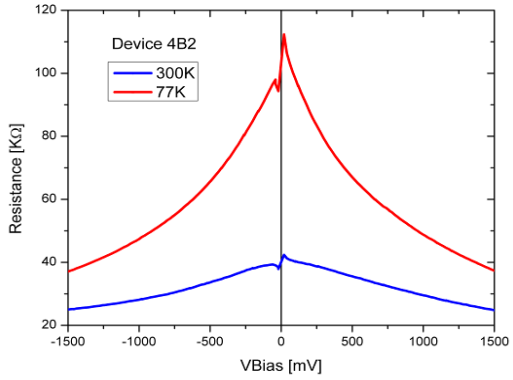
Device 4B2
300K
77K
Resistance [KΩ]
VBias [mV]

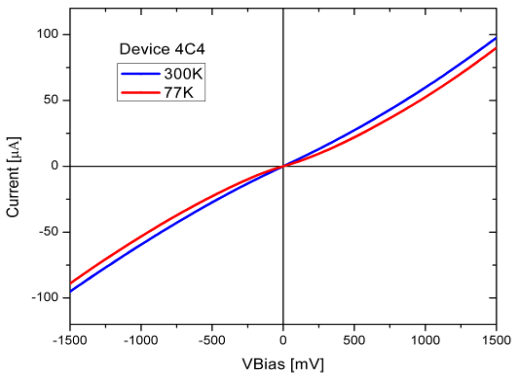

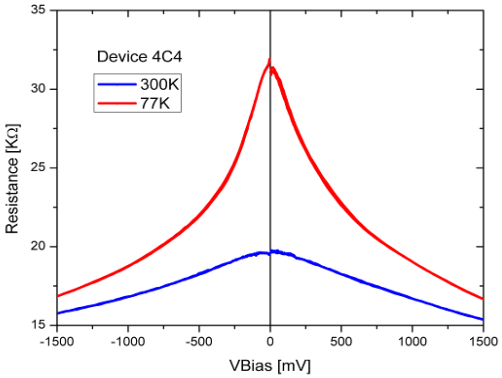

- *LPA4 Generation:* C2, C3, D1, F2, F2R

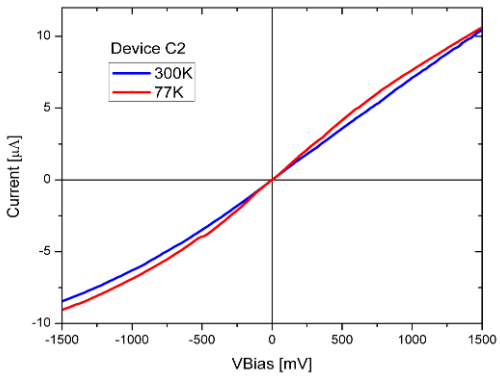

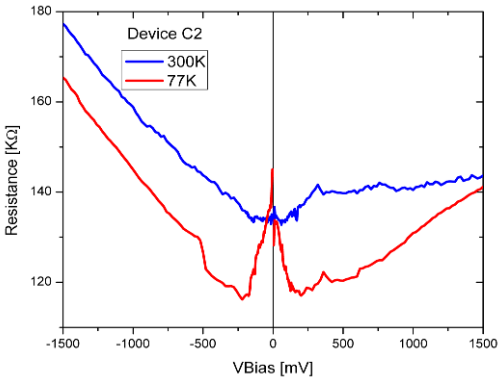

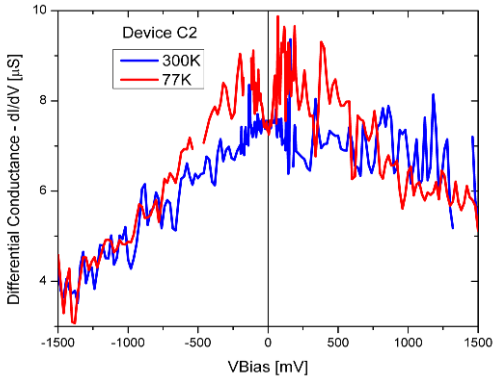

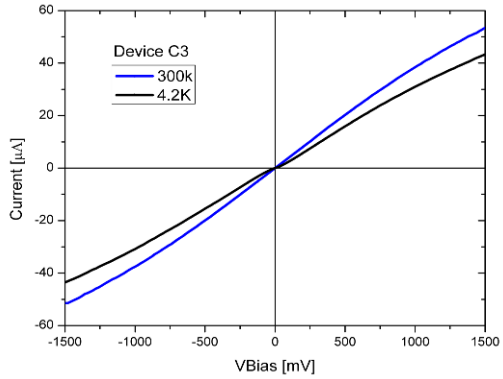
Device C3
300k
4.2K
Current [μA]
VBias [mV]

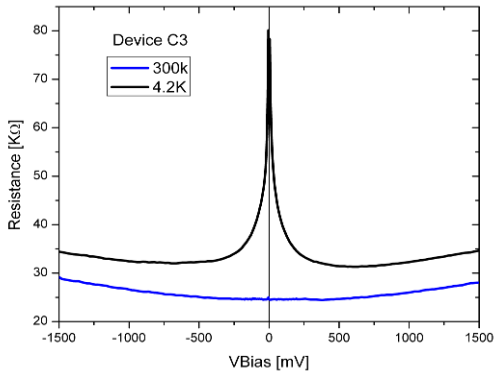
Device C3
300k
4.2K
Resistance [KΩ]
VBias [mV]

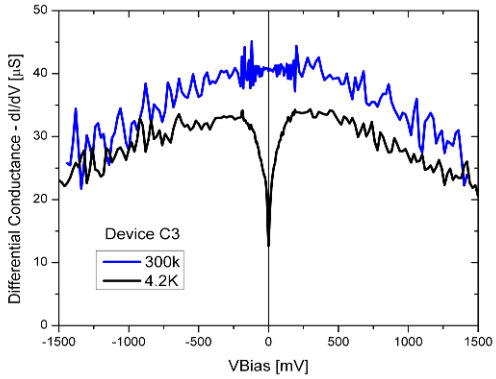
Device C3
300k
4.2K
Differential Conductance - dI/dV [μS]
VBias [mV]

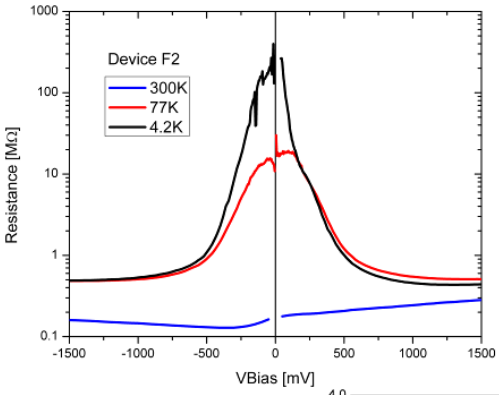
Device F2
300K
77K
4.2K
Resistance [MΩ]
VBias [mV]

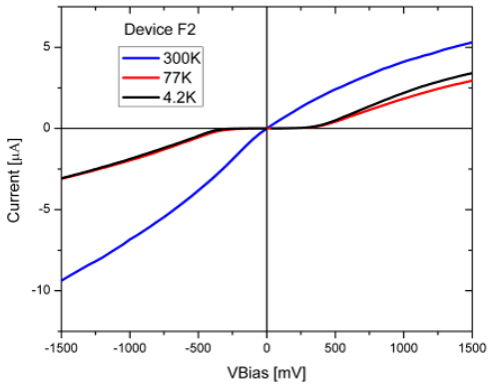
Device F2
300K
77K
4.2K
Current [μA]
VBias [mV]

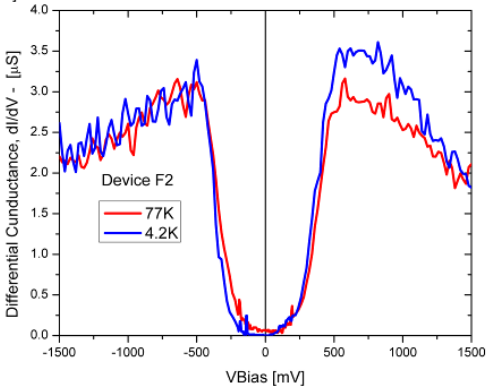
Device F2
77K
4.2K
Differential Cunductance, dI/dV - [μS]
VBias [mV]

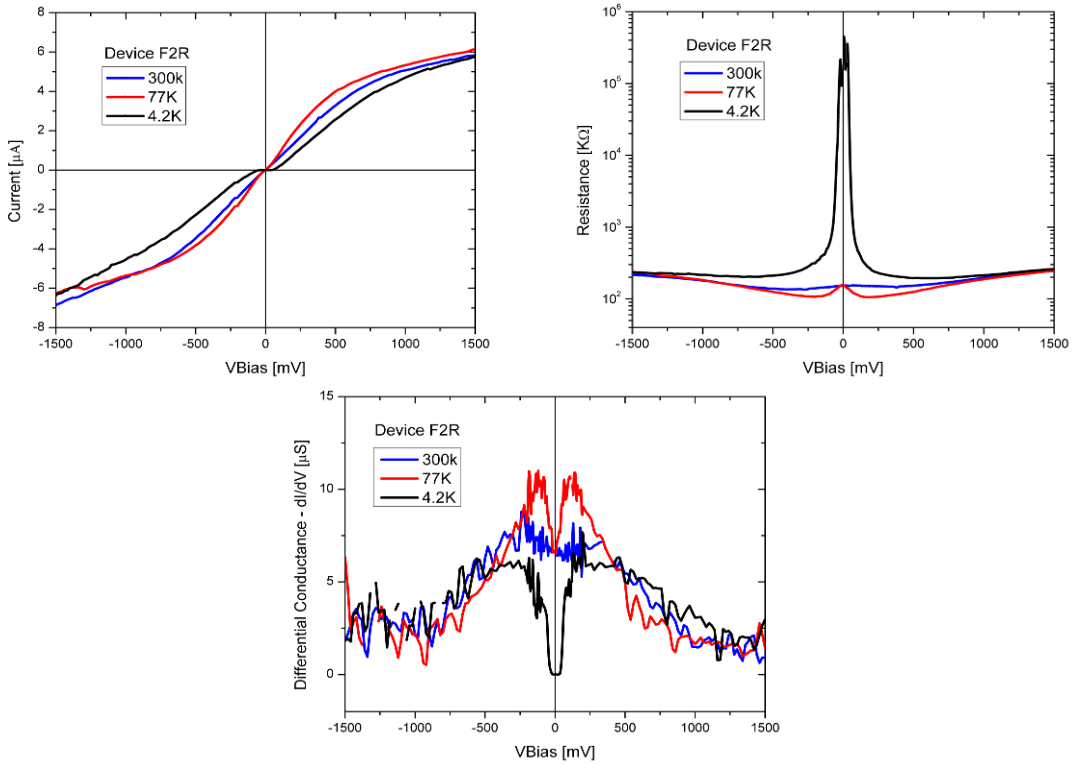

- Circuit Model Fits: Measured and simulated impedances from S-parameter meas.

50 - 900 Ohms Devices

Device D3A2 - 50 Ohms - Ohmic

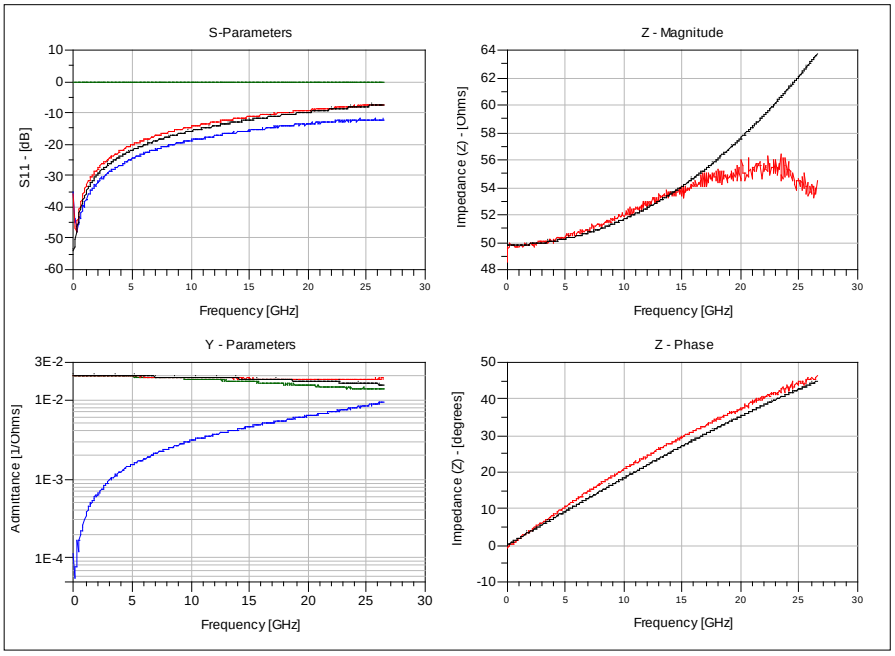

- With CNTs - No CNTs - De-embeded data -o- Simulated

Device D3A3 - 50 Ohms - Ohmic

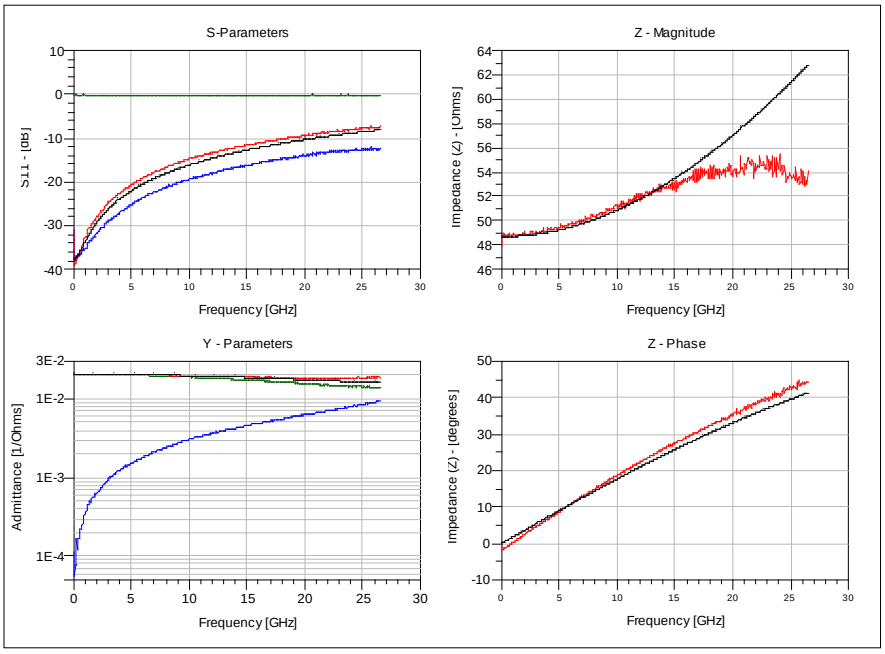

- With CNTs - No CNTs - De-embeded data -o- Simulated

Device D3A1 - 90 Ohms - Ohmic

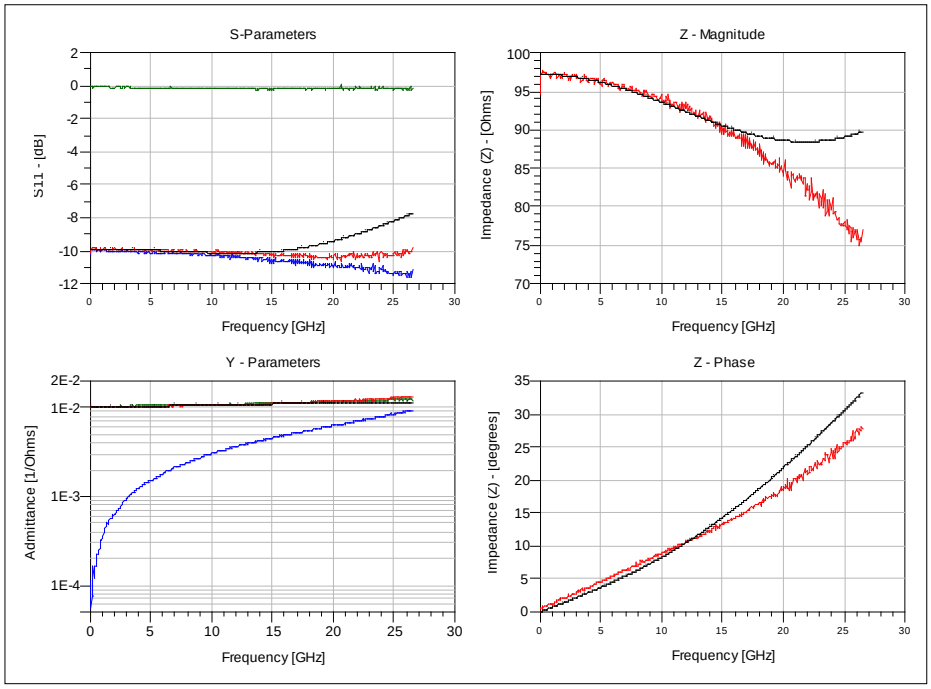

- With CNTs - No CNTs - De-embeded data -o- Simulated

Device D3C2 - 115 Ohms - Ohmic

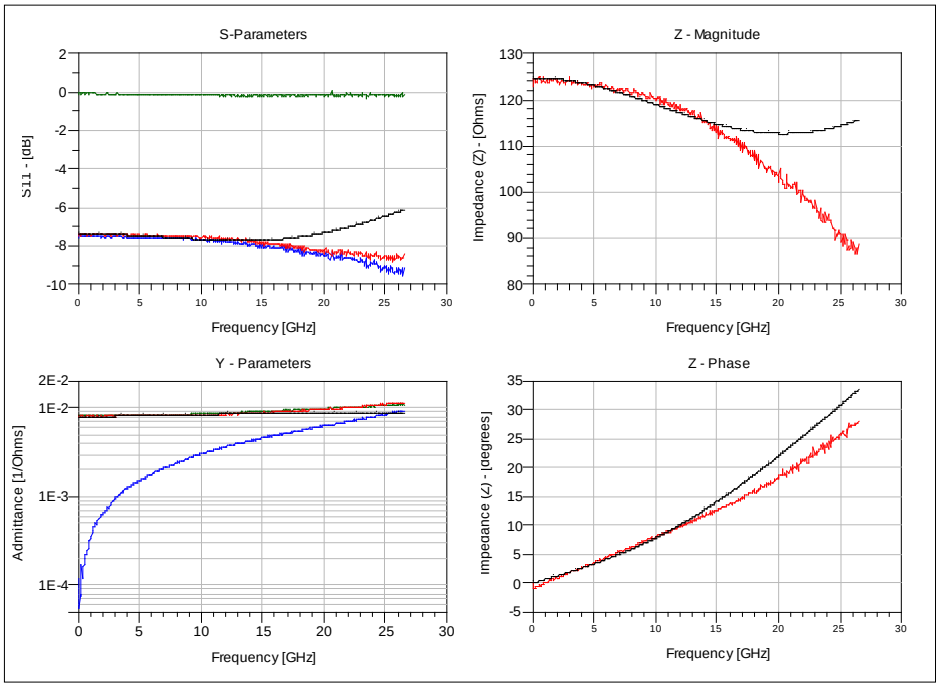

- With CNTs - No CNTs - De-embeded data -o- Simulated

Device D3B3 - 150 Ohms - Ohmic

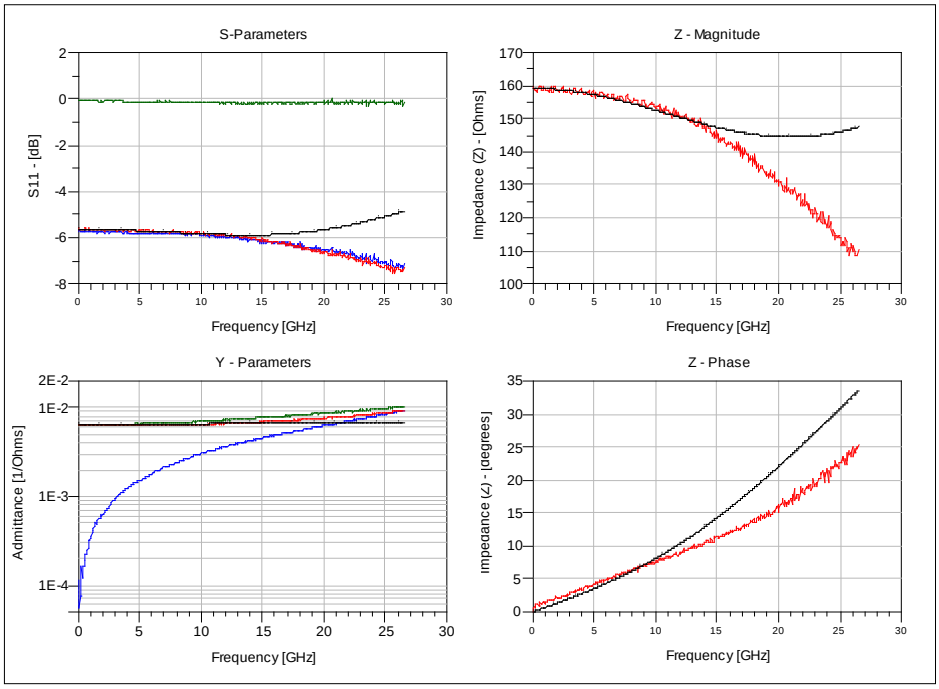

- With CNTs - No CNTs - De-embeded data -o- Simulated

Device D3C3 - 200 Ohms - Ohmic

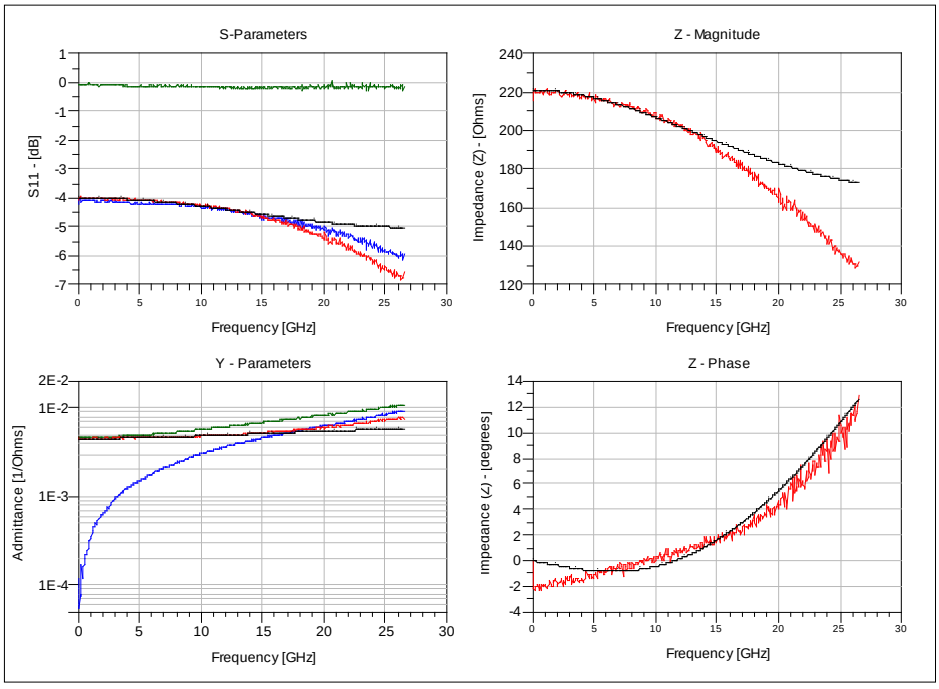

- With CNTs - No CNTs - De-embeded data -o- Simulated

Device D3B1 - 200 Ohms - Ohmic

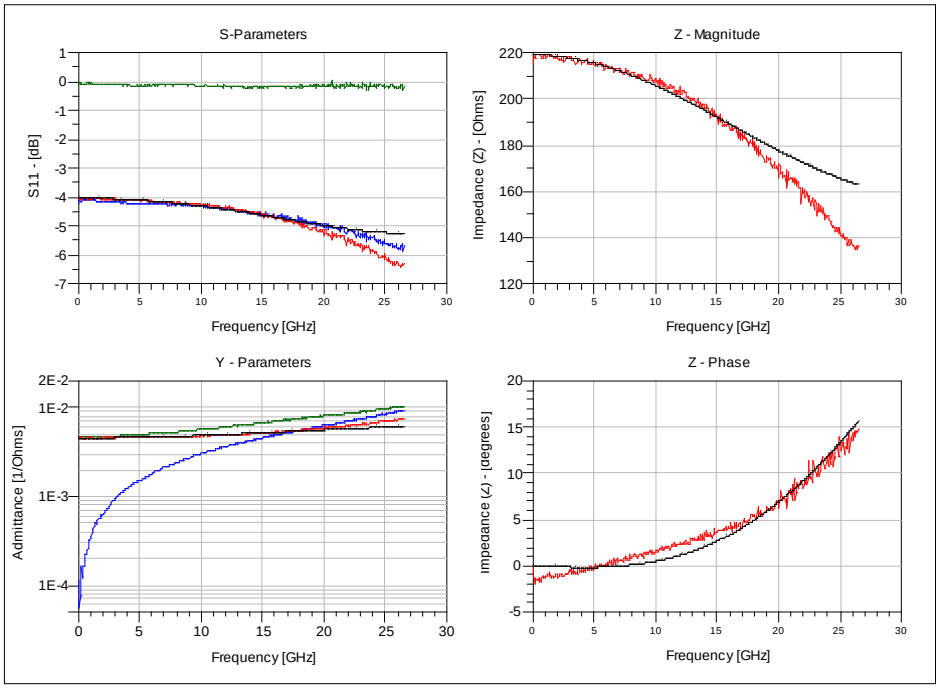

- With CNTs - No CNTs - De-embeded data -o- Simulated

Device D3B1 - 200 Ohms - Ohmic

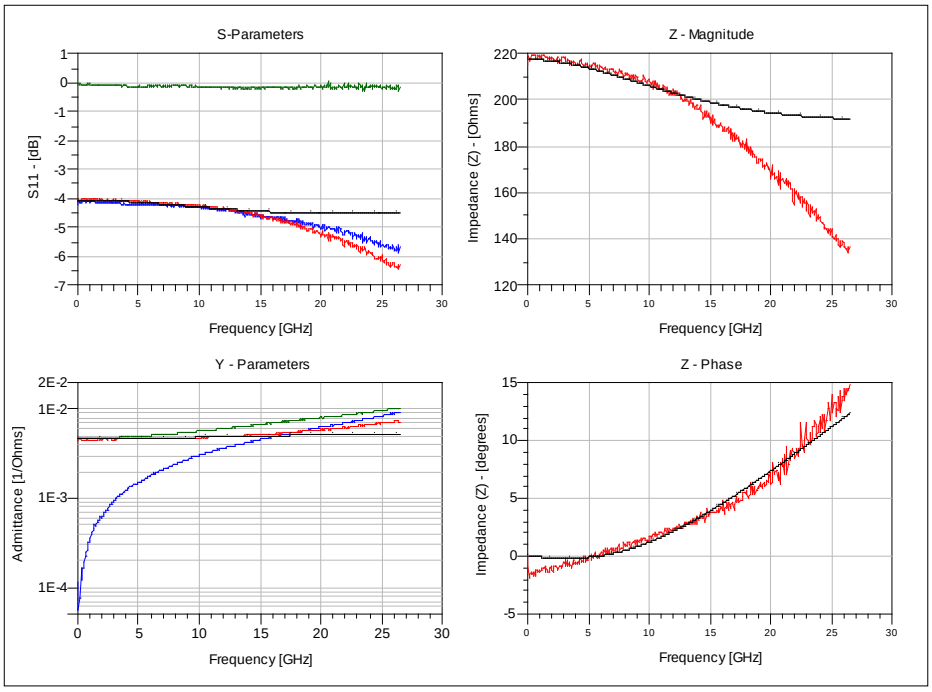

- With CNTs - No CNTs - De-embeded data -o- Simulated

Device D4A3 - 470 Ohms - Ohmic

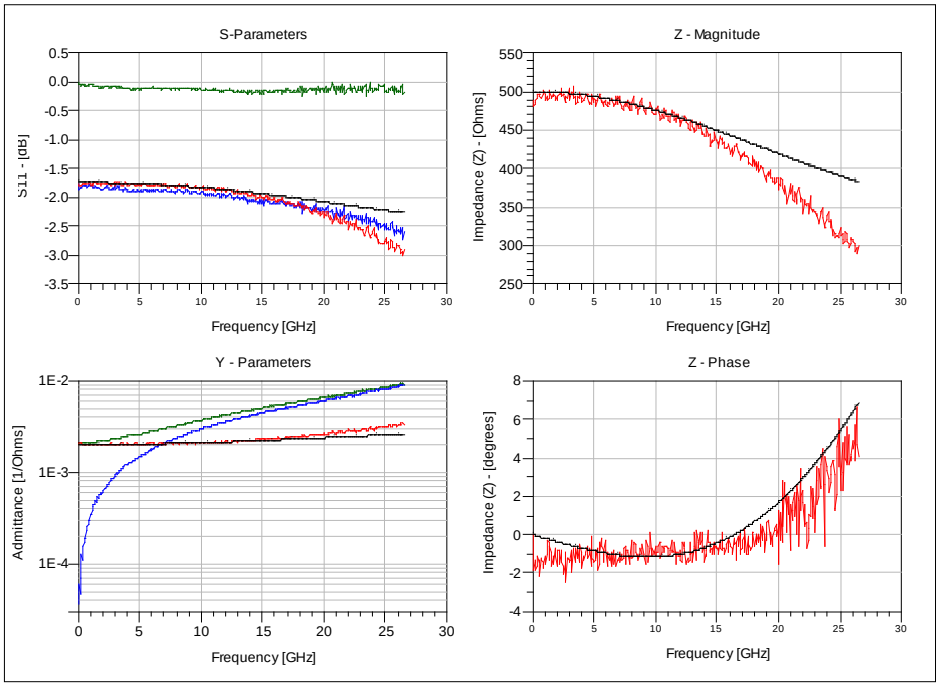

- With CNTs - No CNTs - De-embeded data -o- Simulated

Device B7C1 - 660 Ohms - Non-linear

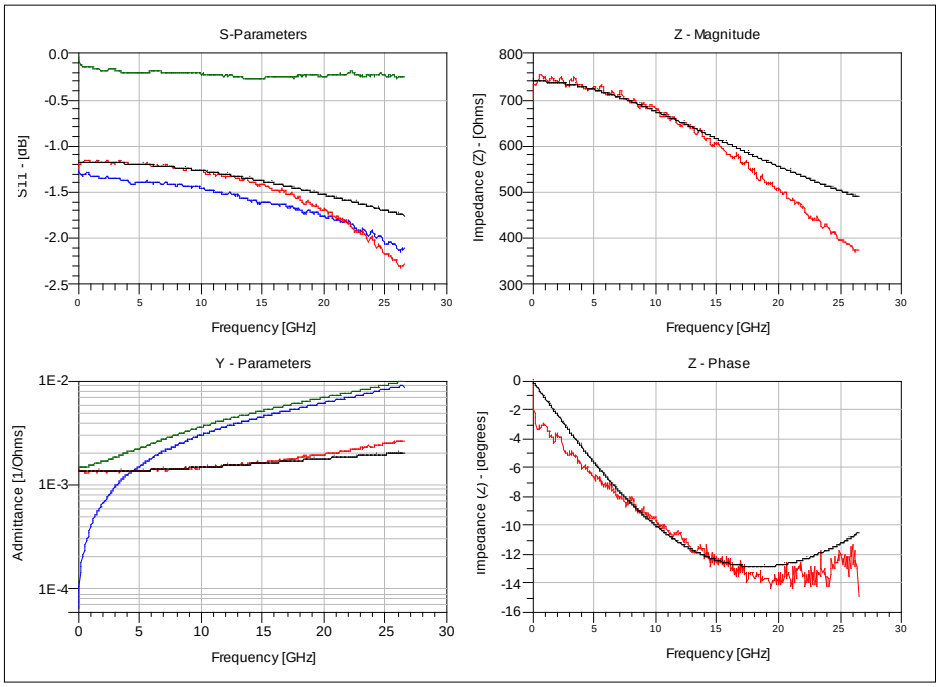

- With CNTs - No CNTs - De-embeded data -o- Simulated

Device D2C1 - 700 Ohms - Non-linear

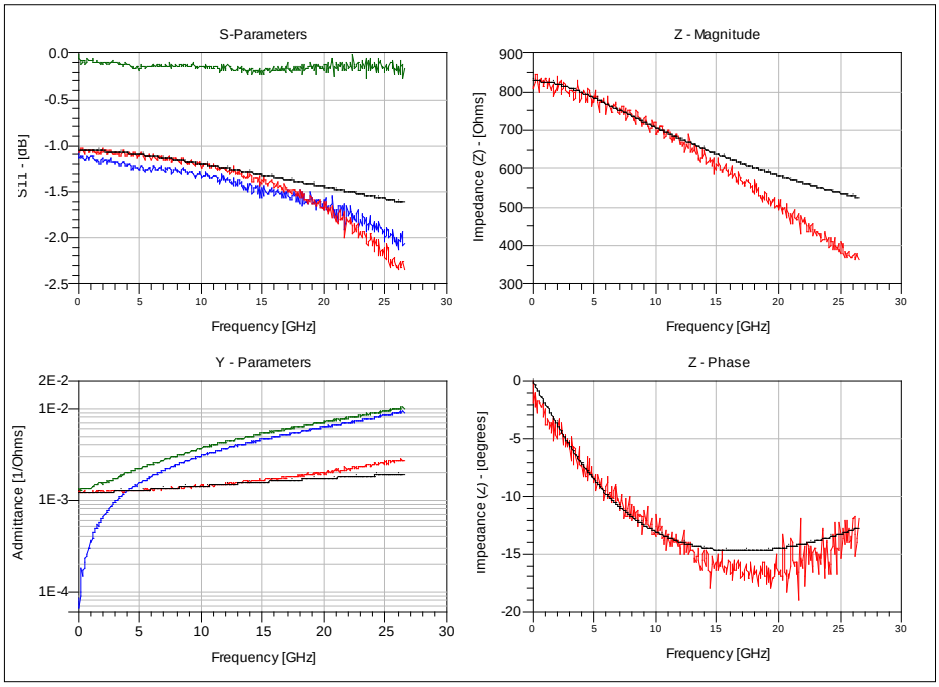

- With CNTs - No CNTs - De-embeded data -o- Simulated

Device D2C2 - 825 Ohms - Non-linear

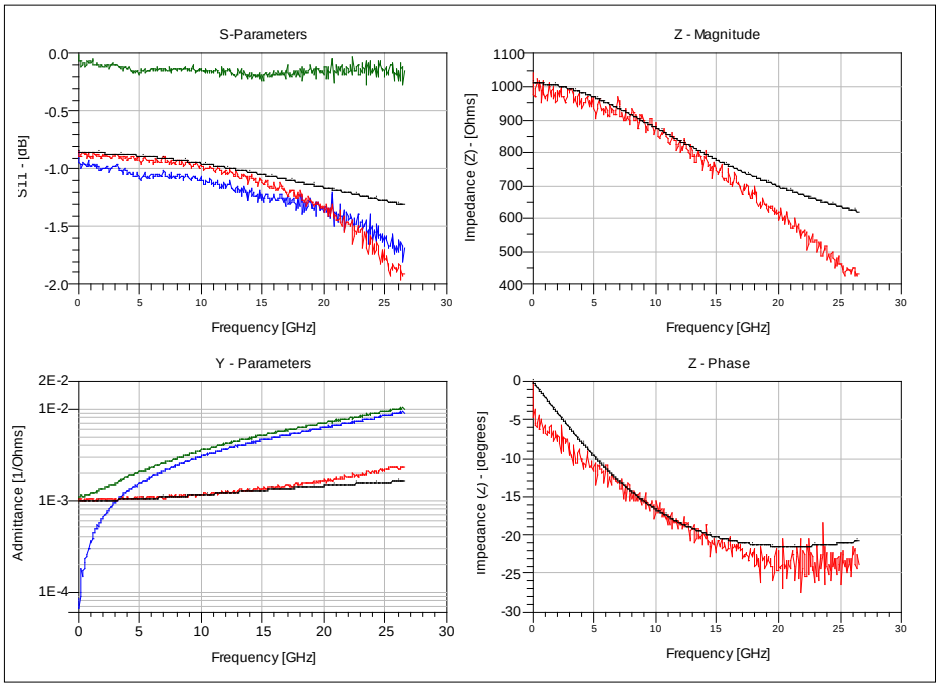

- With CNTs - No CNTs - De-embeded data -o- Simulated

1 -2 K Ohm Devices

Device B1B2 - 900 Ohms - Ohmic

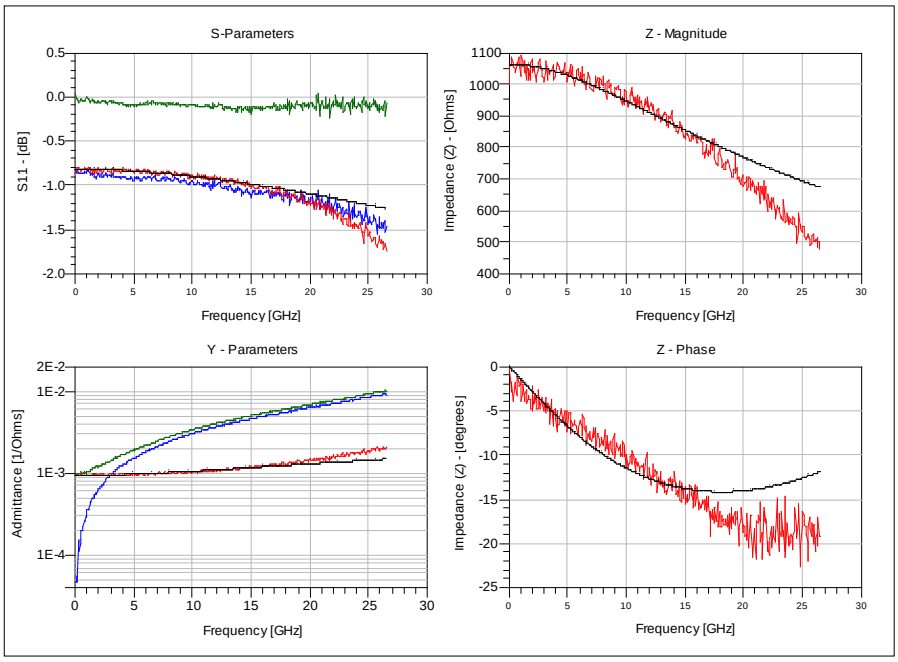

- With CNTs - No CNTs - De-embeded data -o- Simulated

Device B2C3 - 1KOhm - Ohmic

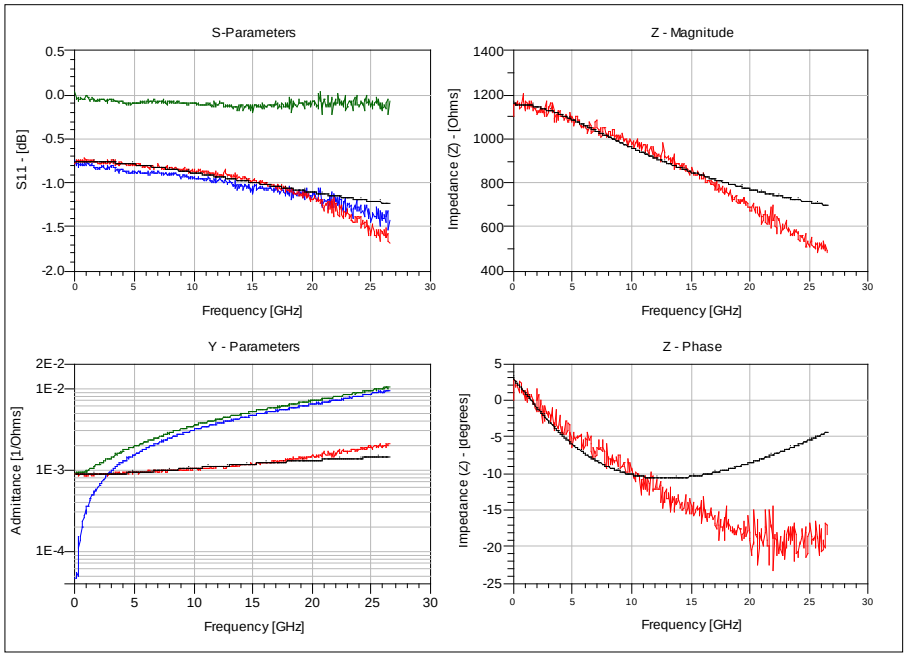

- With CNTs - No CNTs - De-embeded data -o- Simulated

Device C6C2 - 1.2KOhms - Non-linear

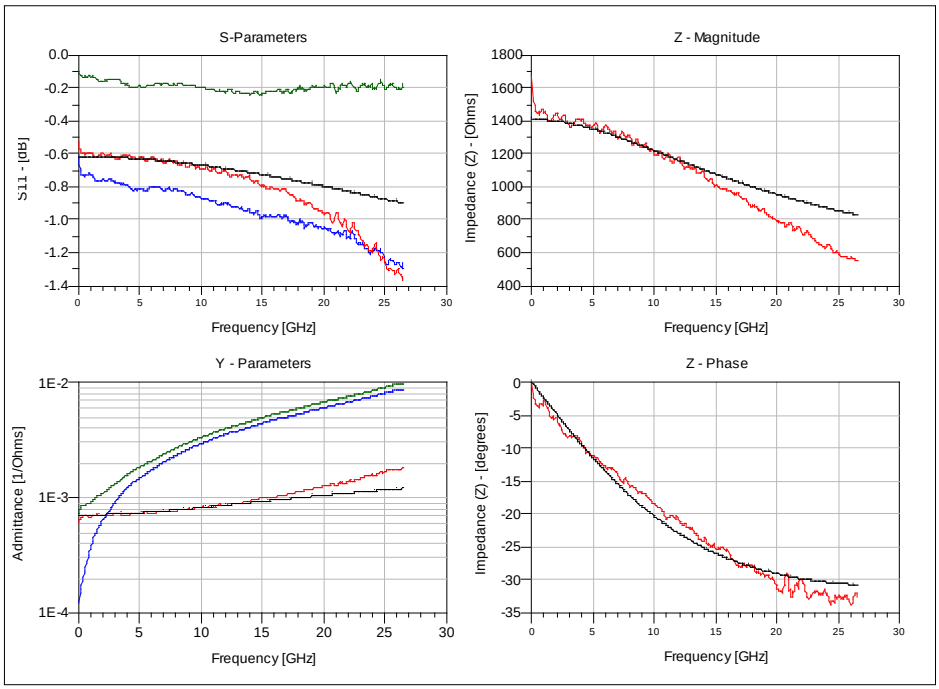

- With CNTs - No CNTs - De-embeded data -o- Simulated

Device B7A3 - 1.3KOhms - Ohmic

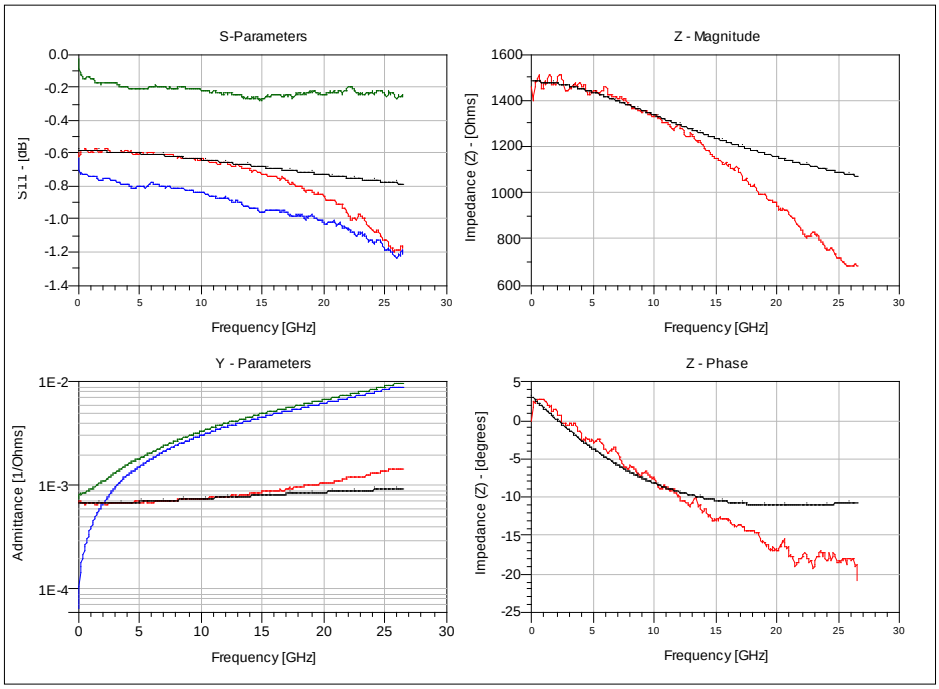

- With CNTs - No CNTs - De-embeded data -o- Simulated

Device A3C3 - 1.5KOhms - Ohmic

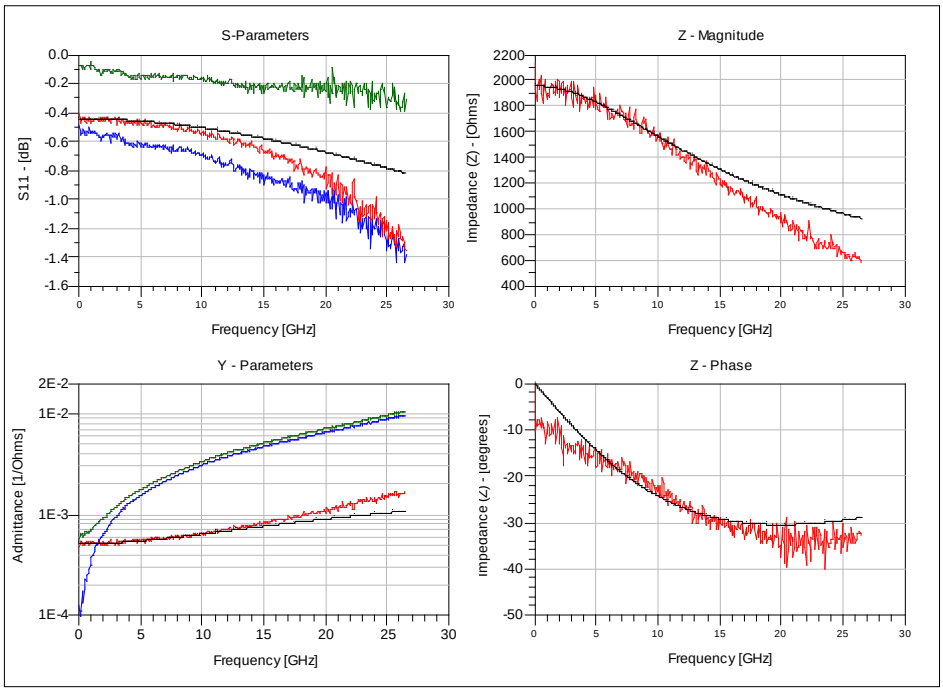

- With CNTs - No CNTs - De-embeded data -o- Simulated

Device B7C3 - 1.65KOhms - Ohmic

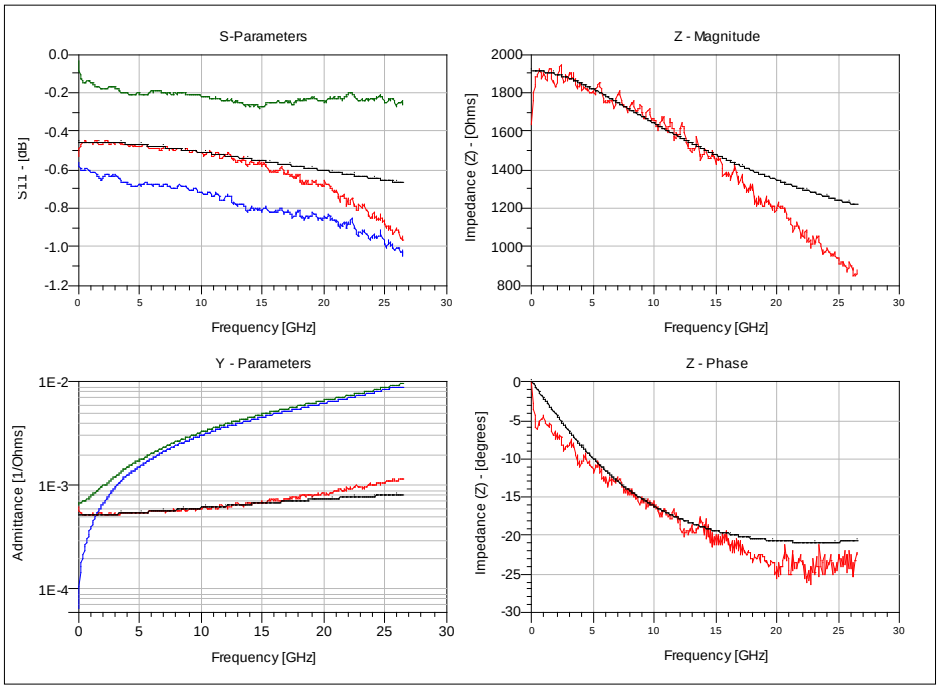

- With CNTs - No CNTs - De-embeded data -o- Simulated

Devices also measured for MW detection

Device D4A3 - 470 Ohms - Ohmic

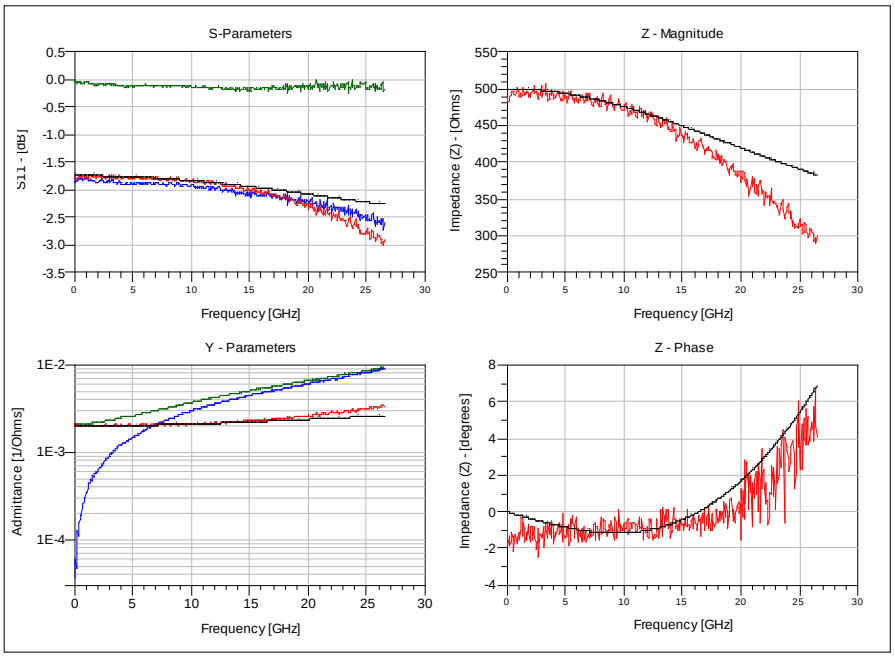

- With CNTs - No CNTs - De-embeded data -o- Simulated

Device A2A1 - 10KOhms - Ohmic

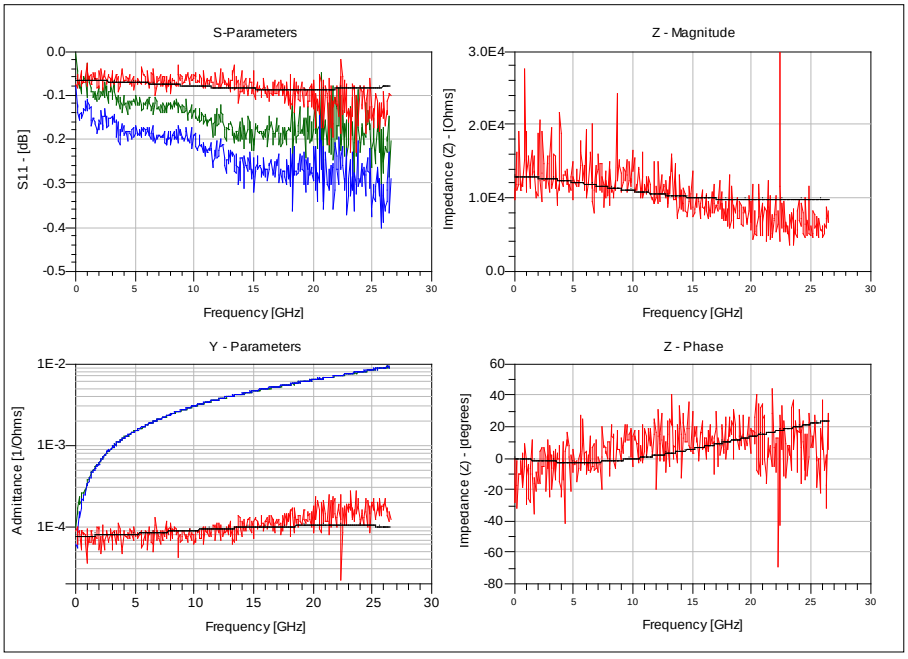

- With CNTs - No CNTs - De-embeded data -o- Simulated

Device A1B1 - 15KOhms - Ohmic

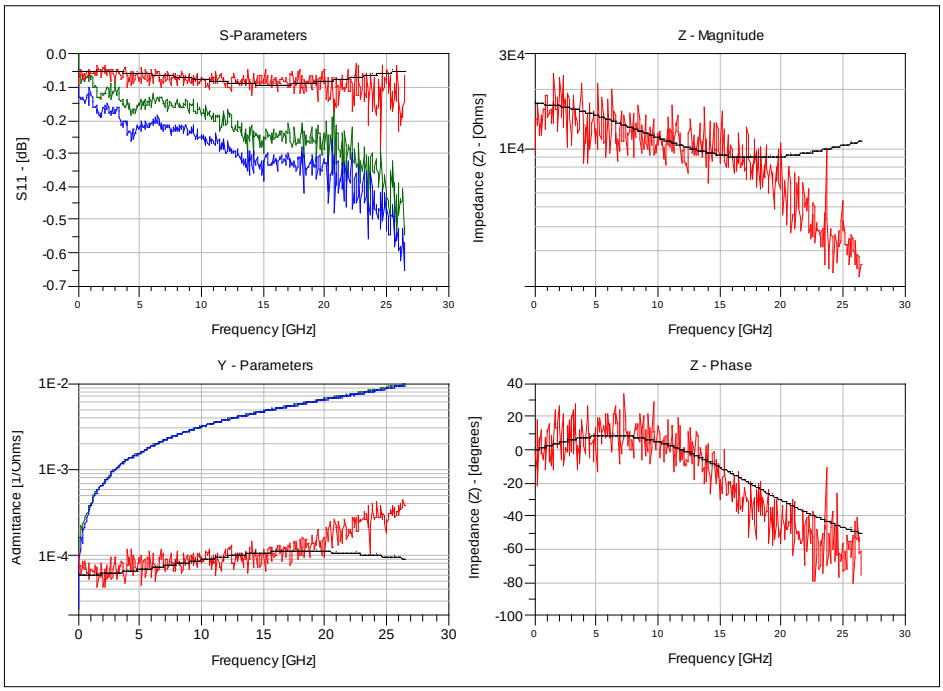

- With CNTs - No CNTs - De-embeded data -o- Simulated

Device A5C2 - 15KOhms - Ohmic

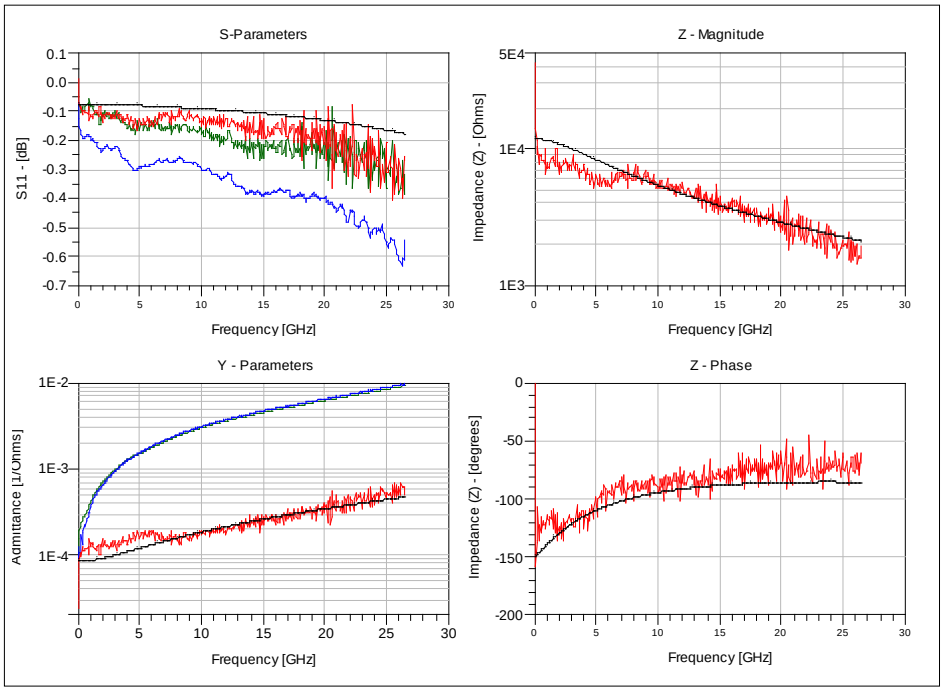

- With CNTs - No CNTs - De-embeded data -o- Simulated

Device B5B1 - 27KOhms - Ohmic

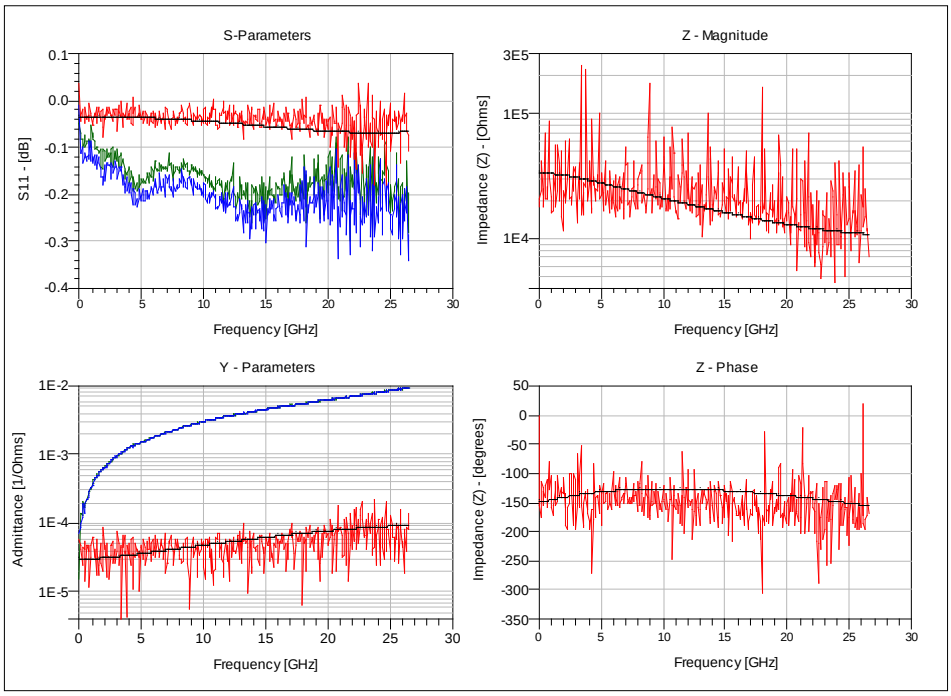

- With CNTs - No CNTs - De-embeded data -o- Simulated

BIBLIOGRAPHY

[1] S. M . Kim, et. al., "Biomedical terahertz imaging with a quantum cascade laser," *Appl. Phys. Lett.* **88**, 153903 (2006)

[2] John F Federici, *et al*, "THz imaging and sensing for security applications—explosives, weapons and drugs," *Semicond. Sci. Technol.* **20** (2005).

[3] H. Yoshida, et al, "Terahertz sensing method for protein detection using a thin metallic mesh," *Appl. Phys. Lett*. **91**, 253901 (2007)

[4] M. Beard, et. al, "Terahertz Spectroscopy," *J. Phys. Chem. B*, **106** (29), pp 7146–7159 (2002).

[5] J. Kawamura, et al, "A 1.5 THz hot electron bolometer receiver for ground-based terahertz astronomy in northern Chile," *Proc. SPIE,* vol. **6373**, (2006)

[6] M. Tonouchi, "Cutting-edge terahertz technology," *Nature Photonics* **1**, 97 - 105 (2007).

[7] A. Maestrini, et al, "Terahertz Sources Based on Frequency Multiplication and Their Applications," *Journ. of RF-Engin. and Tele.* vol. **62**, pp. 118-122 (2008).

[8] Mikhail A. Belkin, Jonathan A. Fan, Sahand Hormoz, Federico Capasso, Suraj P. Khanna, Mohamed Lachab, A. G. Davies, and Edmund H. Linfield, "Terahertz quantum cascade lasers with copper metal-metal waveguides operating up to 178 K," Opt. Express **16**, 3242-3248 (2008)

[9] Ekstrom, et. al, "Conversion Gain and Noise of Niobiuum Supercinducting Hot-Elctron Mixers," *IEEE Trans. on Microwave The. and Tech.,* vol. **4**, (1995)

[10] B. S. Karasik, "Noise temperature limit of a superconducting hot-electron bolometer mixer," *App. Phys. Lett.*, vol. **68**, (1996)

[11] J. Hone, B. Batlogg, Z. Benes, A. T. Johnson, J. E. Fischer, "Quantized Phonon Spectrum of Single-Wall Carbon Nanotubes," *Science,* **289**, 1730 (2000).

[12] F. Leonard, *The Physics of Carbon Nanotube Devices, v*ol. 1 (William Andrew, New York, 2008).

[13] J-S. Lauret et al., " Ultrafast Carrier Dynamics in Single Wall Carbon Nanotubes," *Phys. Rev. Lett.*, vol **90**, 057404 (2003).

[14] M. S. Fuhrer, M. Forero, A. Zettl, and P. L. McEuen, "Ballistic Transport in semcionducting carbon naotubes," *AIP Conf. Proc.*, Nov. 7 2001, vol. **591**, pp 401-404 (2001)

[15] S P Hepplestone and G P Srivastava 2007 *J. Phys.: Conf. Ser.* **92** 012076

[16] E. Gerecht, C. Musante, Y. Zhuang, K. Yngvesson, T. Goyette, J. Dickinson, J. Waldman, P. Yagoubov, G. Gol'tsman, B. Voronov, and E. Gershenzon, *IEEE Trans. Microwave Theory Techn.*, vol. **47**, pp. 2519–2527, (1999).

[17] K.S. Yngvesson, F. Rodriguez-Morales, R. Zannoni, J. Nicholson, M. Fischetti, and J. Appenzeller, "Microwave Detection and Mixing in Metallic Single Wall Carbon Nanotubes and Potential for a New Terahertz Detector," *17th Intern. Symp. Space Terahertz Technol.*, Paris, France, May 2006, p. 135.

[18] S. Iijima, "Helical Microtubes of Graphitic Carbon," *Nature*, vol. 354, pp. 56-58, Nov. 1991.

[19] P. Avouris, Z. Chen, and V. Perebeinos, "Carbon Based Electronics," *Nat. Nanotech.*, vol. **2**, pp. 605-615 (2007).

[20] M. C. Hersam. "Progress towards monodisperse single-walled carbon nanotubes," *Nat. Nanotech.*, vol. **3**, pp. 387-394 (2008).

[21] S. J. Tans, M. H. Devoret, H. Dai, A. Thess, R. E. Smalley, L. J. Georliga, and C. Dekker, "Individual Single-wall Carbon Nanotubes as Quantum Wires," *Nature*, vol. 386, pp. 474-477, 1997.

[22] M. Bockrath, D. H. Cobden, P. L. McEuen, N. G. Chopra, A. Zettl, A. Thess, and R. E. Smalley, "Single-electron Transport in Ropes of Carbon Nanotubes," *Science*, vol. 275, pp. 1922-1925, 1997.

[23] J. Kong, E. Yenilmez, T. W. Tombler, W. Kim, and H. Dai, "Quantum Interference and Ballistic Transmission in Nanotube Electron Waveguides," Physical Review Letters, vol. 87, No. 10, 106801, September 2001.

[24] Ji-yong Park, S. Rosenblatt, Y. Yaish, V. Sazonova, H. Üstünel, S. Braig, T. A. Arias, P. W. Brouwer, and P. J. McEuen, "Electron-Phonon Scattering in Metallic Single-Walled Carbon Nanotubes," Nano Letters, vol. 4, No. 3, pp. 517-520, 2004.

[25] R. Lu, G. Xi, and J.Z. Wu, "Effects of Thermal Annealing on Noise Property and Temperature Coefficient of Resistance of Single-Walled Carbon Nanotube Films," *App. Phys. Lett.* vol. **93**, 213101 (2008)

[26] F. Kreupl, A. P. Graham, M. Liebau, G.S. Duesberg, R. Seidel, E. Unger, " Carbon Nanotubes for Interconnect Applications," *IEDM Tech. Dig*., pp. 683 - 686, 2004

[27] M. P .A Fisher and L. I. Glazman, "Transport in a one-dimensional Lüttinger liquid," *Mesoscopic Electron Transport.* Dordrecht, The Neatherlands: Kluwer, 1997

[28] P. J. Burke, "Lüttinger liquid theory as a model of the gigahertz electrical properties of carbon nanotubes," *IEEE Trans. Nanotech*. **1**,129 (2002).

[29] J. J. Plombon et. al, "High-frequency electrical properties of individual and bundled carbon nanotubes," *App. Phys. Lett.*, vol. **90**, 063106 (2007).

[30] M. Bockrath et. al., "Lüttinger-liquid behavior in carbon nanotubes," *Nature*, vol. **397**, pp. 598 (1999)

[31] S. Tomonaga, "Remarks on Bloch's method of sound waves applied to many-Fermion problems," *Prog. Theor. Phys.*, vol. 5, no. 4, pp. 544–569, 1950.

[32] J. M. Lüttinger, "An exactly solvable model of a many-Fermion system," *J. Math. Phys.*, vol. 4, no. 9, p. 1154, 1963.

[33] S. Ilani, L. A. K. Donev, M. Kindermann, and P. L. McEuen, "Measurement of the quantum capacitance of interacting electrons in carbon nanotubes," *Nature Physics*, vol. 2, pp. 687-691, Oct. 2006.

[34] K. S. Yngvesson, *"Microwave Semiconductor Devices"*, Kluwer Academic, Norwell, MA (1991).

[35] D.F. Santavicca, "Bolometric Response of Superconducting Microbridges and Single-Walled carbon Nanotubes," PhD Dissertation, September, 1992.

[36] J.L. Hesler, T.W. Crowe, D.F. “NEP and responsivity of THz zero-bias Schottky diode detectors,” paper 1646, 32nd Intern. Conf. Infrared, Millimeter and Terahertz Waves, Sept. 2007, Cardiff, Wales.

[37] K. Fu, “Metallic Carbon Nanotubes, Microwave Characterization and Development of a Terahertz Detector,” *M.Sc. thesis, University of Massachusetts, Amherst, MA* (2008).

[38] Th. Hunger, B Lengeler, and J. Appenzeller, “Transport in ropes of carbon nanotubes: Contact barriers and Luttinger liquid theory,” *Phys. Rev. B.* vol, **69**, 195406 (2004).

[39] J. Yang, “AlGaAs/GaAs Two Dimensional Electron Gas Devices: Applications in Millimeter and Submillimeter Waves,” PhD Dissertation, *University of Massachusetts, Amherst, MA. Sept.* (2002.

[40] P.L. Richards, *J. Appl. Phys*., **76**, 1 (1994).

[41] D.F. Santavicca and D. Prober, “Terahertz Resonances and Bolometric Response of a Single Walled Carbon Nanotube”, paper 1646, 33rd Intern. Conf. Infrared, Millimeter and Terahertz Waves, Sept. 2008, CalTech, Pasadena, CA.

[42] M. Ji, “Lens Coupled Printed Antenna Characterization,” MS Thesis Dissertation, *University of Massachusetts, Amherst, MA.* May, 2001.

[43] K. Fu, R. Zannoni, C. Chan, S.H.Adams, J. Nicholson, E. Polizzi and K.S. Yngvesson, “Terahertz detection in single wall carbon nanotubes,” *Appl. Phys. Lett.*, **92**, 033105 (2008).

[44] K.S. Yngvesson, K. Fu, B. Fu, R. Zannoni, J. Nicholson, S.H. Adams, A. Ouarraoui, J. Donovan and E. Polizzi, “Experimental detection of terahertz radiation in bundles of single walled carbon nanotubes,” Proc. 19th Intern. Symp. Space Terahertz Technol., Groningen, The Netherlands, April 28-30, 2008, p. 304.

[45] E. Carrion, M. Muthee, J. Donovan, R. Zannoni, J. Nicholsosn, E. Polizzi, and K.S. Yngvesson. “New Results on Terahertz Detection by Carbon Nanotubes,” Proc. 20th Intern. Symp. Space Terahertz Technol., Charlottesville, VA, April 20-22, 2009, p. 110.

[46] P. J. Burke "Nano-dielectrophoresis: Electronic Nanotweezers" *Encyclopedia of Nanoscience and Nanotechnology*, Editor H.S. Nalwa, v. 6, p. 623-641(2004).

[47] J. D. Beck, L. Shang, M. S. Marcus, and R. J. Hamers, "Manipulation and Real-Time Electrical Detection of Individual Bacterial Cells at Electrode Junctions: A Model for Assembly of Nanoscale Biosystems," *Nano Lett.*, vol. **5**, pp. 777-781 (2005).

[48] R. Krupke, et. al., "Simultaneous Deposition of MetallicBundles of Single-walled Carbon Nanotubes Using Ac-dielectrophoresis," *Nano. Lett.* vol. **3**, pp. 1019-1023 (2003).

[49] M. Dimaki and P. Boggild, "Dielectrophoresis of carbon nanotubes using microelectrodes: a numerical study," *Nanotech.* vol. **15**, (2004).

[50] J. Tang, et. al., " Rapid and Reproducible Fabrication of Carbon Nanotube AFM Probes by Dielectrophoresis," *Nano Lett.*, vol. **5**, pp. 11-14 (2005).

[51] D. Xi, A. Subramanian, L. Dong, and B. Nelson, “Shaping Nanoelectrodes for High-Precision Dielectrophoretic Assembly of Carbon Nanotubes,” *IEEE Trans. Nanotech.* vol. **8**, 449 (2009).

[52] R. Krupke and F. Hennrich, *Adv. Eng. Mater.* **7**, 111 _2005.

[53] A. P. Salet, and A.M. Ionescu, “A Study of Deterministic Positioning of Carbon Nanotubes by Dielectrophoresis,” *Journal of Electronic Materials,* vol. **38**, 742 (2009).

[54] S. Sorgenfrei, K. L .Shepard et. al, "Controlled dielectrophoretic assembly of carbon nanotubes using real-time electrical detection," *App. Phys. Lett.,* vol. **94**, 053105 (2009).

[55] A. Vijayaraghavan, R. Krupke, et. al., " Ultra-Large-Scale Directed Assembly of Single-Walled Carbon Nanotube Devices," *Nano Lett.,* vol. **7**, pp 1556-1560 (2007)

[56] Cheap Tubes, Brattleboro, Vt.. Purified 90% SWCNTs, grown by CVD, nominal diameter from 1 to 2 nm., average length of 50 μm before ultrasonication.

[57] Brewer Science, Rolla, MO. Product used CNTRENE®.

[58] Picoprobe®, by GGB Industries Inc.

[59] C. Highstrete, E. Shaner, and M. Lee, "Microwave dissipation in arrays of single-wall carbon nanotubes," *App. Phys. Lett.,* vol. **89**, 173105 (2006).

[60] E. Pop, D.A. Mann, K. Goodson, and H. Dai, J. Appl. Phys., **101**, 093710 (2007).

[61] B.S. Karasik and A.I. Elantiev, Proc. 6th Intern. Symp. Space Terahertz Technol., Pasadena, CA, March 1995, pp. 229-246.

[62] E. Carrion, M. Muthee, Z. Chen, J. Nicholsosn, E. Polizzi, and K.S. Yngvesson. “Single Wall Carbon Nanotube (SWCNT) Devices as THz detectors and Mizers,” Proc. 21th Intern. Symp. Space Terahertz Technol., Oxford, March 23-25, (2010)